Finite element, adaptive spectral wave modelling

Alexandros Adam

Submitted for the degree of Doctor of Philosophy
and the Diploma of Imperial College

Applied Modelling & Computation Group
Department of Earth Science and Engineering
Imperial College London

September 2016

Abstract

The ability to predict the wave climate has a great impact on a wide range of sectors, including coastal and offshore engineering, marine renewable energy and shipping. The state of the art in wave prediction is called spectral wave modelling and is based on a phase-averaged, spectral description of the sea-surface elevation. The governing equation, called the action balance equation, is five-dimensional and describes the generation, propagation and evolution of action density in geographic space, spectral space and time. Due to the multidimensional nature of the equation the feasible resolutions are restricted by the computational costs. The aim of this work is to propose schemes which can increase the range of possible resolutions in spectral wave modelling, with the use of adaptivity in space and angle. Thus, this work focuses on the development of an unstructured, adaptive finite element spectral wave model (Fluidity-SW).

A sub-grid scale model for the spatial discretisation is used, which retains the stability of discontinuous systems, with continuous degrees of freedom. Then, a new framework for angular adaptivity is developed, with results in dynamic angular and spatial anisotropy of the angular mesh. Finally a spatially $h-$adaptive scheme is implemented, which can dynamically treat the spatial gradients of the solution fields. The resulting framework is thoroughly verified and validated in a wide range of test cases and realistic scenarios, against analytical solutions, wave measurements and the results obtained with the widely used SWAN model. Thus, the overall ability of the code to simulate surface gravity wind-waves in fixed and adaptive spatial and angular meshes is demonstrated.

Copyright Declaration

The copyright of this thesis rests with the author and is made available under a Creative Commons Attribution Non-Commercial No Derivatives licence. Researchers are free to copy, distribute or transmit the thesis on the condition that they attribute it, that they do not use it for commercial purposes and that they do not alter, transform or build upon it. For any reuse or redistribution, researchers must make clear to others the licence terms of this work.

Declaration

I hereby certify that the work presented in this dissertation is the result of my own investigations during the PhD project. Text and results obtained from other sources are referenced and properly acknowledged.

Alexandros Adam
September 2016

Acknowledgements

Firstly, I would like to express my gratitude to my supervisors Prof. Matthew Piggott, Dr Andrew Buchan and Prof. Chris Pain, for offering me the necessary support, guidance and motivation throughout this project.

My sincere thanks also goes to Dr Mark Goffin for helping me in the initial stages of code development and Dr Steven Dargaville for his continued help and valuable input. I also want to thank Richard Smedley-Stevenson for the countless conversations about the project.

What is more, during these years, I benefited greatly from the interaction, advice and help of a large number of people. I would like to thank the entire Applied Modelling and Computational Group for providing a multidisciplinary environment which allowed me to learn and progress during my PhD. To name a few, Dr Jon Hill, Stephan Kramer, Dr Pablo Salinas, Dr Tim Graves, as well as my fellow PhD students Amin Abolghasemi and Dr Frank Milthaler.

I also want to acknowledge the department of Earth Science and Engineering, for providing me with the funding for this work, and Prof. Peter Allison for offering the necessary support which allowed me to finish the project.

Last but not least, I want to thank my parents Sotiris and Aggeliki whose encouragement and support throughout the years made it possible for me to embark on a PhD. Most importantly, however, I would like to thank my partner Evita for her understanding, her unconditional support and limitless patience. I would not have been able to finish this work without her help.

Table of Contents

1 Introduction **23**

1.1 Motivation 23

1.2 Main contributions 25

1.3 Structure 25

2 Theoretical background **27**

2.1 Introduction 27

2.2 Energy density spectrum 29

2.3 Action balance equation 32

2.3.1 Propagation in geographical space 33

2.3.2 Propagation in frequency 34

2.3.3 Propagation in angle 35

2.4 Source terms 36

2.4.1 Wind input 36

2.4.2 White-capping 38

2.4.3 Four-wave interactions (quadruplets) 39

2.4.4 Three-wave interactions (triads) 41

2.4.5 Depth-induced breaking 42

3 Discretisation **45**

3.1 Introduction 45

3.2 Source term linearisation 46

3.3 Temporal discretisation 49

3.4 Frequency discretisation 50

3.5 Angular discretisation 51

3.6 Spatial discretisation 55

4 Validation **63**

4.1 Introduction 63

4.2 Numerical diffusion 64

4.3 Depth-induced shoaling and refraction 65

4.4 Current-induced shoaling and refraction 71

4.5 Fetch-limited growth 76

4.6 Shallow water non-linear interactions 79

4.7 Depth-induced wave breaking 81

4.8 Conclusions 84

5 Angular adaptivity **85**

5.1 Introduction 85

5.2 Wavelets 87

5.2.1 Multiresolution analysis 87

5.2.2 Wavelet construction 88

5.2.3 Haar wavelets 89

5.2.4 Calculating the angular matrices 91

5.3 Angular adaptivity 93

5.3.1 Error measure 94

5.3.2 Adaptive procedure 95
5.4 Numerical results 96
5.4.1 Depth-induced shoaling-refraction 97
5.4.2 Deep water propagation 100
5.5 Conclusions 105

6 Verification **109**
6.1 Introduction 109
6.2 Haringvliet estuary 110
6.2.1 Model set-up 110
6.2.2 Results 113
6.3 Haringvliet estuary – Angular adaptivity 117
6.3.1 Motivation and model set-up 117
6.3.2 Results 118
6.4 Haringvliet estuary – Spatial adaptivity 125
6.4.1 Motivation and model set-up 125
6.4.2 Results 126
6.5 Conclusions 130

7 Conclusions and future work **133**

Bibliography **139**

Appendix A Sub-grid scale matrices **149**

List of Figures

3.1 Example of a cell-centred control volume σ_q of the frequency dimension σ, with the flux $F^{\sigma_{q\pm1/2}}$ from the boundaries. 50

3.2 Example of an element j of the angular dimension θ, the angular flux $F_{j\pm1/2}$ and the normals $\hat{\mathbf{n}}_\theta$ at the element boundaries. 53

4.1 Contour plots of significant wave heights for the numerical diffusion test case. Line 1 and line 2 refer to transects across which the significant wave heights are displayed in figure 4.2. 66

4.2 Line plots of significant wave heights for the numerical diffusion test case, for the two lines shown in figure 4.1a. 67

4.3 Depth induced shoaling and refraction. The depth is linearly decreasing from 20 m in the eastern boundary to 0.05 m in the western boundary. This is resolved with a non-uniform mesh with smaller edge lengths in the shallow water region. Two test cases are considered. In test case I the incoming wave enters at an angle of 180°, while in test case II at an angle of 210°. 68

4.4 Spatial and angular convergence for test case I and test case II of the depth-shoaling and refraction test case respectively. 69

4.5 Validation for depth induced shoaling and refraction for a wave entering at an angle of 180° (test case I), along the line shown in figure 4.3b. 70

4.6 Validation for depth induced shoaling and refraction for a wave entering at an angle of 210° (test case II), along the line shown in figure 4.3b. 71

4.7 Current induced shoaling. Two test cases are considered. In test case I waves are opposing and in test case II following the current direction. The V_x current-component is decreasing linearly in the $x-$direction from 2 m/s to 0 m/s. 72

4.8 Validation for current induced shoaling, along the line shown in figure 4.7b. In test case I waves are opposing and in test case II following the current direction. 73

4.9 Current induced shoaling and refraction on a shearing current. Two test cases are considered: The incoming wave is at an angle of 210° for test case III and 150° for test case IV. The V_y current-component is decreasing linearly in the $x-$direction from 2 m/s to 0 m/s. 74

4.10 Validation for current induced shoaling and refraction, for an incoming wave at an angle of 210°, for test case III, and 150°, for test case IV, on top of a shearing current. The results are plotted along the line shown in figure 4.7b. 75

4.11 Spatial mesh for the fetch limited growth test case. The wind is blowing in the positive $x-$ direction ($\theta_{\text{wind}} = 0°$). 77

4.12 Validation for non-dimensional energy E^* against non-dimensional fetch x^*, for the fetch limited growth test case. 78

4.13 Validation for non-dimensional peak frequency ${f_p}^*$ against non-dimensional fetch x^*, for the fetch-limited growth test case. 78

4.14 Set-up of the flume experiment by Beji and Battjes [10] for shallow water three-wave interactions, with the location of the gauges used for the output of the spectrum in figure 4.16. 79

4.15 Validation for the three-wave interactions test case. The significant wave height is plotted along the $y = 9.5$ m line of the domain. 80

4.16 Validation for the three-wave interactions test case. Variance density plots for the gauge locations of figure 4.14. 82

4.17 Set-up of the flume experiment by Battjes and Janssen [8] for depth-induced wave breaking. 83

4.18 Validation for the depth induced breaking test case. The significant wave height is plotted along the $y = 9$ m line of the domain. 83

5.1 Haar wavelet MRA of the 2π angular domain. Each space V_l has 2^l subdivisions. 90

5.2 Example of Haar wavelets on a quadrant of the 2π angular domain. Each V_j space (denoted on the left) is reproduced by $V_j = V_l \oplus_{n=2}^{j-1} W_n$ (denoted on the right). Space V_5 can be thus reproduced by $V_5 = V_2 \oplus W_2 \oplus W_3 \oplus W_4$. 91

5.3 Polar plots for various Haar wavelet expansions. Each concentric circle represents the spaces: $\{V_l, W_l, W_{l+1}, ..., W_{j-1}\}$, for a $HW_{l,j}$ discretisation. 92

5.4 Simplified example of the angular adaptive scheme. Starting from the left sketch the red basis function suggests that the respective next level (dashed line) basis functions(green) should be added, i.e. the wavelet coefficient is bigger than the tolerance $N_i > \tau$. The central sketch shows that one of the two newly added basis functions can be removed (yellow), while the other requires yet another level. The sketch on the right shows the final adapted system. 95

5.5 Depth induced refraction. Convergence tests for uniform $P0$ and $HW_{3,j}$, $j_{\max} \in \{4, 5, 6, 7, 8, 9, 10\}$, adaptive discretisations for various tolerances: $\tau = 1$ $\tau = 10^{-1}$, $\tau = 10^{-2}$. The $HW_{3,j}$ points correspond to the results after the adaptive algorithm converges. . . . 98

5.6 Depth induced refraction. Convergence tests for uniform $P0$ with $\{16, 32, 64, 128, 256, 400\}$ angles and $HW_{3,j}$, $j_{\max} \in \{4, 5, 6, 7, 8, 9, 10\}$, adaptive discretisations for a tolerance $\tau = 10^{-1}$. The $HW_{3,j}$ points correspond to the results after the adaptive algorithm converges. 99

5.7 Polar plots for a $HW_{3,10}$ discretisation for points: $a = (0\text{ m}, 1000\text{ m})$, $b = (2000\text{ m}, 1000\text{ m})$, $c = (4000\text{ m}, 1000\text{ m})$. 100

5.8 Spatial mesh and initial conditions for the deep water propagation test case. 101

5.9 Significant wave height after 5 days of deep water propagation, for a $P0$ angular discretisation with various angular resolutions. 101

5.10 Significant wave height for an adaptive $HW_{2,6}$ discretisation with tolerance $\tau = 10^{-6}$ at several time levels. 102

5.11 Absolute difference in significant wave height between a $P0-64$ angle and an adaptive $HW_{2,6}$ discretisation with tolerance $\tau = 10^{-6}$ for various time levels. Colorbar in logarithmic scale. 103

5.12 Angular mesh, i.e. number of angular basis functions, for a $HW_{2,6}$ discretisation with tolerance $\tau = 10^{-6}$ at various time levels. The polar plots for the points denoted by the yellow dots are presented in figure 5.13. 103

5.13 Polar plots of a $HW_{2,6}$ discretisation for the points in figure 5.12, at their respective time levels. 104

5.14 Error against run-time for the deep water propagation test case. Results for $P0$ with $\{8, 16, 32, 64, 128, 256\}$ angles and $HW_{2,j}$, $j_{max} \in \{3, 4, 5, 6, 7, 8\}$, for tolerances: $\tau = 10^{-6}$, $\tau = 10^{-7}$, $\tau = 10^{-8}$. Each point corresponds to the error compared to a uniform $P0$ discretisation with 300 angles, at the final time level. 105

5.15 Mean number of angular basis functions against timelevel for the deep water propagation test case. $HW_{2,3}$, $HW_{2,4}$, $HW_{2,5}$, $HW_{2,6}$, $HW_{2,7}$, $HW_{2,8}$, for a tolerance of $\tau = 10^{-6}$. 106

6.1 Bathymetry and spatial mesh for the Haringvliet estuary, along with the locations of the eight observation stations and the location of the Hinderplaat shoal (taken from the SWAN website [82]). The positive $y-$ axis is rotated by 38.8° relative to the North. 111

6.2 Variance density plots at the locations of figure 6.1a for the Haringvliet estuary at 14 October 1982, 21:00 UTC (test case I). 114

6.3 Variance density plots at the locations of figure 6.1a for the Haringvliet estuary at 14 October 1982, 23:00 UTC (test case II). 116

6.4 Mean number of angular basis functions, for an adaptive $HW_{2,5}$ discretisation with tolerance $\tau = 10^{-2}$ at each iteration step, for the Haringvliet test case. 119

6.5 Angular mesh, i.e. number of angular basis functions, for an adaptive $HW_{2,5}$ discretisation with tolerance $\tau = 10^{-2}$ at various iteration steps, for the Haringvliet test case. 119

6.6 Mean number of angular basis functions, for an adaptive $HW_{2,5}$ discretisation with tolerance $\tau = 10^{-3}$ at each iteration step, for the Haringvliet test case. 120

6.7 Angular mesh, i.e. number of angular basis functions, for an adaptive $HW_{2,5}$ discretisation with tolerance $\tau = 10^{-3}$ at various iteration steps, for the Haringvliet test case. 121

6.8 Variance density plots at the locations of figure 6.1a for the Haringvliet estuary (test case II). An adaptive $HW_{2,5}$ discretisation with tolerances $\tau = 10^{-2}$ and 10^{-3} compared against the uniform $P0$ results with 32 angles. 123

6.9 Polar plots for an adaptive $HW_{2,5}$ discretisation with tolerance $\tau = 10^{-2}$, for the Haringvliet test case. The locations are depicted in figure 6.1a. 124

6.10 Variance density plots at location 5 of figure 6.1a, for the Haringvliet estuary (test case II). The results from a finely resolved grid with SWAN, compared to the coarse results of section 6.2. 127

6.11 Spatial adaptivity for the Haringvliet test case with Fluidity-SW. Number of spatial elements at each non-linear iteration. 128

6.12 Spatial adaptivity for the Haringvliet test case with Fluidity-SW. Spatial mesh at various iteration steps. 128

6.13 Variance density plots at location 5 of figure 6.1a, for the Haringvliet estuary (test case II). The results from a finely resolved grid with SWAN, compared to the results from spatial adaptivity with Fluidity-SW. 129

7.1 Example of an idealised test case, where a monochromatic wave propagates over a long distance. Two different simulations are presented, with the application of spatial and angular adaptivity respectively. . . 136

List of Tables

6.1 Description of the conditions for the two test cases considered for the Haringvliet estuary. The wind direction assumes a nautical convention, i.e. the direction from which the wind is blowing is measured clock-wise from North. 111

Chapter

ONE

Introduction

1.1 Motivation

Interest in the prediction of ocean waves grew during the Second Word War, driven by the need to plan landing operations [48]. A lot of effort has been made since and the state of the art is now called spectral wave modelling, or phase-averaged wave modelling. This is based on a statistical, spectral description of the sea-surface elevation. It is governed by the action balance equation, a five-dimensional system in geographic space, spectral space (frequency and angle) and time, which models the processes of wave generation, wave propagation and wave dissipation in oceanic and coastal environments.

The ability to predict the wave climate has an impact on a very wide range of sectors. It is important to civil and marine engineering for the designing of ports, harbours, offshore structures, and marine energy converters. It is necessary for the study of the complex physical processes controlling sedimentation, which in turn affect the morphology and local biology of coastal areas. It is vital to the shipping industry for the scheduling of safe navigation routes. Thus, spectral wave models are now used for a multitude of applications, including wave forecasting, climatology and wave energy resource assessments.

Well known models include the Wave Prediction Model (WAM) [91] and WAVEWATCH III (WWIII) [84], which were originally developed for global wave predictions, and the Simulating Waves Nearshore model (SWAN) [13], originally designed to be used for coastal simulations. These were all based on finite difference methods on structured grids. As the application field for spectral wave models spread, however, and the need for increased resolution in the coastal regions grew, codes able of working with more flexible, multi-scale unstructured meshes starting being developed.

The first attempt was made by Benoit et al. [11] who developed TOMAWAC, a semi-Langrangian model on triangular grids. Then Sørensen et al. [79] developed MIKE21SW, which was based on a cell-centered finite volume discretisation of the geographic and spectral space. Hsu et al. [43] then developed the Wind Wave Model (WWMI) by using a Taylor-Galerkin scheme for the spatial discretisation of the system. This was then extended by Roland [76] (WWMII) by introducing Fluctuation Splitting schemes to the spatial discretisation of the WWMI. Qi et al. [70] then developed a finite-volume code (FVCOM-SWAVE), and soon after Zijlema [99] modified SWAN to allow its use on unstructured grids in a finite difference framework.

More recent developments in the numerical treatment of spectral wave models include the high-order hybrid spectral/DG model developed by Yildirim and Karniadakis [96], who used a discontinuous Galerkin formulation for the discretisation of geographic space and a Fourier-collocation method for the discretisation of spectral space. Meixner et al. [59] then developed a discontinuous finite element model, introducing $p-$adaptivity in both geographic and spectral space.

The motivation behind the work presented in this thesis was to further explore the frameworks for the numerical treatment of spectral wave models, by developing adaptive schemes for space and angle. Due to the multidimensional nature of the governing equation, the feasible resolutions are restricted by the computational costs. Adaptivity is, thus, studied here as a means of reducing the computational cost for high-fidelity simulations. To this end, a new model is developed, named hereafter Fluidity-SW, based on a finite element expansion in geographic and angular space, employing a compactly-supported angularly adaptive algorithm and a spatially $h-$adaptive algorithm.

1.2 Main contributions

The main contributions of this work can be summarised as:

- A new approach for the discretisation of the action balance equation is proposed, with a focus on the treatment of the spatial and angular dimensions. A discontinuous finite element expansion is used for the angular dimension and a sub-grid scale finite element method for the spatial. The sub-grid scale combines the benefits of discontinous formulations, i.e. stability and accuracy, with continuous formulations, i.e. low cost.

- A new framework is developed for applying anisotropic angular adaptivity in spectral wave modelling. Haar wavelets are used for the first time to discretise the angular dimension of the action balance equation. These hierarchical, compactly supported basis functions are used to develop an adaptive framework allowing for spatially variable, anisotropic angular adaptivity. The framework is then validated and it is demonstrated that using variable angular meshes allows for a reduction of the computational effort compared to uniform angular resolutions.

- An unstructured dynamically $h-$adaptive scheme is implemented for the spatial dimension of the spectral wave model. This is validated in a realistic scenario and it is shown to more accurately resolve the gradients in the solution fields at a reduced cost, compared to fixed spatial meshes.

- The code is validated and verified against a plethora of standardised test cases, as well as realistic scenarios, typically used for the verification and validation of spectral wave models. The results are compared to analytical solutions, wave measurements and the results obtained with the unstructured mesh version of the widely used SWAN model. Thus, the overall ability of the code to simulate surface gravity wind-waves on fixed and adaptive spatial and angular meshes is thoroughly demonstrated.

1.3 Structure

First in chapter 2 a brief theoretical background of spectral wave modelling is presented, introducing the basic aspects of the spectral description of waves and the

action balance equation. Then in chapter 3 the proposed discretisation for the system is explained, deriving the final discrete form of the action balance equation, as it is implemented in Fluidity-SW. In chapter 4 the code is then validated against a set of standardised cases, which test each term of the system separately, by isolating the main physical processes. Then in chapter 5 a new framework for the application of angular adaptivity is developed. The scheme is tested against uniform angular resolutions in idealised test cases and the relative benefits are quantified. Finally in chapter 6 the code is tested on a realistic test case, with all the terms of the equation activated. This is then followed by the application of angular and spatial adaptivity, on the same scenario and the comparison of fixed and adaptive angular and spatial meshes in terms of accuracy and degrees of freedom.

Chapter

TWO

Theoretical background

2.1 Introduction

A wide range of different numerical models are now available which can be used for the study of wave generation and propagation. These can be split into two main categories: phase-resolving and phase-averaging [7]. Phase-resolving models, such as potential flow, mild-slope, Boussinesq and full 3D Navier-Stokes models represent the sea surface elevation in space and time and accurately account for non-linear processes. They are, however, computationally expensive and, thus, restricted to relatively small scale applications. Phase-averaging models are based on a spectral description of the waves and though the non-linearities are mostly represented by parametrised formulations, they are cheap enough to be used on larger problem domains, such as global wave forecasting applications.

Spectral wave modelling first appeared after the introduction of the wave energy spectrum by Pierson [66] and the introduction of the energy balance equation by Gelci [33]. In this framework, the sea surface elevation is composed of a superposition of harmonic wave components and the energy spectrum $E(x, y, f, \theta, t)$ represents the energy content in geographic space (x, y), spectral space, i.e. frequencies f and directions θ, and time t.

The energy spectrum is calculated based on the conservation of energy in an Eulerian framework. A kinematic part, representing the propagation of wave energy in geographic and spectral space, is balanced with a set of source terms to represent the rate of change of the spectrum. After the introduction of the equation, Gelci used a purely empirical expression to represent the evolution of the spectrum. It was not until the work of Phillips [64] and Miles [60] on wave generation, and Hasselmann [37] on non-linear wave-wave interactions that a general expression for the source function was formed.

Based on the various forms of the spectral equation, a number of spectral wave models have been developed from as early as the 1960s. So-called "first-generation models" did not account (or loosely accounted) for non-linear wave-wave interactions. "Second-generation" models used a simplified parametrised form for these interactions, restricting the shape of the spectrum. A thorough review of these early models can be found in [80].

The next milestone in spectral wave modelling came from the WAMDI group [91] with the introduction of WAM, a model with the general form for the source terms still used today (i.e. wind generation, wave-wave transfers and wave dissipation) and no a-priori restriction on the shape of the spectrum. This framework was coined as "third-generation" wave modelling and followed by rapid developments. Currents were included in the formulation by rewriting the governing equation in terms of the action density, which is conserved in a relative frame of reference moving with the current [14]. The action balance equation was then extended to account for shallow water propagation, such as shoaling and refraction and shallow water non-linear processes, such as triads and depth induced breaking.

In the next sections, first a brief summary of [41] is presented to describe the basic aspects of the spectrum and the action balance equation, the governing equation in spectral wave modelling. This is then followed by the description of each of the implemented source functions.

This is by no means a thorough review of either the theory of waves or the progress in spectral wave modelling. For a more in depth overview of the theory of surface gravity waves the reader can refer to [93, 57], while more specialised textbooks on spectral wave modelling include [48] and [41]. Finally a thorough review of the more recent notable developments in spectral wave modelling can be found in [46] and [19].

2.2 Energy density spectrum

In the framework of spectral wave modelling, the energy density spectrum is one of the most important concepts, as it provides the basis for the statistical description of the sea surface elevation. Within the context of the linear wave theory for surface gravity waves, the surface elevation $\eta(t)$ (m), as a function of time at one location, can be described by the sum of a number of harmonic wave components,

$$\eta(t) = \sum_{i=1}^{N} a_i \cos(2\pi f_i t + \alpha_i), \tag{2.1}$$

with a_i (m) and α_i (rad) being the amplitude and phase respectively, and f_i (Hz) the frequency of each wave component. Thus, a Fourier analysis of a surface elevation record would yield the values of amplitude and phase for each frequency. These are called the amplitude and phase spectrum.

Due to the chaotic behaviour of wave generation and propagation, by measuring the surface elevation many times under statistically identical conditions the time record would be different and thus the amplitude and phase spectrum would be different. To surpass this problem, the sea surface elevation is assumed to be a stationary Gaussian process with a_i and α_i treated as random variables. In other words, each wave in this sum of harmonic components has a constant amplitude and phase, randomly chosen for each realisation of the time record. This is known as the random-phase/amplitude model,

$$\underline{\eta}(t) = \sum_{i=1}^{N} \underline{a}_i \cos(2\pi f_i t + \underline{\alpha}_i), \tag{2.2}$$

where the underscore denotes random variables. Given that the probability distribution for phases is usually uniform between 0 and 2π, the amplitude spectrum is adequate to describe the sea surface elevation. This follows a Rayleigh distribution which is fully described by the expected value,

$$\mu_i = E\{\underline{a}_i\} = \frac{1}{M} \sum_{m=1}^{M} a_{i,m}, \tag{2.3}$$

where M is the number of sample values from the different realisations of the time-

record. Thus for each frequency of the amplitude spectrum there is one uniform distribution for the random phase and one Rayleigh distribution for the random amplitude which can be fully described by $E\{\underline{a}_i\}$.

The amplitude spectrum provides enough information to statistically describe the sea-surface elevation, however, an even more useful variable is the variance of each wave component, which is equal to $E\{\frac{1}{2}\underline{a}_i^2\}$ (m^2). The variance spectrum (as well as the amplitude spectrum) is discrete, given that only values at discrete frequencies f_i are present. To make the spectrum continuous, first the discrete variances are distributed over each frequency interval Δf_i, which results in a variance density of $E\{\frac{1}{2}\underline{a}_i^2\}/\Delta f_i$. Finally, by having the width of the frequency intervals approach zero $\Delta f_i \to 0$ the spectrum becomes continuous,

$$E_{\mathrm{var}}(f) = \lim_{\Delta f \to 0} \frac{1}{\Delta f} E\left\{\frac{1}{2}\underline{a}^2\right\}. \tag{2.4}$$

This is known as the one-dimensional variance density spectrum $E_{\mathrm{var}}(f)$ ($\mathrm{m}^2\mathrm{Hz}^{-1}$), which distributes the variance of the surface elevation, over frequencies.

All the equations derived above are one-dimensional and, thus, the surface elevation does not represent waves coming from all directions. This can be achieved by extending the random phase/amplitude model as

$$\underline{\eta}(x, y, t) = \sum_{i=1}^{N} \sum_{j=1}^{M} \underline{a}_{i,j} \cos(2\pi f_i t - k_i x \cos(\theta_j) - k_i y \sin(\theta_j) + \underline{\alpha}_{i,j}), \tag{2.5}$$

where $k = 2\pi/L$ ($\mathrm{rad\,m}^{-1}$) is the wave number and L (m) is the wave length of the harmonic wave. It is worth noting that this is a three-dimensional model but only two indices i, j are present. This is the case since the wave number and the frequency are directly related through the dispersion relationship of the linear wave theory,

$$\omega^2 = gk \tanh(kd), \tag{2.6}$$

where $\omega = 2\pi f$ ($\mathrm{rad\,Hz}$) is the radian frequency, g ($\mathrm{m\,s}^{-2}$) the acceleration due to gravity and d (m) is the bathymetric value. Thus, the dispersion relationship reduces the dimensions of the random phase/amplitude model to two. By following the same

procedure as above the two-dimensional variance density spectrum becomes

$$E_{\mathrm{var}}(f,\theta) = \lim_{\Delta f \to 0} \lim_{\Delta \theta \to 0} \frac{1}{\Delta f \Delta \theta} E\left\{\frac{1}{2}\underline{a}^2\right\}. \tag{2.7}$$

One of the main reasons the variance density spectrum is preferred to the amplitude density spectrum is that variance is proportional to wave energy. In particular, multiplying the variance density spectrum with the density of water ρ ($\mathrm{kg\,m^{-3}}$) and the acceleration due to gravity yields the energy density spectrum,

$$E(f,\theta) = \rho g E_{\mathrm{var}}(f,\theta). \tag{2.8}$$

The two-dimensional energy density spectrum $E(f,\theta)$ ($\mathrm{Jm^{-2}Hz^{-1}rad^{-1}}$) distributes the amount of wave energy over the frequencies and directions.

All of the important characteristics of the sea surface, such as the significant wave height (the mean of the highest one-third of waves in a record) or the mean period, can then be seen as statistical parameters of the spectrum and derived from various combinations of its moments $m_n = \int\int f^n E(f,\theta) df d\theta$. In particular the significant wave height is obtained from the zeroth moment of the spectrum as

$$H_s = 4\sqrt{m_0} = \int\int E(f,\theta)\mathrm{d}f\mathrm{d}\theta. \tag{2.9}$$

The mean zero-crossing period (the average time between crossings through zero for a wave record) is usually taken to be

$$\overline{T}_0 = \sqrt{\frac{m_0}{m_2}} = \sqrt{\frac{\int\int E(f,\theta)\mathrm{d}f\mathrm{d}\theta}{\int\int f^2 E(f,\theta)\mathrm{d}f\mathrm{d}\theta}}, \tag{2.10}$$

whereas another useful definition for the mean period is

$$T_{m_{01}} = \frac{m_0}{m_1} = \frac{\int\int E(f,\theta)\mathrm{d}f\mathrm{d}\theta}{\int\int f^1 E(f,\theta)\mathrm{d}f\mathrm{d}\theta}. \tag{2.11}$$

Finally, the mean wave direction can be derived from the spectrum as

$$\theta_m = \arctan\left(\frac{\int\int \sin\theta E(f,\theta)\mathrm{d}f\mathrm{d}\theta}{\int\int \cos\theta E(f,\theta)\mathrm{d}f\mathrm{d}\theta}\right). \tag{2.12}$$

2.3 Action balance equation

The basic equation formulated in terms of the energy spectrum $E(\mathbf{r}, t, f, \theta)$ is the energy balance equation which describes the conservation of wave energy (in an Eulerian approach) in geographic space $\mathbf{r} = (x, y)$, spectral space (f, θ) and time. When waves are propagating through inhomogeneous media however, i.e. time-varying depths and ambient ocean currents, wave energy is not conserved and the energy balance has to be reformulated in terms of the action density [14],

$$N = E/\sigma, \tag{2.13}$$

where σ (rad Hz) is the radian relative or intrinsic frequency, i.e. the frequency of the waves on a frame of reference moving with the velocity of the ocean current. The relationship between the absolute and relative frequencies is,

$$\omega = \sigma + \mathbf{k} \cdot \mathbf{V}, \tag{2.14}$$

where $\mathbf{k}$ is the wave number vector and $\mathbf{V}$ the velocity of the ocean current. The second term in equation (2.14) represents the Doppler shift, as the waves are carried by the current velocity. The dispersion relationship (see equation (2.6)) in this relative frame of reference still holds true, reformulated now in terms of the intrinsic frequency,

$$\sigma^2 = gk\tanh(kd). \tag{2.15}$$

The action balance equation then reads,

$$\frac{\partial N}{\partial t} + \nabla \cdot [(\mathbf{c_g} + \mathbf{V})N] + \frac{\partial c_\sigma N}{\partial \sigma} + \frac{\partial c_\theta N}{\partial \theta} = \frac{S_{\mathrm{tot}}}{\sigma}. \tag{2.16}$$

The left hand side of the action balance equation is the adiabatic part and conserves the total action in non-homogeneous media with variable currents and depths. It

represents the propagation of action in geographical space, with velocity $\mathbf{c_g} + \mathbf{V}$ and spectral space, with c_σ being the speed of propagation of action in frequency (frequency shifting due to wave-current interactions) and c_θ being the speed of propagation of action in angle (depth and current induced refraction). The right hand side of the equation contains a number of source and sink terms S_{tot}, which approximate the non-linear processes of wave generation and evolution, i.e. wind input, non-linear wave-wave transfers and wave dissipation.

2.3.1 Propagation in geographical space

The propagation speed of the surface wave profile for each frequency component is called phase speed (m) and given by

$$c = \frac{g}{\omega} \tanh(kd). \tag{2.17}$$

Of more importance, however, is the group speed, which represents the speed with which wave energy propagates and is given by

$$c_g = nc, \tag{2.18}$$

where

$$n = \frac{1}{2}\left(1 + \frac{2kd}{\sinh(2kd)}\right). \tag{2.19}$$

Thus, in the absence of currents, wave energy would move with the group velocity which is normal to the wave crest, i.e. in the wave direction. This is not the case in the presence of currents, however, since currents essentially dislocate the waves. In a frame of reference moving with the velocity of the ocean current, the relative group velocity would still be perpendicular to the wave crest. In an absolute frame of reference, however, the absolute group velocity is

$$\mathbf{c}_{g,\text{abs}} = \mathbf{c}_{g,\text{rel}} + \mathbf{V}. \tag{2.20}$$

Using equations (2.18) and (2.19) the relative group velocity becomes

$$c_{g,\mathrm{rel}} = c_g = \frac{1}{2}\left(1 + \frac{2kd}{\sinh(2kd)}\right)\sqrt{\frac{g\tanh(kd)}{k}}. \tag{2.21}$$

The subscript from the relative group velocity is henceforth dropped for simplicity. In the case of Cartesian coordinates the relative group velocity becomes

$$\mathbf{c}_g = (c_g\cos(\theta), c_g\sin(\theta)), \tag{2.22}$$

with θ being the wave direction measured counter-clock-wise from the positive $x-$axis. Given also that the velocity vector is $\mathbf{V} = (V_x, V_y)$, the absolute velocity with which action propagates in geographic space becomes

$$\mathbf{c}_{g,\mathrm{abs}} = \mathbf{c}_g + \mathbf{V} = (c_g\cos(\theta) + V_x, c_g\sin(\theta) + V_y)\,. \tag{2.23}$$

2.3.2 Propagation in frequency

In the special case when waves interact with a constant current in water of constant depth (in space and time), both the relative and the absolute frequency will remain constant. If these quantities vary horizontally or in time however, then these frequencies will also vary.

In terms of the spectrum, this means that action will shift through the frequency dimension. This is represented in the action balance equation with the advection in frequency, or $\partial\left(c_\sigma N\right)/\partial\sigma$. The rate of change of relative frequency in a frame of reference moving with the wave action is

$$c_\sigma = \frac{d\sigma}{dt} = \frac{\partial\sigma}{\partial d}\left[\frac{\partial d}{\partial t} + \mathbf{V}\cdot\nabla d\right] - c_g\mathbf{k}\cdot\frac{\partial\mathbf{V}}{\partial s}, \tag{2.24}$$

where s is a coordinate in the direction of θ, i.e. in the wave direction and $\mathbf{k} = (k\cos(\theta), k\sin(\theta))$ is the wave number vector. The partial derivative of relative frequency over depth, is calculated with the use of the dispersion relationship (see equation 2.15) as

$$\frac{\partial\sigma}{\partial d} = \frac{\sigma k}{\sinh(2kd)}. \tag{2.25}$$

The three terms of equation (2.24) reveal three distinct mechanisms responsible for changes in the relative frequency. The first is the effect of the wave action facing a time-dependent water depth. The second relates to the effect of the current moving the waves across a spatially varying water depth, while the third is the result of waves moving with a spatially varying current.

Finally, casting equation (2.24) in Cartesian coordinates gives

$$c_\sigma = \frac{\sigma k}{\sinh(2kd)}\left[\frac{\partial d}{\partial t} + V_x\frac{\partial d}{\partial x} + V_y\frac{\partial d}{\partial y}\right] - c_g k\left(\cos^2(\theta)\frac{\partial V_x}{\partial x} + \cos(\theta)\sin(\theta)\frac{\partial V_x}{\partial y} + \cos(\theta)\sin(\theta)\frac{\partial V_y}{\partial x} + \sin^2(\theta)\frac{\partial V_y}{\partial y}\right). \tag{2.26}$$

2.3.3 Propagation in angle

The change in the direction of wave propagation translates to action shifting through the angular dimension. This is represented by the $\partial\left(c_\theta N\right)/\partial\theta$ advection term of the action balance equation, where $c_\theta = d\theta/dt$ is the rate of change of the wave direction. This is expressed as

$$c_\theta = \frac{d\theta}{dt} = -\frac{1}{k}\Big[\frac{\partial\sigma}{\partial d}\frac{\partial d}{\partial m} + \mathbf{k}\cdot\frac{\partial \mathbf{u}}{\partial m}\Big]. \tag{2.27}$$

Here m is a coordinate perpendicular to the wave direction. Equation (2.27) has two terms and thus two discrete mechanisms affecting the direction of wave energy. These are depth-induced refraction and current-induced refraction respectively.

Casting this into Cartesian coordinates gives

$$c_\theta = \frac{\sigma}{\sinh(2kd)}\left(\sin(\theta)\frac{\partial d}{\partial x} - \cos(\theta)\frac{\partial d}{\partial y}\right) + \cos(\theta)\sin(\theta)\frac{\partial V_x}{\partial x} - \cos^2(\theta)\frac{\partial V_x}{\partial y} + \sin^2(\theta)\frac{\partial V_y}{\partial x} - \sin(\theta)\cos(\theta)\frac{\partial V_y}{\partial y}. \tag{2.28}$$

It is worth noting here that the wave direction can also change due to diffraction, i.e. the turning of the waves towards an area with a lower energy content. A proper

representation of diffraction, however, requires the phase information, which, as mentioned earlier, is dropped in the random phase/amplitude model. Diffraction is not included in this work, however, for a phase-decoupled approximation of diffraction in spectral wave models the reader can refer to [42].

2.4 Source terms

In the most general form, the source terms model the processes of wave generation, wave dissipation and wave-wave interactions,

$$S_{\text{tot}} = S_{\text{in}} + S_{\text{nl4}} + S_{\text{nl3}} + S_{\text{ds,wc}} + S_{\text{ds,br}} + S_{\text{ds,fr}}, \tag{2.29}$$

where S_{in} represents the wave growth by wind, S_{nl4} the non-linear four-wave interactions (quadruplets), S_{nl3} the non-linear three-wave interactions (triads), $S_{\text{ds,wc}}$ the wave dissipation due to white-capping, $S_{\text{ds,br}}$ the wave dissipation due to depth-induced breaking and $S_{\text{ds,fr}}$ the wave dissipation due to bottom friction.

Most of these processes are not well understood, which means that their form in the action balance equation is parametrised (based on observations, semi-empirical equations and calibration). In fact even four-wave interactions, for which exact calculations can be performed, are approximated in operational spectral wave models, due to the computational cost of an exact calculation. This means that there are various forms for each of these source terms available and as the understanding of these processes gets better and the computational capacity higher, more versions are expected to emerge.

It is beyond the scope of this work to present the progress in the modelling of each of these processes or improve their framework. Thus, here only the implemented form of the source terms is presented. Finally, it is worth noting that bottom friction was not included in this work and is, thus, omitted here.

2.4.1 Wind input

The general form of the source term for wind input is based on two distinct mechanisms. The initial growth of waves is described by Phillips [64], who suggested that water waves are formed by resonating with wind-induced pressure waves on

the water surface. Then, after the initial waves have been generated the Miles [60] positive-feedback mechanism becomes dominant, which is based on the wind-induced pressure differential between the windward and leeward side of a wave crest. The source terms reads

$$S_{\text{in}}(\sigma,\theta) = \alpha + \beta E(\sigma,\theta), \tag{2.30}$$

where α is the linear growth (linear in time) due to Phillips and βE the exponential growth (exponential in time) due to Miles.

The linear growth is represented by the expression of Cavaleri and Malanotte-Rizzoli [20], with a cut-off introduced by Tolman [85] to only allow for wave growth in the frequency region above the Pierson-Moskowitz frequency. The linear growth term is

$$\alpha = \begin{cases} \frac{1.5\times10^{-3}}{2\pi g^2}[u_* \cos(\theta-\theta_{\text{wind}})]^4 G, & \text{for } |\theta-\theta_{\text{wind}}| \leq 90^\circ, \\ 0, & \text{for } |\theta-\theta_{\text{wind}}| > 90^\circ, \end{cases} \tag{2.31}$$

where θ_{wind} is the wind direction, u_* is the friction velocity and G the cut-off frequency filter. The friction velocity is generally calculated by

$$u_*^2 = C_D U_{10}^2, \tag{2.32}$$

where U_{10} is the wind speed at an elevation of 10 m and C_D is the wind-drag coefficient. Here the WAM Cycle III (WAM III) formulation was implemented, which uses the expression of Wu [95] for the calculation of C_D,

$$C_D = \begin{cases} 1.2875 \times 10^{-3}, & \text{for } U_{10} < 7.5\,\text{m}\,\text{s}^{-1}, \\ (0.8 + 0.065 U_{10}) \times 10^{-3}, & \text{for } U_{10} \geq 7.5\,\text{m}\,\text{s}^{-1}. \end{cases} \tag{2.33}$$

Finally the cut-off frequency filter is

$$G = \exp[-(\sigma/\sigma^*_{\text{PM}})^{-4}], \tag{2.34}$$

$$\sigma^*_{\text{PM}} = 2\pi \frac{0.13g}{28u_*}, \tag{2.35}$$

where σ_{PM} is the Pierson-Moskowitz frequency, or the equilibrium frequency for the fully developed sea state according to Pierson and Moskowitz [65].

For the exponential growth the (WAM III) formulation for the term β comes from

Snyder et al. [78] and Komen et al. [49],

$$\beta = \max\Big[0, 0.25\frac{\rho_{\text{air}}}{\rho_{\text{water}}}\Big(28\frac{u_*}{c}\cos(\theta - \theta_{wind}) - 1\Big)\Big]\sigma, \tag{2.36}$$

where ρ_{air} and ρ_{water} are the densities of air and water respectively and c is the phase velocity.

2.4.2 White-capping

For white-capping the pulse model of Hasselmann [36] is implemented, which treats each white-cap as a pressure pulse on the leeward side of a crest. Thus, each white-cap (in an almost opposite mechanism to the positive-feedback of Miles for the exponential wind-growth, see section 2.4.1) removes energy from the wave.

The corresponding source term reads [91]

$$S_{\text{ds,wc}}(\sigma, \theta) = -\mu k E(\sigma, \theta), \tag{2.37}$$

where μ is given by

$$\mu = C_{\text{wc}}\left((1-n) + n\frac{k}{\tilde{k}}\right)\left(\frac{\tilde{s}}{\tilde{s}_{\text{PM}}}\right)^p \frac{\tilde{\sigma}}{\tilde{k}}. \tag{2.38}$$

Here $\tilde{s}$ is the overall mean wave steepness $\tilde{s} = \tilde{k}\sqrt{E_{\text{tot}}}$ [45], $\tilde{s}_{\text{PM}}$ is the overall mean wave steepness of the Pierson-Moskowitz spectrum $\tilde{s}_{\text{PM}} = \sqrt{3.02 \times 10^{-3}}$ [65], while $\tilde{\sigma}$, $\tilde{k}$ and E_{tot} are the mean relative frequency, mean wave number and total energy (or the zeroth moment) given by [91]

$$\tilde{\sigma} = \left[\frac{\int_0^{2\pi}\int_0^{\infty} E(\sigma,\theta)d\sigma d\theta}{\int_0^{2\pi}\int_0^{\infty} \sigma^{-1}E(\sigma,\theta)d\sigma d\theta}\right], \tag{2.39}$$

$$\tilde{k} = \left[\frac{\int_0^{2\pi}\int_0^{\infty} E(\sigma,\theta)d\sigma d\theta}{\int_0^{2\pi}\int_0^{\infty} k^{-1/2}E(\sigma,\theta)d\sigma d\theta}\right]^2, \tag{2.40}$$

$$E_{\text{tot}} = m_0 = \int_0^{2\pi} \int_0^{\infty} E(\sigma, \theta) d\sigma d\theta. \tag{2.41}$$

Finally C_{wc}, p and n are tunable coefficients. For the WAM III formulations used here, these are $C_{wc} = 2.36 \times 10^{-5}$, $p = 4$, $n = 0$ [91]. However, as noted by Rogers et al. [74], setting $n = 1$ actually leads to a better estimation of the mean frequencies for SWAN and, thus, the default parameter for SWAN is set equal to $n = 1$ [81]. Hence, for the test cases where Fluidity-SW is compared to SWAN with white-capping activated, a value of $n = 1$ is used.

2.4.3 Four-wave interactions (quadruplets)

In deep water, four different wave components start exchanging energy amongst each other, if they fulfil the resonance conditions:

$$\begin{aligned} f_1 + f_2 &= f_3 + f_4, \\ \mathbf{k_1} + \mathbf{k_2} &= \mathbf{k_3} + \mathbf{k_4}. \end{aligned} \tag{2.42}$$

This is referred to as four-wave interactions or quadruplet wave-wave interactions. The analytical form for four-wave interaction, in the context of the random/phase amplitude model, has been given by Hasselmann [37, 35]. Writing it as a source term for wave number $\mathbf{k_4}$ gives

$$\begin{aligned} S_{\text{nl4}}(\mathbf{k_4}) = &\int\int\int\int T_1(\mathbf{k_1}, \mathbf{k_2}, \mathbf{k_1} + \mathbf{k_2} - \mathbf{k_4}) E(\mathbf{k_1}) E(\mathbf{k_2}) E(\mathbf{k_1} + \mathbf{k_2} - \mathbf{k_4}) \mathrm{d}\mathbf{k_1} \mathrm{d}\mathbf{k_2} \\ &- E(\mathbf{k_4}) \int\int\int\int T_2(\mathbf{k_1}, \mathbf{k_2}, \mathbf{k_4}) E(\mathbf{k_1}) E(\mathbf{k_2}) \mathrm{d}\mathbf{k_1} \mathrm{d}\mathbf{k_2}, \end{aligned} \tag{2.43}$$

where T_1 and T_2 represent the transfer functions, determining the strength of the non-linear energy transfer between the wave components.

Calculating the exact expression for four-wave interactions is too computationally demanding for operational wave models, which means that an approximate form

is necessary for the efficient incorporation of quadruplets into the action balance equation. To date the most successful attempt has been the introduction of the Discrete Interaction Approximation (DIA) by Hasselmann et al. [38].

Based on the principle of detailed balance, the DIA restricts the non-linear iterations for each wave component to just two configurations of quadruplets (one representative quadruplet and its mirror image). These are defined as

$$\begin{aligned} \sigma_1 &= \sigma_2 = \sigma, \\ \sigma_3 &= \sigma(1+\lambda) = \sigma^+, \\ \sigma_4 &= \sigma(1-\lambda) = \sigma^-, \end{aligned} \tag{2.44}$$

where $\lambda = 0.25$. For the first configuration, the directions of the wave number vectors with frequencies σ_3 and σ_4 are at an angle of $\theta_3 = -11.5°$ and $\theta_4 = 33.6°$ respectively, relative to the wave number vectors with frequencies $\sigma_1 = \sigma_2$, which are identical to each other in wave number and direction. The configuration of the second quadruplet is then the mirror image of the first, with $\theta_3 = 11.5°$ and $\theta_4 = -33.6°$.

The source term can be then written as

$$S_{\mathrm{nl4}}(\sigma,\theta) = S^{*}_{\mathrm{nl4}}(\sigma,\theta) + S^{**}_{\mathrm{nl4}}(\sigma,\theta), \tag{2.45}$$

where $S^{*}_{\mathrm{nl4}}(\sigma,\theta)$ is the first quadruplet and $S^{**}_{\mathrm{nl4}}(\sigma,\theta)$ the second, i.e. its mirror image. The expression for the first quadruplet is

$$S^{*}_{\mathrm{nl4}}(\sigma,\theta) = 2\delta S_{\mathrm{nl4}}(\alpha_1\sigma,\theta) - \delta S_{\mathrm{nl4}}(\alpha_2\sigma,\theta) - \delta S_{\mathrm{nl4}}(\alpha_3\sigma,\theta), \tag{2.46}$$

where

$$\begin{aligned} &\delta S_{\mathrm{nl4}}(\alpha_i\sigma,\theta) = C_{\mathrm{nl4}}(2\pi)^2 g^{-4}\left(\frac{\sigma}{2\pi}\right)^{11} \times \\ &\left[E^2(\alpha_i\sigma,\theta)\left[\frac{E(\alpha_i\sigma^+,\theta)}{(1+\lambda)^4} + \frac{E(\alpha_i\sigma^-,\theta)}{(1-\lambda)^4}\right] - 2\frac{E(\alpha_i\sigma,\theta)E(\alpha_i\sigma^+,\theta)E(\alpha_i\sigma^-,\theta)}{(1-\lambda^2)^4}\right]. \end{aligned} \tag{2.47}$$

Here $\alpha_1 = 1$, $\alpha_2 = (1 + \lambda)$ and $\alpha_3 = (1 - \lambda)$, while $C_{\mathrm{nl4}} = 3 \times 10^7$. The second quadruplet $S^{**}_{\mathrm{nl4}}(\sigma, \theta)$ is calculated with the same expression (equation (2.46)), but for the mirror directions.

Finally to extend the source term in shallow water, equation (2.45) is multiplied by a scaling factor R [48],

$$R = 1 + \frac{C_1}{k_{\mathrm{p}} d}(1 - C_2 k_{\mathrm{p}} d) \exp(C_3 k_{\mathrm{p}} d), \tag{2.48}$$

where $k_p = 0.75\tilde{k}$ is the peak wave number, $\tilde{k}$ the mean wave number (see equation (2.40)), $C_1 = 5.5$, $C_2 = 6/7$ and $C_3 = -1.25$.

2.4.4 Three-wave interactions (triads)

When waves enter very shallow waters, three-wave interactions (triads) become important. These resonant conditions can only be satisfied in the non-dispersive region and are, thus, not realisable in deep water.

A simple approximation for these interactions is the lumped-triad approximation (LTA) of Eldeberky [28], which defines the source term for three-wave interactions as the sum of a positive and a negative contribution

$$S_{\mathrm{nl3}}(\sigma, \theta) = S^{+}_{\mathrm{nl3}}(\sigma, \theta) + S^{-}_{\mathrm{nl3}}(\sigma, \theta), \tag{2.49}$$

with the positive contribution equal to

$$S^{+}_{\mathrm{nl3}}(\sigma, \theta) = \max\left[0, \alpha_{\mathrm{EB}} 2\pi J^2 c c_g |\sin\beta| \left[E^2(\sigma/2, \theta) - 2E(\sigma/2, \theta)E(\sigma, \theta)\right]\right]. \tag{2.50}$$

Here α_{EB} is a tunable coefficient and β is the biphase parameter approximated by

$$\beta = -\frac{\pi}{2} + \frac{\pi}{2} \tanh\left(\frac{0.2}{\mathrm{Ur}}\right), \tag{2.51}$$

where Ur is the Ursell number calculated as

$$\mathrm{Ur} = \frac{g}{8\sqrt{2}\pi^2 d^2} H_s T_{m_{01}}^2. \tag{2.52}$$

Here, H_s is the significant wave height and $T_{m_{01}}$ the mean period (see equation (2.11)). The interaction coefficient J in equation (2.50) is taken from Madsen and Sørensen [55],

$$J = \frac{k_{\sigma/2}^2 (gd + 2c_{\sigma/2}^2)}{k_\sigma d \left(gd + \frac{2}{15} g d^3 k_\sigma^2 - \frac{2}{5}\sigma^2 d^2\right)}. \tag{2.53}$$

Finally the negative contribution for the three-wave interactions source term, can be calculated in terms of the positive as

$$S_{\mathrm{nl3}}^-(\sigma, \theta) = -2 S_{\mathrm{nl3}}^+(2\sigma, \theta). \tag{2.54}$$

2.4.5 Depth-induced breaking

To model the process of depth-induced wave breaking in shallow waters, the bore model of Battjes and Janssen [8] is used. The mean rate of energy dissipation per unit area is

$$D_{\mathrm{tot}} = -\frac{1}{4} \alpha_{\mathrm{BJ}} Q_b \frac{\sigma_{m_{10}}}{2\pi} H_{\mathrm{max}}^2, \tag{2.55}$$

where the coefficient α_{BJ} is set equal to 1 and $\sigma_{m_{10}}$ is a mean frequency, i.e. the frequency calculated in terms of the first and zeroth moment of the spectrum

$$\sigma_{m_{10}} = \frac{m_1}{m_0} = \left[\frac{\int_0^{2\pi} \int_0^\infty \sigma E(\sigma, \theta) d\sigma d\theta}{\int_0^{2\pi} \int_0^\infty E(\sigma, \theta) d\sigma d\theta} \right]. \tag{2.56}$$

The fraction of breaking waves Q_b can be calculated, by making further assumptions about the probability distributions of the heights of the waves that have not broken, i.e. with wave heights bellow H_{max} [9]. The fraction can then be calculated by,

$$\frac{1 - Q_b}{\ln Q_b} = -\left(\frac{H_{\mathrm{rms}}}{H_{\mathrm{max}}} \right)^2, \tag{2.57}$$

where $H_{\mathrm{rms}} = \sqrt{8m_0}$ is the root-mean-square wave height. The maximum significant wave height H_{max} can be approximated by $H_{\mathrm{max}} = \gamma d$, where γ is the tunable breaking index, set equal to $\gamma = 0.73$ [9].

The final form of the source term for depth-induced breaking is derived by extending the expression of Eldeberky and Battjes [29] to account for directional spectra,

$$S_{\mathrm{ds,br}} = \frac{D_{\mathrm{tot}}}{E_{\mathrm{tot}}} E(\sigma, \theta). \tag{2.58}$$

Chapter

THREE

Discretisation

3.1 Introduction

The action balance equation is a non-linear, five dimensional, hyperbolic equation. It consist of an adiabatic part which represents the propagation of action in time, geographic space and spectral space (angle and frequency), as well as a set of source terms which represent the non-linear dynamics of waves in deep and shallow water:

$$\underbrace{\frac{\partial N}{\partial t}}_{\text{Time propagation}} + \underbrace{\nabla \cdot [(\mathbf{c_g} + \mathbf{V})N]}_{\text{advection in space}} + \underbrace{\frac{\partial c_\sigma N}{\partial \sigma}}_{\text{advection in frequency}} + \underbrace{\frac{\partial c_\theta N}{\partial \theta}}_{\text{advection in angle}} = \underbrace{\frac{S_{\text{tot}}}{\sigma}}_{\text{source terms}} . \tag{3.1}$$

In this work, following the framework of SWAN, the adiabatic part in all dimensions is discretised and integrated along with the source terms implicitly.

In the next sections, the discretisation of the system in every dimension is presented. First the linearisation of the source terms is explained followed by the discretisation of the system in time, frequency and angle respectively. Finally the system is discretised in geographic space (in Cartesian coordinates) and the whole discrete form of the action balance equation is formulated.

3.2 Source term linearisation

Before moving on to discretise the action balance equation first the source terms have to be appropriately treated, given that, except from the linear growth part of the wind input term (see section 2.4.1), they are nonlinear.

The general form for each of the source terms is

$$S = \phi N, \tag{3.2}$$

where ϕ is a complicated function of N (integral parameters of action density and action densities at other spectral components). The basic procedure is to cast S_{tot} in linear form and integrate it in the action balance equation.

In the WAM model, which was created to model non-stationary problems on oceanic scales, a semi-implicit time integration approach was introduced for the source terms in the action balance equation [91]. The source terms are linearised with a Taylor expansion and the explicit contributions are calculated from the previously available values of N in the time propagation scheme. In the SWAN model, however, which is used in many time-independent problems for coastal applications, an iterative procedure (non-linear iterations) was introduced to update the values of N in stationary simulations [100]. Here the same approach as in the SWAN model was implemented.

The linearisation chosen, is the same as that proposed by Booij et al. [13] for SWAN. Due to the complexity of the source terms, in most cases, ϕ can only be calculated from available values of N, which means that ϕ is always treated explicitly. In any given non-linear iteration step n, ϕ is calculated from the previous iteration step $n-1$. Here explicit and implicit refer to the approximation of the source term in the iteration procedure.

To ensure the stability of the linear system, depending on the sign of the source term different approaches are used [62]. The positive source terms, i.e. wind-input, the positive part of four-wave interactions and the positive part of three-wave interactions, are treated explicitly

$$S^n_{\text{pos}} = S^n_{\text{in}} + S^n_{\text{nl4}_{\text{pos}}} + S^n_{\text{nl3}_{\text{pos}}} \approx \phi^{n-1}_{\text{pos}} N^{n-1}. \tag{3.3}$$

For negative source terms, i.e. white-capping, the negative part of four-wave interactions and the negative part of three-wave interactions, an implicit approach is used (or more precisely a semi-implicit approach given that ϕ is still calculated from the previous iteration step $n-1$)

$$S^n_{\text{neg}} = S^n_{\text{ds,w}} + S^n_{\text{nl4}_{\text{neg}}} + S^n_{\text{nl3}_{\text{neg}}} \approx \phi^{n-1}_{\text{neg}} N^n. \tag{3.4}$$

Finally for the strongly non-linear wave breaking term, a Taylor expansion is employed

$$S^n_{\text{ds,br}} \approx \phi^{n-1}_{\text{ds,br}} N^{n-1} + \left(\frac{\partial S_{\text{ds,br}}}{\partial N}\right)^{n-1} (N^n - N^{n-1}). \tag{3.5}$$

Treating the first term of the expansion more implicitly tends to make the system more robust [13],

$$S^n_{\text{ds,br}} \approx \phi^{n-1}_{\text{ds,br}} N^n + \left(\frac{\partial S_{\text{ds,br}}}{\partial N}\right)^{n-1} (N^n - N^{n-1}), \tag{3.6}$$

where the functional derivative of equation (3.6) can be calculated analytically from equation (2.58). The final form of the combined linearised source terms can be then written as

$$S^n_{\text{tot}} = S^n_{\text{tot,rhs}} + S^n_{\text{tot,lhs}} N^n, \tag{3.7}$$

where the subscripts rhs and lhs refer to right hand side and left hand side, or explicit and implicit contributions in the equation respectively. In equation (3.7) $S_{\text{tot,rhs}}$ contains all the positive source terms (equation (3.3)) and the right hand side contributions of wave breaking (equation 3.6), while $S_{\text{tot,lhs}}$ contains all the negative source terms (equation (3.4)) and the left hand side contributions of wave breaking (equation (3.6)). Both $S_{\text{tot,rhs}}$ and $S_{\text{tot,lhs}}$ are calculated at iteration level $n-1$ and are thus independent of the solution at level n.

In this work the source terms are incorporated within the solver directly with the adiabatic part of the action balance equation. The iteration process is thus applied to the whole system producing tentative results for N and S_{tot}, N^n and S^n_{tot} respectively. When the enforced convergence criteria have been satisfied, the tentative results

become final, i.e. $N = N^n$ and $S_{\text{tot}} = S^n_{\text{tot}}$.

To ensure the numerical stability of the iteration process, the maximum total change of action $N(\sigma, \theta)$ per each iteration, at each discrete wave component is limited to a fraction of the fully-developed Pierson-Moskowitz spectrum [65],

$$|\Delta N(\sigma, \theta)| = \gamma \frac{\alpha_{\text{PM}}}{2\sigma k^3 c_g}, \tag{3.8}$$

where $\alpha_{\text{PM}} = 0.0081$ is the Phillips constant for a Pierson-Moskowitz spectrum [48], γ is the fraction of the change, typically set to 10% [87], σ is the relative frequency, c_g the group velocity and k the wavenumber.

The use of this limiter has proven to be very successful in spectral wave modelling. The high frequency part of the spectrum has significantly shorter adjustment time scales than the low frequency bands, which are of most interest to modelling applications. Thus, the limiter was first introduced in the WAM model to limit the evolution of energy density in the time propagation and allow for economical calculations, at time steps larger than the time scales of wave growth [39]. In the SWAN model this limiter was included in the stationary solver, with the reasoning that a stationary problem is essentially a time marching problem with a pseudo-time step that does not generally match the evolution time scales of the source terms. As an alternative, under-relaxation can be used which essentially reduces the size of the pseudo-time step [100]. Here the iterations are stabilised with the use of the limiter.

It is beyond the scope of this work to explore the convergence behaviour of the limiter. Interesting discussions on the behaviour of various limiters can be found in [39, 87, 85]. A brief discussion on the convergence criteria however is necessary.

When one is interested in the steady state solution, a set of criteria must be satisfied to indicate that the numerical solutions have converged. In a stationary simulation for instance, where the non-linear problem is solved in an iterative manner, criteria must be defined to terminate the iteration process.

The iteration process should be terminated when a balance between accuracy and computational effort has been reached. In general, as noted by Booij et al. [13] for SWAN, in most cases the convergence tends to be monotonic up to a point after which occasionally the results tend to oscillate. Thus, the proposed stopping criteria for SWAN are based on the value of the absolute difference, the relative difference and the curvature (second derivative) of the significant wave height between

iterations, over a percentage of the active grid points [81].

In this work a fixed number of iterations is used for the convergence of the system. In all the stationary simulations that follow, the results are compared to the results of the SWAN model. The number of iterations used by SWAN to converge the non-linear problem with the default criteria is stated. Then, a higher fixed number of iterations is used for both codes to ensure that in the comparison of the codes, the presented results are converged.

3.3 Temporal discretisation

After the linearisation of the source terms the action balance equation reads

$$\begin{aligned}&\frac{\partial N(\mathbf{r},t,\sigma,\theta)}{\partial t}+\nabla\cdot\Big[\big(\mathbf{c_g}(\mathbf{r},t,\sigma,\theta)+\mathbf{V}(\mathbf{r},t)\big)N(\mathbf{r},t,\sigma,\theta)\Big]\\&+\frac{\partial c_\sigma(\mathbf{r},t,\sigma,\theta)N(\mathbf{r},t,\sigma,\theta)}{\partial\sigma}+\frac{\partial c_\theta(\mathbf{r},t,\sigma,\theta)N(\mathbf{r},t,\sigma,\theta)}{\partial\theta}-S_{\text{tot,lhs}}(\mathbf{r},t,\sigma,\theta)N(\mathbf{r},t,\sigma,\theta)\\&=S_{\text{tot,rhs}}(\mathbf{r},t,\sigma,\theta).\end{aligned}\tag{3.9}$$

To discretise in time, a first-order implicit finite difference scheme is used (backward Euler method [27]). If the continuous time-space is divided into discrete timelevels $\{t, t+1, ...\}$, then equation (3.9) is expressed as

$$\begin{aligned}&\frac{N(\mathbf{r},\sigma,\theta)^t-N(\mathbf{r},\sigma,\theta)^{t-1}}{\Delta t}+\nabla\cdot\Big[\big(\mathbf{c_g}(\mathbf{r},\sigma,\theta)^t+\mathbf{V}(\mathbf{r})^t\big)N(\mathbf{r},\sigma,\theta)^t\Big]\\&+\frac{\partial c_\sigma(\mathbf{r},\sigma,\theta)^tN(\mathbf{r},\sigma,\theta)^t}{\partial\sigma}+\frac{\partial c_\theta(\mathbf{r},\sigma,\theta)^tN(\mathbf{r},\sigma,\theta)^t}{\partial\theta}-S_{\text{tot,lhs}}(\mathbf{r},\sigma,\theta)^tN(\mathbf{r},\sigma,\theta)^t\\&=S_{\text{tot,rhs}}(\mathbf{r},\sigma,\theta)^t.\end{aligned}\tag{3.10}$$

If non-linear iterations are used in time-dependent problems, then at each iteration step n tentative values of N^n, $S^n_{\text{tot,rhs}}$ and $S^n_{\text{tot,lhs}}$ are produced. When the convergence criteria have been satisfied the tentative results become final and $N^t = N^n$.

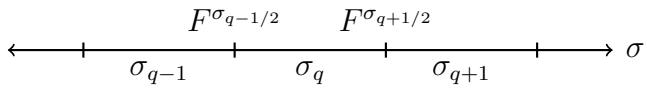


Figure 3.1: Example of a cell-centred control volume σ_q of the frequency dimension σ, with the flux $F^{\sigma_{q\pm1/2}}$ from the boundaries.

3.4 Frequency discretisation

For the frequency discretisation a control volume formulation (cell-centred finite volume) is used combined with a first-order upwind scheme. This provides a simple and stable framework before higher-order approximations are applied (such as the QUICKEST scheme [51]). The continuous frequency space is split into a series of discrete frequency control volumes $\{\sigma_q, \sigma_{q+1}, ...\}$. The action balance equation discretised in time and frequency is then expressed as

$$\begin{aligned}
&\frac{N(\mathbf{r},\theta)^{t,\sigma_q} - N(\mathbf{r},\theta)^{t-1,\sigma_q}}{\Delta t} + \nabla \cdot \left[\left(\mathbf{c_g}(\mathbf{r},\theta)^{t,\sigma_q} + \mathbf{V}(\mathbf{r})^t \right) N(\mathbf{r},\theta)^{t,\sigma_q} \right] \\
&+ \frac{\left[c_\sigma(\mathbf{r},\theta)^t N(\mathbf{r},\theta)^t \right]^{\sigma_{q+1/2}} - \left[c_\sigma(\mathbf{r},\theta)^t N(\mathbf{r},\theta)^t \right]^{\sigma_{q-1/2}}}{\Delta\sigma} + \frac{\partial c_\theta(\mathbf{r},\theta)^{t,\sigma_q} N(\mathbf{r},\theta)^{t,\sigma_q}}{\partial\theta} \\
&- S_{\mathrm{tot,lhs}}(\mathbf{r},\theta)^{t,\sigma_q} N(\mathbf{r},\theta)^{t,\sigma_q} = S_{\mathrm{tot,rhs}}(\mathbf{r},\theta)^{t,\sigma_q},
\end{aligned} \tag{3.11}$$

where the fluxes $F = c_\sigma N$ from the boundaries $\sigma_{q-1/2}$ and $\sigma_{q+1/2}$ of control volume σ_q (see figure 3.1) are

$$\begin{aligned}
&F^{\sigma_{q-1/2}} = {c_\sigma}^{\sigma_{q-1/2}} N^{\sigma_{q-1/2}}; && F^{\sigma_{q+1/2}} = {c_\sigma}^{\sigma_{q+1/2}} N^{\sigma_{q+1/2}}, \\
&{c_\sigma}^{\sigma_{q-1/2}} = \left({c_\sigma}^{\sigma_{q-1}} + {c_\sigma}^{\sigma_q} \right)/2; && {c_\sigma}^{\sigma_{q+1/2}} = \left({c_\sigma}^{\sigma_q} + {c_\sigma}^{\sigma_{q+1}} \right)/2, \\
&N^{\sigma_{q-1/2}} = N^{\sigma_{q-1}}, \quad \text{if} \quad {c_\sigma}^{\sigma_q} \geq 0; && N^{\sigma_{q+1/2}} = N^{\sigma_q}, \quad \text{if} \quad {c_\sigma}^{\sigma_q} \geq 0, \\
&N^{\sigma_{q-1/2}} = N^{\sigma_q}, \quad \text{if} \quad {c_\sigma}^{\sigma_q} < 0; && N^{\sigma_{q+1/2}} = N^{\sigma_{q+1}}, \quad \text{if} \quad {c_\sigma}^{\sigma_q} < 0.
\end{aligned} \tag{3.12}$$

The frequency space is historically discretised with a logarithmic grid mainly to accommodate the DIA (see section 2.4.3). This is defined as

$$\frac{\Delta\sigma}{\sigma} = 0.1, \tag{3.13}$$

which is the resolution used initially to tune the DIA [90]. If the DIA is not activated then there is no restriction on the choice of $\Delta\sigma/\sigma$.

The frequency dimension spans the space $[0, \infty)$. However, the space is truncated between a low and high cut-off frequency. This is referred to as the prognostic part of the spectrum. Below the low cut-off point (typically set to $\approx 0.04\,\text{Hz}$ [13]) the spectrum is assumed to be zero. This is adequate as the spectrum is not expected to reach frequencies below this limit [85]. Above the high cut-off point (typically set to $\approx 1\,\text{Hz}$ [13]) a fixed diagnostic tail σ^{-m} is added to represent the spectrum at high frequencies. This allows for the non-linear interactions to be computed in the diagnostic region (i.e. energy is exchanged between the prognostic and diagnostic part of the spectrum) and is also used for calculating the integral parameters [91]. The value of the power m is dependent on the choice of the physical parametrisations used. Here since the WAM III formulations are implemented (see section 2.4) the power is set equal to 4 [91].

In the absence of currents or a time-dependent water depth, the flux in frequency space becomes zero and the frequencies are decoupled. Each monochromatic wave can be then solved independently. Otherwise, an iterative procedure needs to be followed to capture the interaction of the frequency groups (frequency shifting). This is essentially the application of a Gauss-Seidel algorithm in frequency.

3.5 Angular discretisation

The angular domain is periodic. Historically in spectral wave models it has been discretised with an isotropic distribution of angles from 0 to 2π. In this work a finite element expansion is used for its representation. An arbitrary angular discretisation is considered, in which θ is represented by the span of angular trial functions G_j, $j \in \{1, 2, ..., K\}$, such that

$$N(\mathbf{r}, \theta)^{t,\sigma_q} \approx \sum_{j=1}^{K} N_j(\mathbf{r})^{t,\sigma_q} G_j(\theta). \tag{3.14}$$

To derive the weak formulation of the problem a set of test functions is required. For this work the Galerkin method is used [30], in which the trial and test functions are chosen to be the same. Weighting equation (3.11) with the set of test functions G_i, $i \in \{1, 2, ..., K\}$ and integrating over the angular domain gives

$$\begin{aligned}
&\int_{\theta} G_i(\theta)\frac{N(\mathbf{r},\theta)^{t,\sigma_q} - N(\mathbf{r},\theta)^{t-1,\sigma_q}}{\Delta t}\mathrm{d}\theta + \int_{\theta} G_i(\theta)\nabla\cdot\Big[\big(\mathbf{c_g}(\mathbf{r},\theta)^{t,\sigma_q} + \mathbf{V}(\mathbf{r})^t\big)N(\mathbf{r},\theta)^{t,\sigma_q}\Big]\mathrm{d}\theta \\
&+ \int_{\theta} G_i(\theta)\frac{\big[c_\sigma(\mathbf{r},\theta)^t N(\mathbf{r},\theta)^t\big]^{\sigma_{q+1/2}} - \big[c_\sigma(\mathbf{r},\theta)^t N(\mathbf{r},\theta)^t\big]^{\sigma_{q-1/2}}}{\Delta\sigma}\mathrm{d}\theta \\
&+ \int_{\theta} G_i(\theta)\frac{\partial c_\theta(\mathbf{r},\theta)^{t,\sigma_q} N(\mathbf{r},\theta)^{t,\sigma_q}}{\partial\theta}\mathrm{d}\theta - \int_{\theta} G_i(\theta) S_{\mathrm{tot,lhs}}(\mathbf{r},\theta)^{t,\sigma_q} N(\mathbf{r},\theta)^{t,\sigma_q}\mathrm{d}\theta \\
&= \int_{\theta} G_i(\theta) S_{\mathrm{tot,rhs}}(\mathbf{r},\theta)^{t,\sigma_q}\mathrm{d}\theta, \quad \forall\ i \in \{1, 2, .., K\},
\end{aligned} \tag{3.15}$$

where θ is the one-dimensional angular coordinate. For the angular advection term in equation (3.15), applying the divergence theorem gives

$$\begin{aligned}
&\int_{\theta} G_i(\theta)\frac{\partial c_\theta(\mathbf{r},\theta)^{t,\sigma_q} N(\mathbf{r},\theta)^{t,\sigma_q}}{\partial\theta}\mathrm{d}\theta = \\
&\int_{S} G_i(\theta) c_\theta(\mathbf{r},\theta)^{t,\sigma_q} N(\mathbf{r},\theta)^{t,\sigma_q}\hat{\mathbf{n}}_\theta dS - \int_{\theta}\frac{\mathrm{d}G_i(\theta)}{\mathrm{d}\theta} c_\theta(\mathbf{r},\theta)^{t,\sigma_q} N(\mathbf{r},\theta)^{t,\sigma_q}\mathrm{d}\theta, \\
&\quad \forall\ i \in \{1, 2, .., K\},
\end{aligned} \tag{3.16}$$

where S corresponds to the boundary surface of the angular domain θ and $\hat{\mathbf{n}}_\theta$ to the outward normal unit vector. Given that the domain θ is one-dimensional S reduces to a point and $\hat{\mathbf{n}}_\theta$ is 1 and -1 on the two boundary nodes of each angular element respectively (figure 3.2).

A first-order upwind scheme is applied to resolve the angular inter-element boundary conditions. This robust choice is used to ensure the successful implementation of the numerical schemes, due to its simplicity and numerical stability, before higher-order approximations are applied (such as the QUICKEST scheme [51]). For a specific

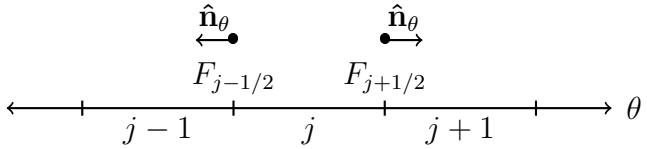


Figure 3.2: Example of an element j of the angular dimension θ, the angular flux $F_{j\pm1/2}$ and the normals $\hat{\mathbf{n}}_\theta$ at the element boundaries.

angular element j the flux $F = c_\theta N$ from the two boundaries at $j - \frac{1}{2}$ and $j + \frac{1}{2}$ (figure 3.2) is

$$\begin{aligned}
&F_{j-\frac{1}{2}} = c_{\theta j-\frac{1}{2}} N_{j-\frac{1}{2}}; && && F_{j+\frac{1}{2}} = c_{\theta j+\frac{1}{2}} N_{j+\frac{1}{2}}, && \\
&c_{\theta j-\frac{1}{2}} = \left(c_{\theta j-1} + c_{\theta j}\right)/2; && && c_{\theta j+\frac{1}{2}} = \left(c_{\theta j} + c_{\theta j+1}\right)/2, && \\
&N_{j-\frac{1}{2}} = N_{j-1}, && \text{if} \quad c_\theta \geq 0; && N_{j+\frac{1}{2}} = N_j, && \text{if} \quad c_\theta \geq 0, \\
&N_{j-\frac{1}{2}} = N_j, && \text{if} \quad c_\theta < 0; && N_{j+\frac{1}{2}} = N_{j+1}, && \text{if} \quad c_\theta < 0.
\end{aligned} \tag{3.17}$$

Finally, to evaluate the spatial advection term in equation (3.15), the group velocity is first expressed as the product of the unit vector and group speed,

$$\mathbf{c_g}(\mathbf{r},\theta)^{t,\sigma_q} = c_g(\mathbf{r})^{t,\sigma_q}\hat{\theta}, \tag{3.18}$$

where

$$\hat{\theta} = \left(\hat{\theta}_x, \hat{\theta}_y\right) = \left(\cos(\theta), \sin(\theta)\right). \tag{3.19}$$

Substituting equations (3.12), (3.14), (3.16), (3.17) and (3.18) into (3.15) and formulating the system in vector form, gives the system discretised in time and spectral space, i.e. angle and frequency

$$\begin{aligned}
&\frac{1}{\Delta t}\mathbf{M}\mathbf{N}(\mathbf{r})^{t,\sigma_q} + \nabla\cdot\left[\left(\mathbf{A}_\mathrm{s}c_g(\mathbf{r})^{t,\sigma_q} + \mathbf{M}\mathbf{V}(\mathbf{r})^t\right)\mathbf{N}(\mathbf{r})^{t,\sigma_q}\right] + \frac{1}{\Delta\sigma}\mathbf{H}_\sigma(\mathbf{r})^{t,\sigma_q}\mathbf{N}(\mathbf{r})^{t,\sigma_q} \\
&+ \mathbf{H}_\theta(\mathbf{r})^{t,\sigma_q}\mathbf{N}(\mathbf{r})^{t,\sigma_q} - \mathbf{H}_\mathrm{S}^\mathrm{lhs}(\mathbf{r})^{t,\sigma_q}\mathbf{N}(\mathbf{r})^{t,\sigma_q} = \mathbf{S}(\mathbf{r})^{t,\sigma_q},
\end{aligned} \tag{3.20}$$

where $\mathbf{S}$ is a vector of size K (number of angles) representing the numerical source, i.e. all the right hand side contributions to the system:

$$\mathbf{S}(\mathbf{r})^{t,\sigma_q} = \frac{1}{\Delta t}\mathbf{M}\mathbf{N}(\mathbf{r})^{t-1,\sigma_q} - \frac{1}{\Delta\sigma}\mathbf{H}_{\sigma}^{\mathrm{U}}(\mathbf{r})^{t,\sigma_q}\mathbf{N}(\mathbf{r})^{t,\sigma_{q-1}} - \frac{1}{\Delta\sigma}\mathbf{H}_{\sigma}^{\mathrm{D}}(\mathbf{r})^{t,\sigma_q}\mathbf{N}(\mathbf{r})^{t,\sigma_{q+1}} + \mathbf{H}_{\mathrm{S}}^{\mathrm{rhs}}(\mathbf{r})^{t,\sigma_q}. \tag{3.21}$$

The rest of the angular matrices are given by

$$\mathbf{A}_{\mathrm{s}} = (\mathbf{A}_{\mathrm{s},\mathbf{x}}, \mathbf{A}_{\mathrm{s},\mathbf{y}}), \quad \forall\, i \in \{1,2,...,K\}, \tag{3.22}$$

$$\mathbf{A}_{\mathrm{s},\mathbf{x}} = \sum_{j=1}^{K} \int_{\theta} G_i(\theta)\cos(\theta)G_j(\theta)\mathrm{d}\theta, \quad \forall\, i \in \{1,2,...,K\}, \tag{3.23}$$

$$\mathbf{A}_{\mathrm{s},\mathbf{y}} = \sum_{j=1}^{K} \int_{\theta} G_i(\theta)\sin(\theta)G_j(\theta)\mathrm{d}\theta, \quad \forall\, i \in \{1,2,...,K\}, \tag{3.24}$$

$$\mathbf{M} = \sum_{j=1}^{K} \int_{\theta} G_i(\theta)G_j(\theta)\mathrm{d}\theta, \quad \forall\, i \in \{1,2,...,K\}, \tag{3.25}$$

$$\mathbf{H}_{\theta} = \sum_{j=1}^{K} G_i(\theta)\Bigg[\Big(\max(c_{\theta_{j+\frac{1}{2}}},0) - \min(c_{\theta_{j-\frac{1}{2}}},0)\Big)G_j(\theta) + \min(c_{\theta_{j+\frac{1}{2}}},0)G_{j+1}(\theta) - \max(c_{\theta_{j-\frac{1}{2}}},0)G_{j-1}(\theta)\Bigg] + \sum_{j=1}^{K}\int_{\theta}\frac{dG_i(\theta)}{\mathrm{d}\theta}c_{\theta}(\mathbf{r},t,\theta)G_j(\theta)\mathrm{d}\theta, \quad \forall\, i \in \{1,2,...,K\}, \tag{3.26}$$

$$\mathbf{H}_{\sigma} = \sum_{j=1}^{K} \int_{\theta} G_i(\theta)\Big(\max({c_{\sigma}}^{\sigma_{q+1/2}},0) - (\min({c_{\sigma}}^{\sigma_{q-1/2}},0)\Big)G_j(\theta)\mathrm{d}\theta, \tag{3.27}$$

$$\forall\, i \in \{1,2,...,K\}, \tag{3.28}$$

$$\mathbf{H}_{\sigma}^{\mathrm{U}} = -\sum_{j=1}^{K} \int_{\theta} G_i(\theta)\Big(\max({c_{\sigma}}^{\sigma_{q-1/2}},0)\Big)G_j(\theta)\mathrm{d}\theta, \quad \forall\, i \in \{1,2,...,K\}, \tag{3.29}$$

$$\mathbf{H}_{\sigma}^{\mathrm{D}} = \sum_{j=1}^{K} \int_{\theta} G_i(\theta)\Big(\min({c_{\sigma}}^{\sigma_{q+1/2}},0)\Big)G_j(\theta)\mathrm{d}\theta, \quad \forall\, i \in \{1,2,...,K\}, \tag{3.30}$$

$$\mathbf{H}_{\mathrm{S}}^{\mathrm{lhs}} = \sum_{j=1}^{K} \int_{\theta} G_i(\theta) S_{\mathrm{tot,lhs}} G_j(\theta) \mathrm{d}\theta, \quad \forall\ i \in \{1, 2, ..., K\}, \tag{3.31}$$

$$\mathbf{H}_{\mathrm{S}}^{\mathrm{rhs}} = \sum_{j=1}^{K} \int_{\theta} G_i(\theta) S_{\mathrm{tot,rhs}} \mathrm{d}\theta, \quad \forall\ i \in \{1, 2, ..., K\}. \tag{3.32}$$

Here $\mathbf{A}_{\mathrm{s}}$ is a vector of matrices, with $\mathbf{A}_{\mathrm{s,x}}, \mathbf{A}_{\mathrm{s,y}}$ being the $K \times K$ angular streaming matrices in the $x-$ and $y-$ direction respectively. These matrices handle the advection in geographic space for each angular component. $\mathbf{M}$ is the $K \times K$ angular mass matrix. $\mathbf{H}_{\theta}$ is the $K \times K$ angular matrix representing the advection in angle, i.e. refraction. $\mathbf{H}_{\sigma}$ is the $K \times K$ angular matrix representing advection in frequency space, i.e. frequency shifting, with $\mathbf{H}_{\sigma}^{\mathrm{U}}$ and $\mathbf{H}_{\sigma}^{\mathrm{D}}$ bringing the frequency shifting contributions from the previous and next frequency group respectively. Finally $\mathbf{H}_{\mathrm{S}}^{\mathrm{lhs}}$ is a $K \times K$ matrix containing the left hand side contributions of the source terms and $\mathbf{H}_{\mathrm{S}}^{\mathrm{rhs}}$ is a vector of size K containing the right hand side contributions of the source terms for each angle.

When using a $P0$ angular discretisation (i.e. the shape of each basis function is assumed to be constant over a single element and zero elsewhere) all the $K \times K$ matrices are diagonal, except for the angular refraction $\mathbf{H}_{\theta}$ which couples each angle which each two neighbouring angles. This is the case because a first -order upwind scheme is used in angle, as higher order upwind schemes would extend this stencil.

3.6 Spatial discretisation

Owing to the hyperbolic nature of the action balance equation, schemes that exhibit upwind bias are preferable such as discontinuous finite element, Petrov-Galerkin or Taylor-Galerkin methods. As an alternative, here the spatial dimensions are discretised with a sub-grid scale finite element method (SGS). The SGS method combines the benefits of continuous Galerkin formulations, i.e. low computational cost, with discontinuous Galerkin formulations, i.e. accuracy and stability. This is based on the work of Buchan et al. [15], who used this methodology for the spatial discretisation of the Boltzmann transport equation.

To formulate the model, the spatial domain $V \subset \mathbb{R}^2$ is partitioned into a set of disjoint sub-domains or elements V_j, $j \in \{1, 2, ..., \eta\}$. The full solution $\mathbf{N}(\mathbf{r})$ is then

decomposed into two components

$$\mathbf{N}(\mathbf{r}) = \mathbf{\Phi}(\mathbf{r}) + \mathbf{\Theta}(\mathbf{r}), \tag{3.33}$$

where $\mathbf{\Phi}$ and $\mathbf{\Theta}$ represent the coarse scale (continuous) and fine SGS scale (discontinuous) components of the solution respectively. The coarse component's approximation lies in a continuous finite element space, spanned by the continuous trial functions P_j, $j \in \{1, 2, ..., \eta_P\}$,

$$\mathbf{\Phi}(\mathbf{r}) \approx \tilde{\mathbf{\Phi}} = \sum_{j=1}^{\eta_P} \mathbf{P}_j(\mathbf{r})\mathbf{\Phi_j}, \tag{3.34}$$

while the fine scale approximation lies in a discontinuous finite element space, spanned by the discontinuous trial functions Q_j, $j \in \{1, 2, ..., \eta_Q\}$,

$$\mathbf{\Theta}(\mathbf{r}) \approx \tilde{\mathbf{\Theta}} = \sum_{j=1}^{\eta_Q} \mathbf{Q}_j(\mathbf{r})\mathbf{\Theta_j}. \tag{3.35}$$

Given that $\mathbf{\Phi}$ and $\mathbf{\Theta}$ are angular vectors of size K, the terms $\mathbf{P}_j$ and $\mathbf{Q}_j$ are $K \times K$ diagonal matrices, containing the spatial basis functions for each angular element. By weighting equation (3.20) using both sets of test functions $\mathbf{P}_i$ and $\mathbf{Q}_i$ and integrating over the spatial domain a system of $\eta_P + \eta_Q$ equations is formed, which is defined by

$$\int_V \mathbf{P}_i \Bigg[\frac{1}{\Delta t}\mathbf{M}\mathbf{N}(\mathbf{r})^{t,\sigma_q} + \nabla \cdot \Big[\big(\mathbf{A}_s c_g(\mathbf{r})^{t,\sigma_q} + \mathbf{M}\mathbf{V}(\mathbf{r})^t\big)\mathbf{N}(\mathbf{r})^{t,\sigma_q} \Big] + \frac{1}{\Delta\sigma}\mathbf{H}_\sigma(\mathbf{r})^{t,\sigma_q}\mathbf{N}(\mathbf{r})^{t,\sigma_q}$$
$$+ \mathbf{H}_\theta(\mathbf{r})^{t,\sigma_q}\mathbf{N}(\mathbf{r})^{t,\sigma_q} - \mathbf{H}_{\mathrm{S}}^{\mathrm{lhs}}(\mathbf{r})^{t,\sigma_q}\mathbf{N}(\mathbf{r})^{t,\sigma_q} \Bigg] \mathrm{d}V = \int_V \mathbf{P}_i \mathbf{S}(\mathbf{r})^{t,\sigma_q} \mathrm{d}V, \quad \forall \quad i \in \{1, 2, ..., \eta_P\}, \tag{3.36}$$

and

$$\int_V \mathbf{Q}_i \Bigg[\frac{1}{\Delta t}\mathbf{M}\mathbf{N}(\mathbf{r})^{t,\sigma_q} + \nabla \cdot \Big[\big(\mathbf{A}_{\mathrm{s}} c_g(\mathbf{r})^{t,\sigma_q} + \mathbf{M}\mathbf{V}(\mathbf{r})^t\big)\mathbf{N}(\mathbf{r})^{t,\sigma_q} \Big] + \frac{1}{\Delta\sigma}\mathbf{H}_\sigma(\mathbf{r})^{t,\sigma_q}\mathbf{N}(\mathbf{r})^{t,\sigma_q}$$
$$+ \mathbf{H}_\theta(\mathbf{r})^{t,\sigma_q}\mathbf{N}(\mathbf{r})^{t,\sigma_q} - \mathbf{H}_{\mathrm{S}}^{\mathrm{lhs}}(\mathbf{r})^{t,\sigma_q}\mathbf{N}(\mathbf{r})^{t,\sigma_q} \Bigg] \mathrm{d}V = \int_V \mathbf{Q}_i \mathbf{S}(\mathbf{r})^{t,\sigma_q} \mathrm{d}V \quad \forall \quad i \in \{1, 2, ..., \eta_Q\}. \tag{3.37}$$

Before finalising the discrete form of the system, appropriate boundary conditions for the coarse (3.36) and SGS (3.37) equations have to be defined. First the divergence theorem is applied in the advection term of the coarse set of equations (3.36)

$$\begin{aligned} \int_V \mathbf{P}_i \nabla \cdot \Big[\big(\mathbf{A}_{\mathrm{s}} c_g(\mathbf{r})^{t,\sigma_q} + \mathbf{M}\mathbf{V}(\mathbf{r})^t\big)\mathbf{N}(\mathbf{r})^{t,\sigma_q} \Big] \mathrm{d}V = \\ \int_\Gamma \mathbf{P}_i \Big[\Big(\mathbf{A}_{\mathrm{s}} c_g(\mathbf{r})^{t,\sigma_q} + \mathbf{M}\mathbf{V}(\mathbf{r})^t\Big) \cdot \mathbf{n} \Big] \mathbf{N}(\mathbf{r})^{t,\sigma_q} \mathrm{d}\Gamma \\ - \int_V \nabla \mathbf{P}_i \cdot \Big(\mathbf{A}_{\mathrm{s}} c_g(\mathbf{r})^{t,\sigma_q} + \mathbf{M}\mathbf{V}(\mathbf{r})^t\Big)\mathbf{N}(\mathbf{r})^{t,\sigma_q} \mathrm{d}V, \end{aligned} \tag{3.38}$$

where the first term is the surface boundary integral and $\mathbf{n}$ is the outwards pointing unit normal vector, perpendicular to each face of the elements' boundaries. Applying the sub-grid scale decomposition (3.33) to the surface integral of equation (3.38) gives

$$\begin{aligned} \int_\Gamma \mathbf{P}_i \Big[\Big(\mathbf{A}_{\mathrm{s}} c_g(\mathbf{r})^{t,\sigma_q} + \mathbf{M}\mathbf{V}(\mathbf{r})^t\Big) \cdot \mathbf{n} \Big] \mathbf{N}(\mathbf{r})^{t,\sigma_q} \mathrm{d}\Gamma = \\ \int_\Gamma \mathbf{P}_i \Big[\Big(\mathbf{A}_{\mathrm{s}} c_g(\mathbf{r})^{t,\sigma_q} + \mathbf{M}\mathbf{V}(\mathbf{r})^t\Big) \cdot \mathbf{n} \Big] \tilde{\mathbf{\Phi}}(\mathbf{r})^{t,\sigma_q} \mathrm{d}\Gamma \\ + \int_\Gamma \mathbf{P}_i \Big[\Big(\mathbf{A}_{\mathrm{s}} c_g(\mathbf{r})^{t,\sigma_q} + \mathbf{M}\mathbf{V}(\mathbf{r})^t\Big) \cdot \mathbf{n} \Big] \tilde{\mathbf{\Theta}}(\mathbf{r})^{t,\sigma_q} \mathrm{d}\Gamma, \end{aligned} \tag{3.39}$$

where the second term of equation (3.39) is eliminated with the sub-grid scale boundary condition $\tilde{\mathbf{\Theta}} = 0$.

Thus, in terms of the coarse system the discontinuous approximation does not communicate across elements, resulting in only external boundary conditions (external referring to the spatial domain's boundaries). Typically external boundary conditions are fully absorbing in spectral wave models, i.e. the incoming flux is set to zero. For incoming boundary conditions on the other hand, the incoming flux is set to a desired value.

For the fine system (3.37) the divergence theorem is only applied to the advective flux of the discontinuous component $\tilde{\mathbf{\Theta}}$,

$$\begin{aligned}\int_V \mathbf{Q}_i \nabla \cdot \Big[\big(\mathbf{A}_{\mathrm{s}} c_g(\mathbf{r})^{t,\sigma_q} + \mathbf{MV}(\mathbf{r})^t\big)\mathbf{N}(\mathbf{r})^{t,\sigma_q}\Big]\mathrm{d}V = \int_V \mathbf{Q}_i \nabla \cdot \Big[\big(\mathbf{A}_{\mathrm{s}} c_g(\mathbf{r})^{t,\sigma_q} \\ + \mathbf{MV}(\mathbf{r})^t\big)\tilde{\mathbf{\Phi}}(\mathbf{r})^{t,\sigma_q}\Big]\mathrm{d}V + \int_\Gamma \mathbf{Q}_i \Big[\Big(\mathbf{A}_{\mathrm{s}} c_g(\mathbf{r})^{t,\sigma_q} + \mathbf{MV}(\mathbf{r})^t\Big)\cdot \mathbf{n}\Big]\tilde{\mathbf{\Theta}}(\mathbf{r})^{t,\sigma_q}\mathrm{d}\Gamma \\ - \int_V \nabla \mathbf{Q}_i \cdot \Big(\mathbf{A}_{\mathrm{s}} c_g(\mathbf{r})^{t,\sigma_q} + \mathbf{MV}(\mathbf{r})^t\Big)\tilde{\mathbf{\Theta}}(\mathbf{r})^{t,\sigma_q}\mathrm{d}V.\end{aligned} \tag{3.40}$$

Thus, the only surface integral present on the fine system is on the discontinuous solution $\tilde{\mathbf{\Theta}}$. This integral is then split into the incoming and outgoing flux at each element's boundary. Finally the surface integral containing the incoming flux is eliminated by setting it equal to zero

$$\begin{aligned}\int_\Gamma \mathbf{Q}_i \Big[\Big(\mathbf{A}_{\mathrm{s}} c_g(\mathbf{r})^{t,\sigma_q} + \mathbf{MV}(\mathbf{r})^t\Big)\cdot \mathbf{n}\Big]\tilde{\mathbf{\Theta}}(\mathbf{r})^{t,\sigma_q}\mathrm{d}\Gamma = \\ \int_{\Gamma_{\mathrm{out}}} \mathbf{Q}_i \Big[\Big(\mathbf{A}_{\mathrm{s}} c_g(\mathbf{r})^{t,\sigma_q} + \mathbf{MV}(\mathbf{r})^t\Big)\cdot \mathbf{n}\Big]\tilde{\mathbf{\Theta}}(\mathbf{r})^{t,\sigma_q}\mathrm{d}\Gamma.\end{aligned} \tag{3.41}$$

The result of this approximation is that the sub-grid variables will only receive information through surfaces from the continuous solution $\tilde{\mathbf{\Phi}}$. This is essentially where the SGS approximation differs from a full discontinuous scheme. On each internal face (internal in the spatial domain) only the outgoing information is included, while the elements exchange information through the continuous solution. Additionally as the support of the discontinuous weighting functions is strictly limited to a single element, the integration over the domain $\mathbf{V}$ can be restricted to the weighting

function's respective element $\mathbf{V}_e$.

Combining the results of the coarse and fine scale systems, the SGS formulation of the action balance equation takes the form of the following linear system

$$\begin{pmatrix} \mathbf{A} & \mathbf{B} \\ \mathbf{C} & \mathbf{D} \end{pmatrix} \begin{pmatrix} \tilde{\mathbf{\Phi}} \\ \tilde{\mathbf{\Theta}} \end{pmatrix} = \begin{pmatrix} \tilde{\mathbf{S}}_{\mathbf{\Phi}} \\ \tilde{\mathbf{S}}_{\mathbf{\Theta}} \end{pmatrix}, \tag{3.42}$$

or equivalently

$$\mathbf{A}\tilde{\mathbf{\Phi}} + \mathbf{B}\tilde{\mathbf{\Theta}} = \tilde{\mathbf{S}}_{\Phi}, \tag{3.43}$$

$$\mathbf{C}\tilde{\mathbf{\Phi}} + \mathbf{D}\tilde{\mathbf{\Theta}} = \tilde{\mathbf{S}}_{\Phi}, \tag{3.44}$$

where the matrices $\mathbf{A}$,$\mathbf{B}$,$\mathbf{C}$ and $\mathbf{D}$ are presented in appendix A. The time and frequency superscripts have been dropped here for simplicity. If equation (3.44) is now multiplied by $\mathbf{D}^{-1}$, the subgrid scale solution becomes

$$\tilde{\mathbf{\Theta}} = -\mathbf{D}^{-1}\mathbf{C}\tilde{\mathbf{\Phi}} + \mathbf{D}^{-1}\tilde{\mathbf{S}}_{\Theta}. \tag{3.45}$$

Substituting this into (3.43) an expression for the coarse solution is formed:

$$(\mathbf{A} - \mathbf{B}\mathbf{D}^{-1}\mathbf{C})\tilde{\mathbf{\Phi}} = -\mathbf{B}\mathbf{D}^{-1}\tilde{\mathbf{S}}_{\Theta} + \tilde{\mathbf{S}}_{\Phi}. \tag{3.46}$$

The continuous coarse solution $\tilde{\mathbf{\Phi}}$ is solved using (3.46) and then (3.45) is utilised to calculate the discontinuous fine solution $\tilde{\mathbf{\Theta}}$. Finally the two components are added to get the full discontinuous solution for the action density $\mathbf{N}$ (3.33).

The rationale for using the sub-grid scale discretisation is to get the accuracy and stability of discontinuous methods, without the cost of having to solve for the full set of unknowns. Equation (3.46) has continuous degrees of freedom but when combined with equation (3.45) produces a discontinuous solution.

The main added cost now is the inversion of $\mathbf{D}$. However, $\mathbf{D}$ acts merely as a stabilisation to the system and can be approximated to make its inversion efficient. The first approximation was the removal of the incoming boundary conditions in $\mathbf{D}$ (equation 3.41). This means that in the fine discontinuous system, the sub-grid

variables are only coupled within each element. Thus, $\mathbf{D}$ becomes an element-block matrix coupling all the angular components on each element, and can be inverted on an element by element basis.

The angular sub-matrices of $\mathbf{D}$, $\mathbf{D}_{i,j}$ (see appendix A) contain the spatial integrals of the angular matrices (presented in section 3.5) for each node combination (i, j) of a spatial element. Thus, each sub-matrix $\mathbf{D}_{i,j}$ is sparse (for a $P0$ angular discretisation the only non-diagonal matrix is $\mathbf{H}_\theta$). The sparsity of $\mathbf{D}$ on each element is then dependent on the coupling of its nodal basis functions, with higher order approximations producing less sparse matrices. In general, however, inverting it for each element is a $\mathcal{O}(K^3)$ operation where K is the number of angles.

Fortunately as this is merely a stabilisation term it can be further simplified. As showed by [16] and [25] for the Boltzmann transport equation, simply diagonalising $\mathbf{D}_{i,j}$, i.e. decoupling the angles on each node of an element, produces a conservative and stable system. This is the case even in high scattering problems where $\mathbf{D}_{i,j}$ is dense and the angles are coupled tightly. This makes the cost of inverting $\mathbf{D}$ an $\mathcal{O}(K)$ operation. Initial results showed this is is also possible for the action balance equation, however, this is not further explored here and in the next sections $\mathbf{D}$ is calculated and inverted with the angular coupling intact.

The discrete system (3.43) is assembled for each frequency group, non-linear iteration step and time-propagation step and solved with the use of PETSc [6], which provides a wide range of pre-conditioners and solvers. In the examples that follow a GMRES iterative solver is used with an SOR pre-conditioner. The assembled system is then of size: (number of (continuous) nodes $\times$ number of angles)^2, for each frequency group.

The discretisation presented is linear and formed on arbitrary spatial elements. All the results presented in the next chapters are restricted to a $P1$ spatial discretisation (linear elements). That means that the spatial accuracy is 2^{nd} order $(p + 1)$.

According to Godunov's theorem any linear monotonicity-preserving scheme can be at most first-order accurate (see [27]). Thus, the proposed scheme leads to non- monotonic behaviour. In places of high discontinuities where the problem is under-resolved local oscillations can be produced resulting in negative values for the solution variables.

Both the non-linear limiter (see section 3.2) and the calculation of the source terms, however, depend on the sign of the action density and leaving these negative values

in the solution is unstable. Thus, after each solve, the negative values are removed. To ensure the scheme remains conservative, the action density is then rescaled to account for the removal of these values.

Chapter

FOUR

Validation

4.1 Introduction

To fully validate the proposed numerical scheme, each term of the equation should be tested individually. Here, a set of standardised tests are implemented, which isolate the various physical processes and are typically used for the validation of spectral wave models [13, 43, 70, 76, 59, 96].

In these simulations the adiabatic (linear) part of the system is tested by comparing the results with analytical solutions derived from the linear wave theory approximation. The (non-linear) source terms are then tested by comparing the results with field measurements and experiments. Here the results will also be compared to those obtained with SWAN (version 41.10 [83]) with identical physical setups, given that it is one of the most widely used and validated coastal spectral wave models.

The scheme presented in section 3 is formed on arbitrary spatial and angular expansions, which means that any type of basis functions can be used to formulate the system. However, in this chapter the simulations are restricted to a $P1$ spatial discretisation (linear elements) and a $P0$ angular discretisation (piece-wise constant elements).

In the next sections first the numerical diffusion in geographic space is investi-

gated. This is followed by the validation of the linear system, i.e. advection in geographic and spectral space, with depth- and current- induced shoaling and refraction. Then the implementation of wind-input, four-wave interactions and white-capping is tested, by studying the evolution of the spectrum in a fetch-limited growth test case. Finally the shallow water non-linear terms are tested with a three-wave interaction test case and a wave-breaking test-case.

The fetch-limited growth test case is run as a time dependent simulation without non-linear iterations (the non-linear system evolves with the time-marching). The last two test cases, however, are run as stationary problems which require a set of stopping criteria for the non-linear iterations. Running SWAN with the default break-off criteria (see section 3.2 and [81]), led to $\approx$ 15–60 iterations, starting from a zero initial condition. It was observed that the two codes with the same setups converged at approximately the same rates. However, given that the convergence behaviour of the non-linear iterations is beyond the scope of this work, a fixed number of 100 iterations was used for both codes.

4.2 Numerical diffusion

To test the level of numerical diffusion present in the spatial discretisation of Fluidity-SW, the test case of Booij et al. [13] is reproduced. A harmonic, long-crested wave in deep water ($d = 10\,\text{km}$) enters at an angle of 45° through a small gap ($150\sqrt{2}$ m) in the lower left corner of a 10 km $\times$ 10 km domain. The wave height is 1 m at the boundary and the frequency 0.1 Hz. This is represented by a Gaussian-shaped spectrum in frequency, with a peak frequency of 0.1 Hz and a standard deviation of 0.01 Hz. The frequency mesh has 100 elements logarithmically distributed from 0.01–0.25 Hz (resulting in $\Delta\sigma/\sigma = 0.0327$). The directional spectrum is represented by a $\cos^{500}(\theta)$ distribution (this results in a directional width of $\sigma_\theta = 2.5°$, where σ_θ is the standard deviation of the directional distribution [50]) and an angular mesh of 720 elements (resulting in $\Delta\theta = 0.5°$). Given that the wave propagates in deep water and there are no currents present, the velocities in spectral space (c_θ, c_σ) are both zero. The high number of elements in angle and frequency are thus only necessary to properly represent the respective distributions.

The stationary results for a spatial mesh with an element-edge length of $\Delta x \approx 100\,\text{m}$ (26,559 elements) are presented in figure 4.1a and the results from SWAN on the

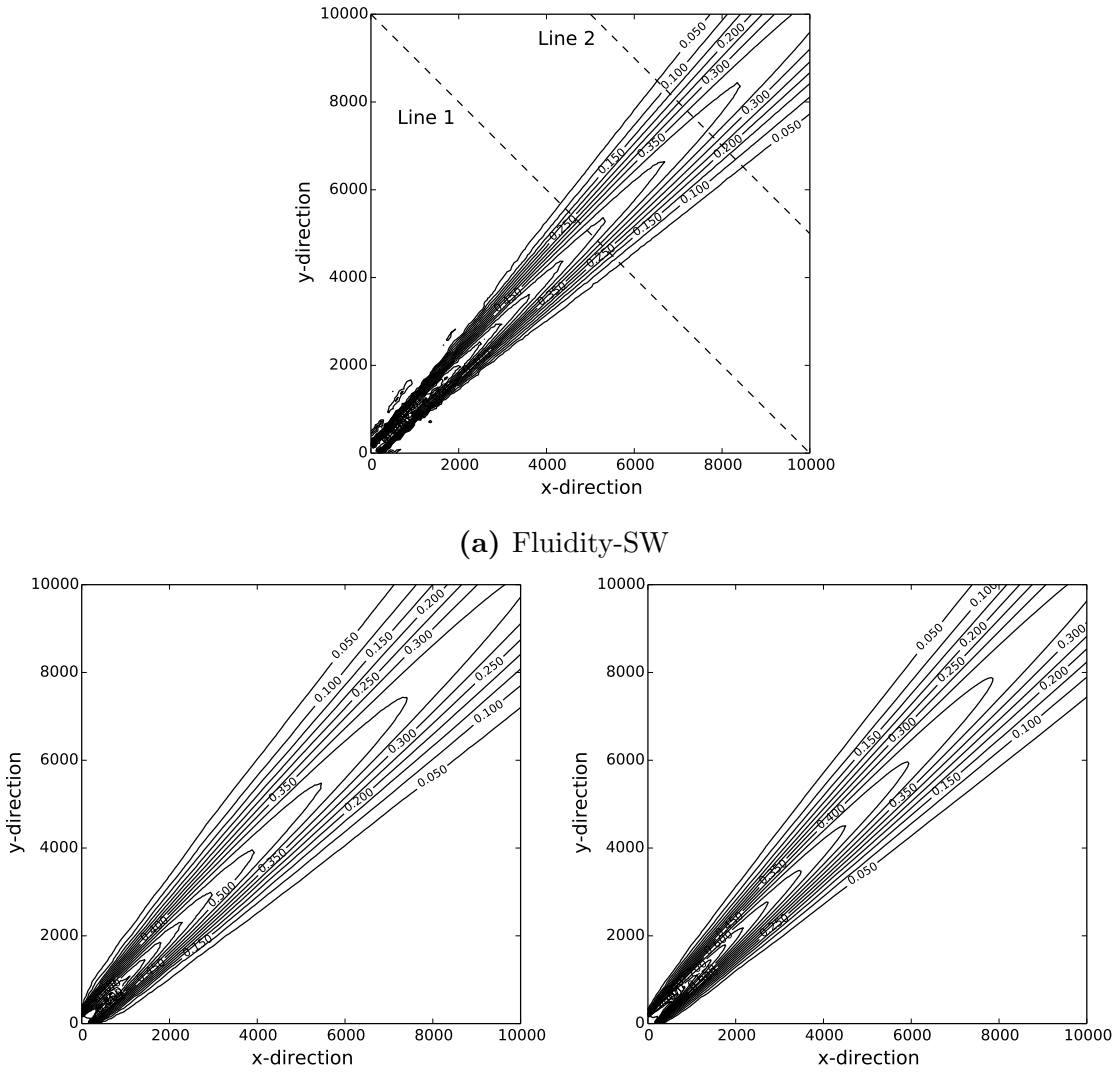
same mesh in figure 4.1b. SWAN is first-order accurate in geographic space (higher order approximations are only available in the structured version of SWAN) and is thus expected to be more diffusive compared to the second-order $P1$ sub-grid scale method. However, the first-order scheme of SWAN is monotone, producing smooth results throughout the domain, whereas the non-monotone nature of the proposed scheme produces small oscillations in the lower left corner of the domain, where strong gradients in the solution field exist. The effects of this are further explored in a realistic test case in sections 6.2 and 6.4 in the context of mesh resolution and mesh adaptivity.

To quantify the advantage of using higher order schemes in space in terms of levels of numerical diffusion, the results for SWAN on a finer mesh with an element-edge length of $\Delta x \approx 50\,\mathrm{m}$ (106,236 elements) are presented in figure 4.1c. Increasing the spatial resolution has a visible effect for SWAN, but the spreading of the wave is still wider compared to Fluidity-SW. This is more clearly depicted in the line plots presented in figure 4.2, for the diagonal lines in figure 4.1a. SWAN on the same mesh produces a wider spread and smaller peaks, as its results are diffused over the path of propagation. Increasing the number of elements improves the results and pushes them more towards Fluidity-SW, but even with four times as many elements, they are still clearly more diffusive.

Similar findings have been published by Rogers et al. [75], Hsu et al. [43] and Qi et al. [70] who showed that the second-order (SORDUP) and third-order (S&L) spatial discretisation of SWAN (available only for structured grids) are significantly less diffusive. In fact these schemes were implemented to improve the results of SWAN in larger-scale simulations [75]. When simulating wave propagation over larger scales, where the effects of diffusion become more important, higher-order schemes provide a significant advantage.

4.3 Depth-induced shoaling and refraction

A plane beach front is considered, represented by a $4\,\mathrm{km} \times 4\,\mathrm{km}$ domain, with a bathymetric slope of $1 : 200$. A long wave enters from the deep eastern boundary with $d = 20\,\mathrm{m}$ propagating towards the shallow western boundary with $d = 0.05\,\mathrm{m}$ (figure 4.3a). Two different cases are considered. In the first the wave enters perpendicular to the boundary, at an angle of 180° measured counter-clockwise from

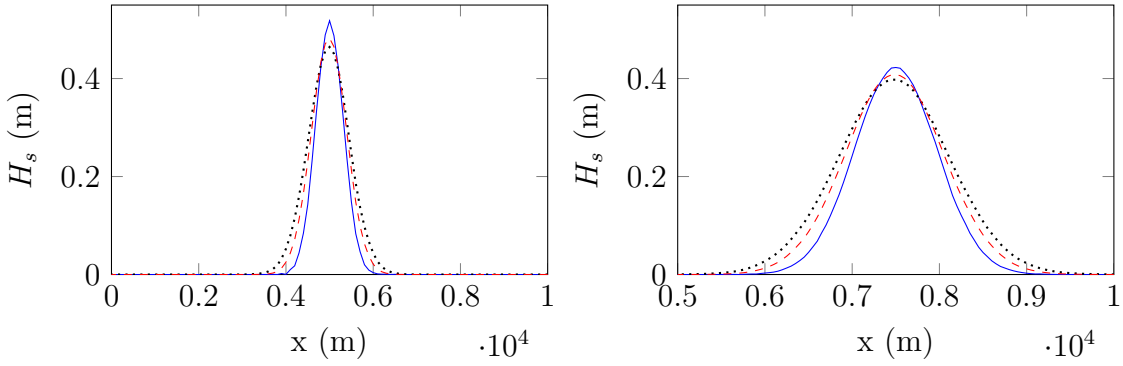


(a) Fluidity-SW

(b) SWAN

(c) SWAN-fine

Figure 4.1: Contour plots of significant wave heights for the numerical diffusion test case. Line 1 and line 2 refer to transects across which the significant wave heights are displayed in figure 4.2.



(a) Line 1 **(b)** Line 2

Figure 4.2: Line plots of significant wave heights for the numerical diffusion test case, for the two lines shown in figure 4.1a.
Fluidity-SW: ——, SWAN: ·····, SWAN-fine: - - -.

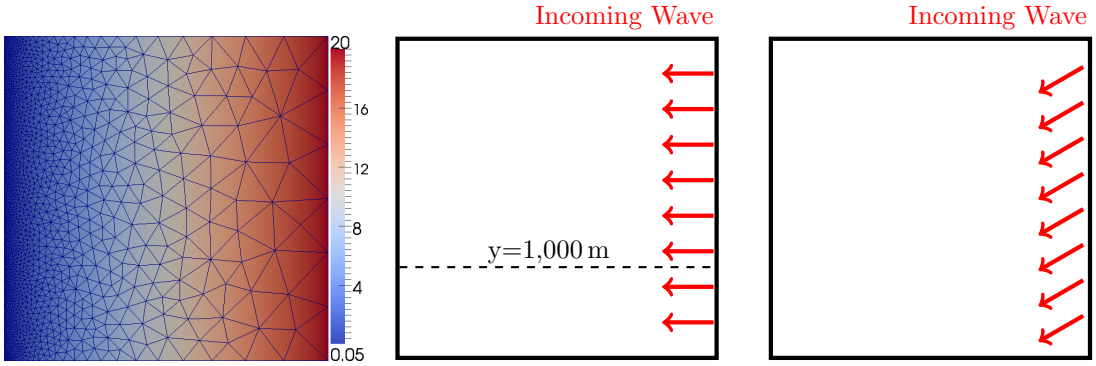
the positive x-axis, (figure 4.3b), while in the second the wave enters at an angle of 210° (figure 4.3c).

For this set-up, as the wave encounters shallower waters, it slows down, causing its wavelength to decrease and, thus, its wave height to increase. This is referred to as shoaling (In the general case, the group velocity initially increases slightly before decreasing [41]). If different parts of the wave-train travel with different speeds, as they will in different water depths, then the wave will also turn. This is referred to as refraction.

To test shoaling and refraction, a monochromatic wave is considered with a wave height of 1 m, a frequency of 0.1 Hz, and a $\cos^{500}(\theta)$ directional distribution. Given that there are no currents present and the bottom level is stationary, there is no frequency shifting. Thus only one frequency group is used to represent the monochromatic wave. All the source terms are deactivated. The significant wave height and the mean direction can be compared to,

$$\frac{H^2}{H_i^2} = \frac{c_{gi}\cos(\theta_i)}{c_g\cos(\theta)}, \qquad (4.1) \qquad\qquad \frac{\sin(\theta)}{\sin(\theta_i)} = \frac{c}{c_i}, \qquad (4.2)$$

where H is the wave height, θ is the direction, c_g and c the group and phase velocity respectively, while i denotes the incoming value. Equation (4.1) is derived from the linear wave theory, while equation (4.2) is Snell's law.

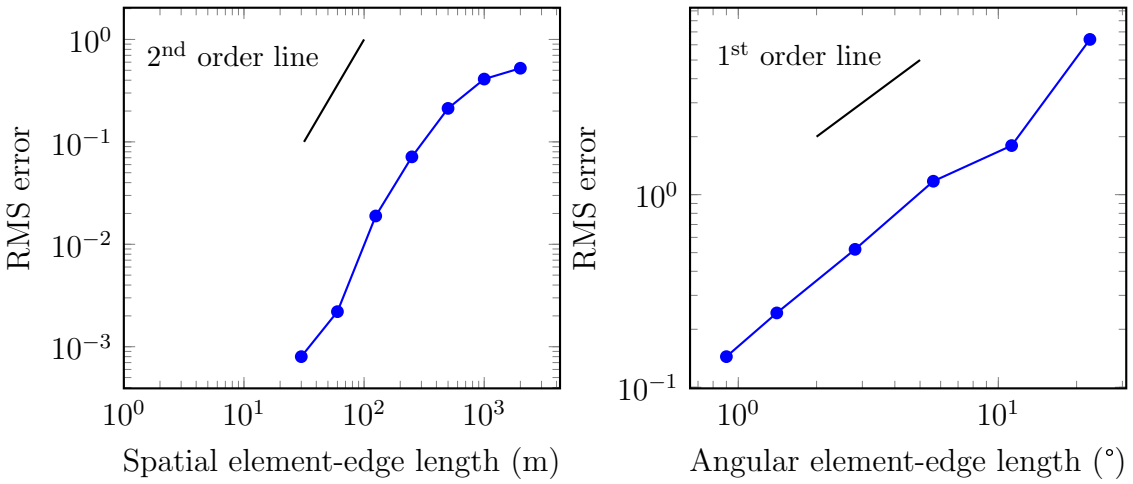


(a) Spatial mesh and depth **(b)** Test case I **(c)** Test case II

Figure 4.3: Depth induced shoaling and refraction. The depth is linearly decreasing from 20 m in the eastern boundary to 0.05 m in the western boundary. This is resolved with a non-uniform mesh with smaller edge lengths in the shallow water region. Two test cases are considered. In test case I the incoming wave enters at an angle of 180°, while in test case II at an angle of 210°.

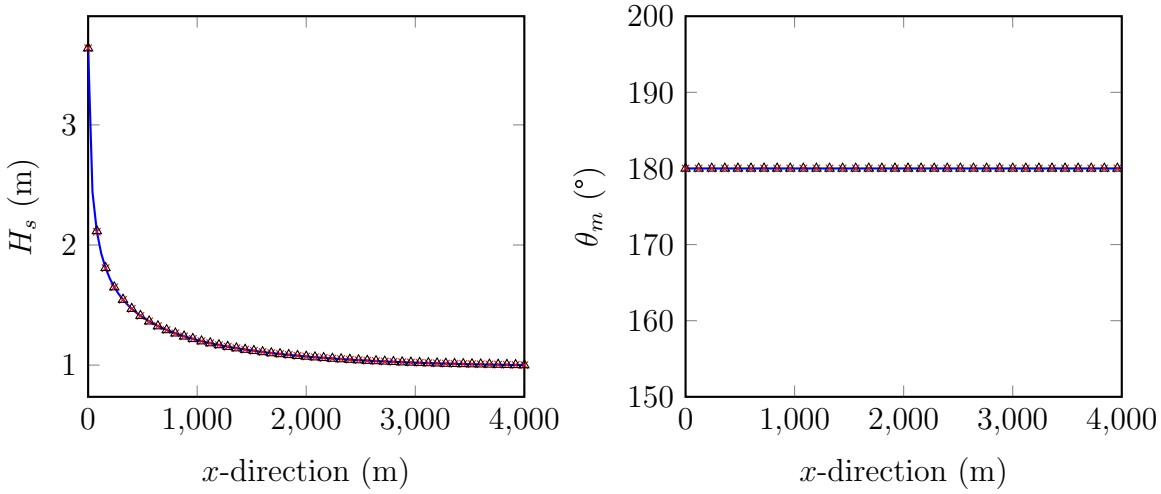
First, two convergence tests are performed for the spatial and angular dimension respectively. These are presented in figure 4.4. For the spatial convergence, test case I is used (see figure 4.3b). Using 100 elements for the angular dimension ($\Delta\theta = 3.6°$), for each simulation the spatial element-edge length is halved and the discrete root-mean-square (RMS) error of the significant wave height plotted. This is calculated by comparing the results with equation (4.1), along the y=1,000 m line. For the angular convergence, test case II is used (see figure 4.3c). Using a spatial element-edge lenth of $\Delta x \approx 30$ m (47764 elements), for each simulation the angular element-edge length is halved and the discrete RMS error of the mean direction plotted. This is calculated by comparing the results to equation (4.2), along the y=1,000 m line. For both the spatial and angular converge tests, a $(p+1)$ convergence rate is achieved, i.e. 2^{nd} and 1^{st} order respectively.

To compare the results against the analytical solutions and the results obtained with SWAN, a high fidelity simulation is now run. To account for the spatial variation of the wavelength, the spatial mesh has a variable element size, starting from an element-edge length of $\Delta x \approx 600$ m and going down to 20 m, resulting in 3,594 elements (figure 4.3a). At the same time, given that refraction is a dominant process, 400 elements are used to represent the angular dimension of the wave (resulting in $\Delta\theta = 0.9°$). The stationary results plotted along the $y = 1{,}000$ m line (dashed line of figure 4.3b) are presented in figure 4.5 for test case I and figure 4.6



(a) Spatial convergence for test case I **(b)** Angular convergence for test case II

Figure 4.4: Spatial and angular convergence for test case I and test case II of the depth-shoaling and refraction test case respectively. For the spatial convergence, as the spatial element-edge length of test case I is reduced, the RMS error is calculated by comparing the significant wave height to the results of equation (4.1), along the y=1,000 m line. For the angular convergence, as the angular element-edge length of test case II is reduced, the RMS error is calculated by comparing the mean direction to the results of equation (4.2), along the y=1,000 m line.



(a) Significant wave height

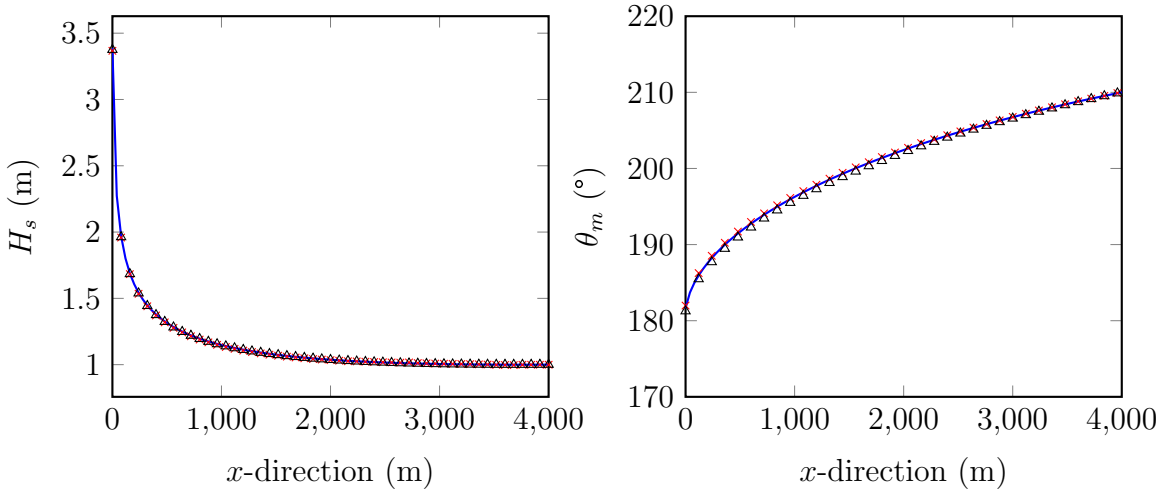
(b) Mean direction

Figure 4.5: Validation for depth induced shoaling and refraction for a wave entering at an angle of 180° (test case I), along the line shown in figure 4.3b. Analytical solutions: ——, Fluidity-SW: ×, SWAN: ▵.

for test case II.

For both test cases as the wave enters shallower waters the significant wave height increases (figures 4.5a, 4.6a). Most of this increase happens in the last few metres when the depth approaches zero, outlining the importance of variable spatial resolutions in coastal applications. If the bathymetric value is allowed to reach a zero value, then the group speed becomes zero and the wave height infinite, which is why the minimum depth needs to always be above zero (here it is set to 0.05 m). This is simply a consequence of the linear wave approximation (linear theory breaks down well before the group speed reaches zero), as in reality the wave energy is dissipated by non-linear processes such as wave breaking. Comparing to the analytical solutions, both codes give near identical results and reproduce shoaling successfully.

Depth induced refraction is caused by phase speed variations due to depth variations along the crest of a wave. The rate of refraction is controlled by the bathymetric gradients, however, another consequence of the linear theory is that when the depth and the phase velocity become zero, the mean direction becomes perpendicular to the shore, regardless of the incident mean direction in deep water (this is derived by setting the phase speed to zero in equation (4.2)). Thus, for test case I where the wave is perpendicular to the bathymetric contours, the mean direction remains constant (figure 4.5b). For test case II the wave is at an angle to the bathymetric



(a) Significant wave height

(b) Mean direction

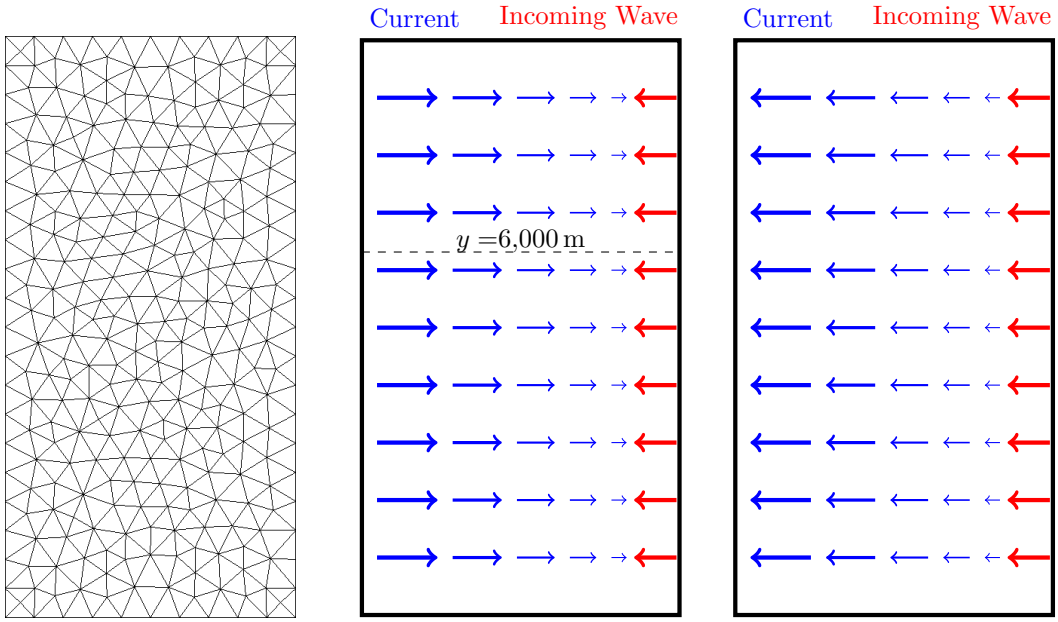
Figure 4.6: Validation for depth induced shoaling and refraction for a wave entering at an angle of 210° (test case II), along the line shown in figure 4.3b. Analytical solutions: ——, Fluidity-SW: ×, SWAN: ▵.

contours and thus different parts of the train have different phase speeds. This causes the wave to refract from 210° to almost 180° (figure 4.6b). Both codes accurately reproduce the results from linear theory with SWAN slightly under-predicting the mean direction.

4.4 Current-induced shoaling and refraction

To validate the implementation of wave-current interactions, a deep-water ($d = 10\,\text{km}$) scenario is considered in which a long-crested, harmonic wave propagates in the presence of an ambient current. The domain is $4\,\text{km} \times 10\,\text{km}$ with an element-edge length of $\Delta x \approx 400\,\text{m}$, resulting in 648 elements (figure 4.7a). The wave has a height of 1 m and is represented by a Gaussian-shaped frequency distribution with a peak frequency of 0.1 Hz and 0.01 Hz standard deviation and a $\cos^{500}(\theta)$ directional distribution.

Four different scenarios are considered. The first two test current-induced shoaling, with the waves in test case I opposing and in test case II following the current direction. A wave is prescribed in the eastern boundary with a significant wave height of 1 m and an incident mean direction of 180°, on top of a spatially variable



(a) Spatial mesh **(b)** Test case I **(c)** Test case II

Figure 4.7: Current induced shoaling. Two test cases are considered. In test case I waves are opposing and in test case II following the current direction. The V_x current-component is decreasing linearly in the $x-$direction from 2 m/s to 0 m/s.

current, with a speed V_x which increases from 0 to 2 m/s in the down-wave direction (figures 4.7b and 4.7c). The vector form of the current for test cases I and II is,

$$\mathbf{V}_{\mathrm{I}} = \begin{bmatrix} 2-(1/2000)x \\ 0 \end{bmatrix}, \qquad (4.3) \qquad \mathbf{V}_{\mathrm{II}} = \begin{bmatrix} -2+(1/2000)x \\ 0 \end{bmatrix}. \qquad (4.4)$$

The ambient current changes the group velocity of the wave causing it to slow down, or speed up for test cases I and II respectively. At the same time, the spatial variation of the current results in frequency shifting, i.e. the velocity in σ space, c_σ, is non-zero. This causes energy to move up or down the frequency groups, changing the wave field's mean relative frequency and significant wave height. Given that the wave vectors and current vectors are always parallel, the velocity in θ -space, c_θ is zero and there is no refraction.

To represent the narrow angular distribution of the incoming waves, 100 angular element are used resulting in $\Delta\theta = 3.6°$. To accurately represent frequency shifting a higher number of 300 frequency elements are used, logarithmically distributed

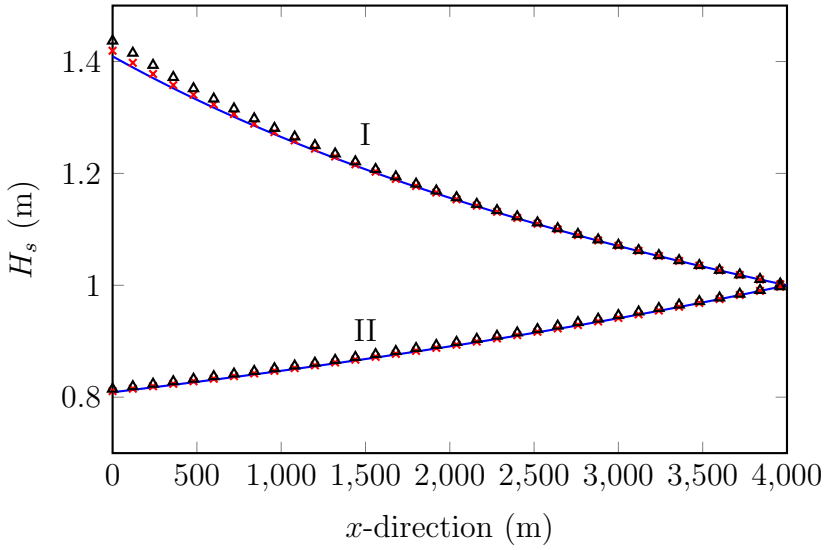


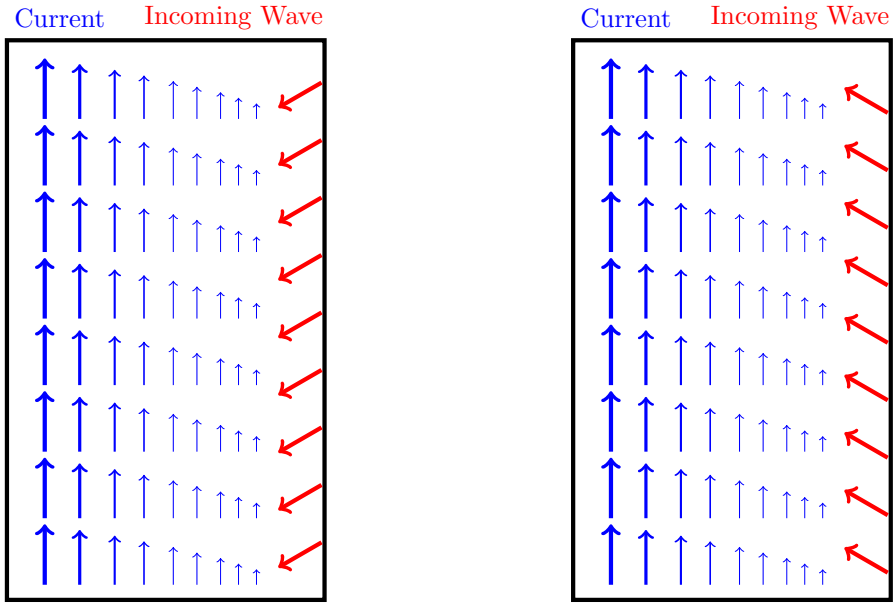
Figure 4.8: Validation for current induced shoaling, along the line shown in figure 4.7b. In test case I waves are opposing and in test case II following the current direction.
Analytical solutions: ——, Fluidity-SW: ×, SWAN: ▵.

between $0.05 - 0.25$ Hz, resulting in $\Delta\sigma/\sigma = 0.0054$. All the source terms are deactivated. The analytical solution for the significant wave height comes directly from the fact that the absolute frequency remains constant ($\omega = \sigma + \mathbf{k} \cdot \mathbf{V} = ct$), since the absolute frequency only changes with temporal variations of depth and currents (see [57]). The equations read [63, 57],

$$\frac{H^2}{H_i^2} = \frac{c_i^2}{c(c+2V)}, \qquad (4.5) \qquad \frac{c}{c_i} = \frac{1}{2} + \frac{1}{2}\left(1 + 4\frac{V}{c_i}\right)^{1/2}, \qquad (4.6)$$

where H is the wave height, V the current speed, c the phase speed and i denotes the incoming value.

The stationary results for the significant wave height plotted along the $y = 6{,}000\,\mathrm{m}$ line (dashed line of figure 4.7b) for both test cases, are presented in figure 4.8. As the wave propagates against the current the wave height increases, and when the wave follows the current the wave height decreases, for test cases I and II respectively. It is worth noting that the effect on the wave height is more prominent in the opposing rather than the following case. In fact in equation (4.5) there is a theoretical limit at $c = -2V$ where the wave height becomes infinite. In practice various non-linear



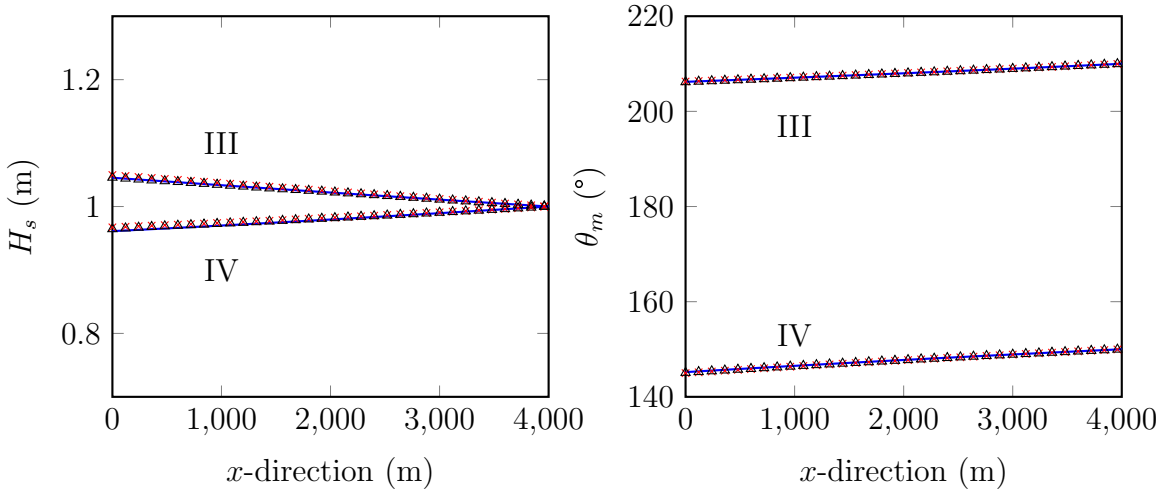
(a) Test case III **(b)** Test case IV

Figure 4.9: Current induced shoaling and refraction on a shearing current. Two test cases are considered: The incoming wave is at an angle of 210° for test case III and 150° for test case IV. The V_y current-component is decreasing linearly in the $x-$direction from 2 m/s to 0 m/s.

processes take place before that point, including wave breaking wave reflection etc., and the linear approximation becomes invalid. Both codes accurately reproduced the results from equation (4.5), with SWAN slightly overestimating the significant wave heights. This is due to the lower accuracy of the spatial discretisation of SWAN and thus decreasing the element size results in a better match.

The final two cases test current induced refraction. For this, a shearing-current test case is reproduced, where the current is flipped by 90° and the wave is flipped by 30° and −30° for case III and IV respectively, compared to test case I. Thus the wave has an incident direction of 210° for test case III and 150° for test case IV, propagating on top of a spatially variable current, with a speed V_y which decreases from 2 m/s to 0 m/s in the x-direction (figure 4.9). The vector form of the current for test cases III and IV is,

$$\mathbf{V}_{\mathrm{III,IV}} = \begin{bmatrix} 0 \\ 2 - (1/2000)x \end{bmatrix}. \tag{4.7}$$



(a) Significant wave height **(b)** Mean direction

Figure 4.10: Validation for current induced shoaling and refraction, for an incoming wave at an angle of 210°, for test case III, and 150°, for test case IV, on top of a shearing current. The results are plotted along the line shown in figure 4.7b.
Analytical solutions: ——, Fluidity-SW: ×, SWAN: ▵.

Part of the current will slow down or speed up the wave and consequently push energy to higher or lower frequencies for III and IV respectively. This effect however is smaller from the previous test cases, as c_σ is smaller. At the same time, due to the relative angle between the wave and the current, part of the wave energy will be swept away along the direction of the current, i.e. c_θ is now non-zero and current induced refraction takes place.

Thus, for these test cases a high number of 720 angular elements is used, resulting in $\Delta\theta = 0.5°$. For the frequency dimension a smaller number of 40 frequency elements are used, logarithmically distributed between $0.05 - 0.25$ Hz, resulting in $\Delta\sigma/\sigma = 0.0421$. Again all the source terms are deactivated. The significant wave height and mean direction can be compared to the analytical solutions derived by Longuet-Higgins and Stewart [53],

$$\sin\theta = \frac{\sin\theta_i}{\left(1 - \frac{V}{c_i}\sin\theta_i\right)^2}, \qquad (4.8)$$

$$H = H_i \left(\frac{\sin(2\theta_i)}{\sin(2\theta)}\right)^{1/2}, \qquad (4.9)$$

where H is the wave height, V the current speed, c the phase speed, θ the wave

direction and i denotes the incoming value.

The stationary results for the significant wave height and mean direction for both test cases, plotted along the y =6,000 m line (dashed line of figure 4.7b) are presented in figure 4.10. In test case III, as part of the wave propagates against the current its wave height grows while in test case IV, propagating following the current causes the wave height to drop. In both test cases, the waves are pushed towards the current direction causing their mean direction to change. Both codes accurately reproduced the analytical solutions.

4.5 Fetch-limited growth

Wave growth (in deep water) is the result of the balance between wave generation from wind input, energy dissipation from white-capping and energy redistribution from the non-linear interactions. As the wind blows over an area, most of the energy is transferred to the high- and mid-range frequencies. Non-linear wave-wave interactions shift most of that energy to lower frequencies, with a smaller amount moving towards the high frequency part of the spectrum. White-capping then removes most of the energy in the mid- and high- frequency range, resulting in a spectrum that gradually becomes narrower and moves towards lower frequencies [41]. In the end, these processes come to an equilibrium and the spectrum is considered to be fully developed.

To test the implementation of wind input, white-capping and four-wave interactions the fetch-limited growth test case is adopted. A uniform, constant wind blows over a large area, perpendicular to a straight shore in the offshore direction ($\theta_{\text{wind}} = 0°$). Starting from a zero initial sea state, the ability of the model to calculate the evolution of the spectrum in deep water ($d = 10\,\text{km}$) is studied, by examining the change of the resulting wave field with distance.

Two different simulations on two different meshes are set up to accurately capture the variable resolutions needed for small and large fetches. The first domain is 10 km $\times$ 10 km with a constant element-edge length of $\Delta x \approx 100\,\text{m}$, resulting in 26,428 elements. This simulates the wave growth for a small fetch. The results at the eastern boundary, i.e. where the waves exit the domain, are then used as a boundary condition for the large fetch test case. This is simulated on a 9,000 km $\times$ 2,000 km domain, in the $x-$ and $y-$ direction respectively, with a variable element-

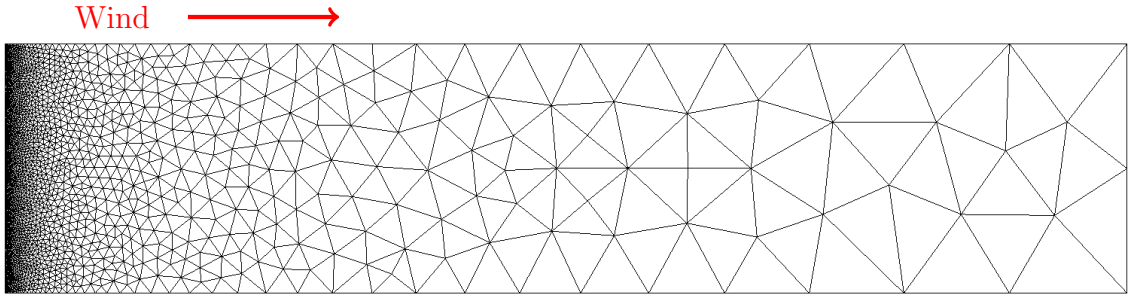


Figure 4.11: Spatial mesh for the fetch limited growth test case. The wind is blowing in the positive $x-$ direction ($\theta_{\text{wind}} = 0°$).

edge length from $\Delta x \approx 10\,\text{km}$ to 1,000 km, resulting in 5,096 elements (figure 4.11). The split of the fetch-limited growth test case into two meshes, small and large, is arbitrary and done only for computational efficiency, as the variable edge lengths used in the two simulations range from 100 m to 1,000,000 m, i.e. four orders of magnitude.

The wind speed in the $x-$direction is $U_{10} = 20\,\text{m}\,\text{s}^{-1}$. Both simulations are set-up with 64 angular elements, resulting in $\Delta\theta = 5.625°$ and 33 frequency elements logarithmically distributed from 0.05 Hz to 1.0557 Hz, resulting in $\Delta\sigma/\sigma = 0.1$. The activated source terms are wind-input, white-capping and four-wave interactions, with the default parameters presented in section 2.4. Both runs are non-stationary starting from a zero initial condition. The small-fetch is run with a time step of $\Delta t = 360\,\text{s}$ for 86,400 s (1 day) and the large-fetch with a time step of $\Delta t = 360\,\text{s}$ for 691,200 s (8 days).

To compare the results against measurements and analytic solutions the non-dimensional energy, non-dimensional peak frequency and non-dimensional fetch are calculated as

$$E^* = \frac{g^2 E_{tot}}{U_*^4}, \quad (4.10) \qquad {f_p}^* = \frac{f_p U_*}{g}, \quad (4.11) \qquad x^* = \frac{gx}{U_*^2}, \quad (4.12)$$

where $g = 9.81\,(\text{m}\,\text{s}^{-2}$ is the acceleration due to gravity, E_{tot} (m^2) is the total variance, i.e. the integral of the variance density spectrum over frequencies and directions, f_p (Hz) is the peak frequency, x (m) is the distance in the $x-$ direction and U_* ($\text{m}\,\text{s}^{-1}$) is the friction velocity calculated with the expression of Wu (equations (2.32,2.33)).

The results for both codes on the same meshes are presented in figures 4.12 and 4.13

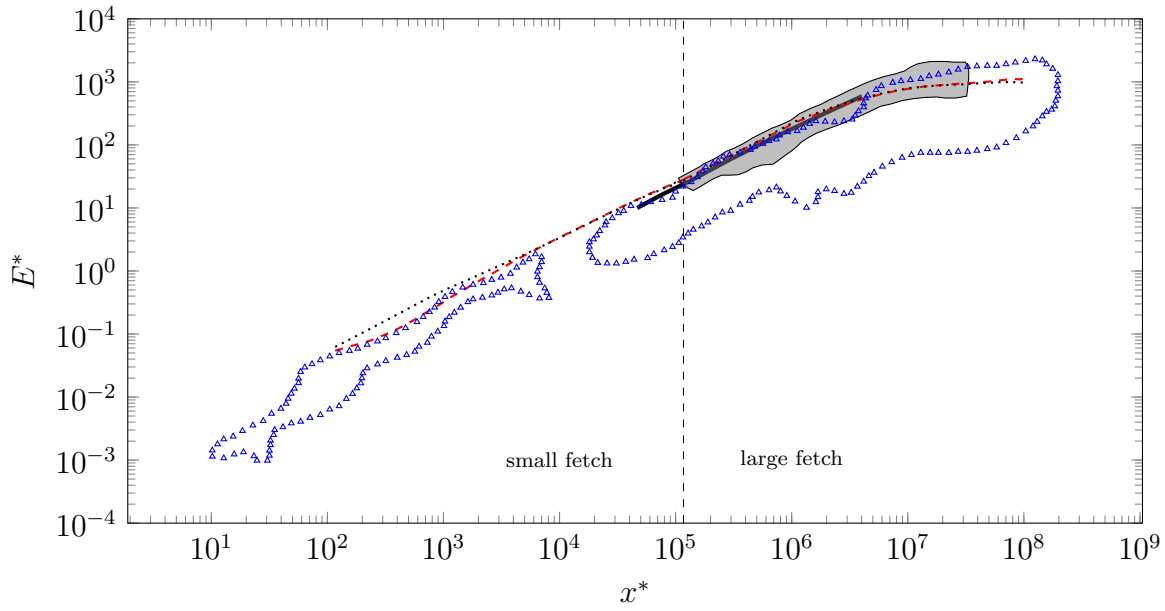


Figure 4.12: Validation for non-dimensional energy E^* against non-dimensional fetch x^*, for the fetch limited growth test case.
Wilson: ▵, Kahma and Calkoen: ——, SWAMP group: ▭, Fluidity-SW: - - -, SWAN: ·····.

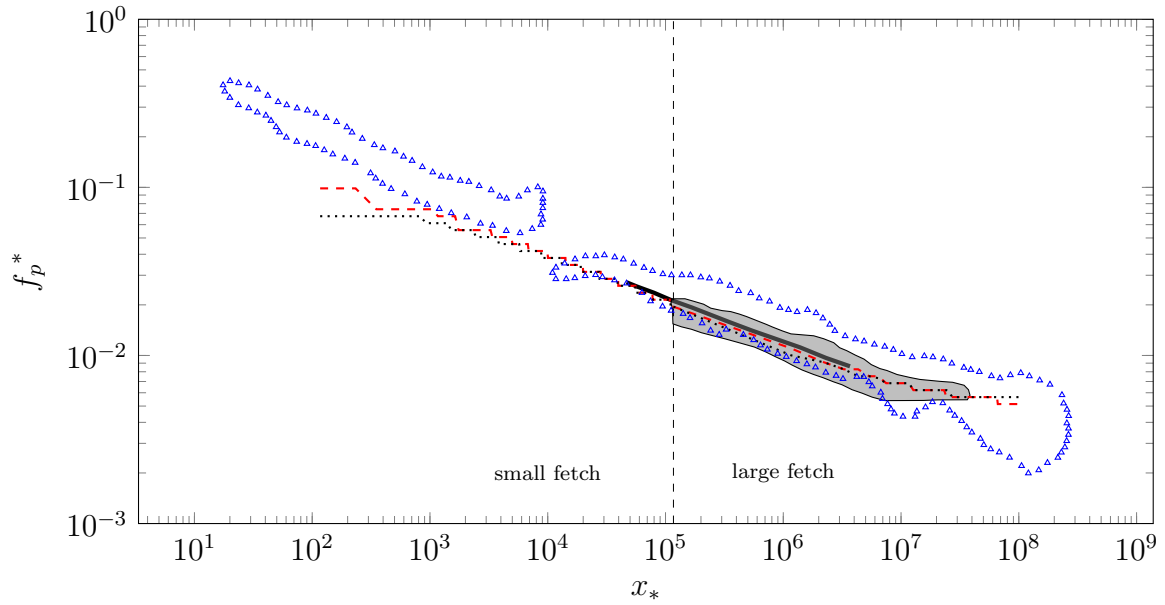


Figure 4.13: Validation for non-dimensional peak frequency $f_p{}^*$ against non-dimensional fetch x^*, for the fetch-limited growth test case.
Wilson: ▵, Kahma and Calkoen: ——, SWAMP group: ▭, Fluidity-SW: - - -, SWAN: ·····.

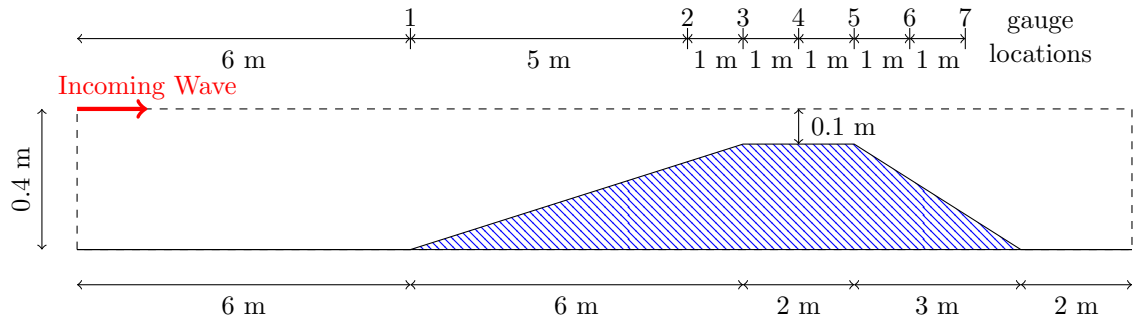


Figure 4.14: Set-up of the flume experiment by Beji and Battjes [10] for shallow water three-wave interactions, with the location of the gauges used for the output of the spectrum in figure 4.16.

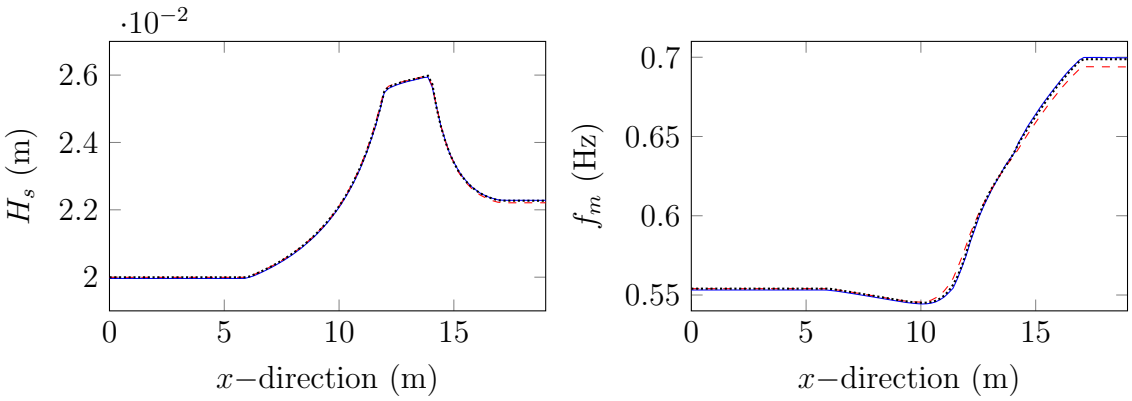
for the non-dimensional energy and non-dimensional peak frequency respectively, against the envelope of observations of Wilson [94], the analytical expression from Kahma and Calkoen [47], and the envelope of model results from the SWAMP group [80].

Towards smaller fetches ($x^* < 3 \times 10^3$), SWAN overestimates the non-dimensional energy and underestimates the non-dimensional peak frequency. This is due to the lower accuracy of the spatial discretisation of SWAN. Decreasing the element size in the SWAN set-up results in a better match. Beyond that region both codes produce similar results, showing good agreement with the analytic solution from Kahma and Calkoen and falling in the middle of the envelope of results from the SWAMP group. Finally compared to the observations of Wilson, the models are in the top limit of the non-dimensional energy and bottom limit of the non-dimensional peak.

4.6 Shallow water non-linear interactions

In very shallow water, three-wave interactions become important. As mentioned in section 2.4.4, a simple approximation of these interactions in the surf-zone is the LTA which, when applied to a unimodal spectrum, transfers energy from the primary frequency peak to its superharmonic. This results in a secondary peak at twice the frequency [41].

To test the implementation of the LTA the flume experiment by Beji and Battjes [10] is reproduced, in which a long wave propagates over a submerged bar, without breaking. The flume set-up, presented in figure 4.14, is simulated with a 19 m ×



(a) Significant wave height

(b) Mean frequency

Figure 4.15: Validation for the three-wave interactions test case. The significant wave height is plotted along the $y = 9.5$ m line of the domain.
Fluidity-SW: ——, SWAN: - - -, SWAN-fine: ·····.

19 m domain. The incoming wave has a wave height of 0.02 m and is represented in the model with a JONSWAP spectrum (γ =3.3), with peak frequency 0.5 s and 32 frequency elements logarithmically distributed from 0.125 Hz to 2.4 Hz, resulting in $\Delta\sigma/\sigma = 0.1$. The mean direction of the wave is 0° and 100 angular elements are used, resulting in $\Delta\theta = 3.6°$, to model the $\cos^{500}(\theta)$ directional distribution. The test case is run as a stationary problem. The results of this simulation are not affected by wave-induced breaking [13] and thus only the three-wave interaction source term is activated.

Having no access to the original flume measurements, the results of the simulation are directly compared to SWAN, as Booij et al. [13] have already shown good agreement between SWAN and the measurements. The proportionality coefficient α_{EB} (see section 2.4.4) in the LTA is a tunable coefficient that requires some calibration. Without the data to calibrate against, just the implementation of the source term is considered here and only one proportionality coefficient is used equal to $\alpha_{\text{EB}} = 0.65$.

The domain is discretised with an edge length of $\Delta x \approx 0.5$ m, resulting in a spatial mesh with 3,778 elements. The results for both codes plotted along the $y = 9.5$ m line (middle line of the domain) are presented in figure 4.15. The significant wave height is very similar for both codes, but SWAN under-estimates the mean frequency close to the eastern boundary of the domain. Increasing the spatial resolution on the SWAN model, it was found that to produce the same results a $\Delta x \approx 0.125$ m (i.e. 4 times smaller) is required, resulting in a spatial mesh with 60,448 elements

(SWAN-fine in figure 4.15).

The evolution of the spectrum as the wave propagates over the submerged bar is presented in figure 4.16, where the variance density spectrum E_{var} (cm^2/Hz) is plotted for the various gauge locations in figure 4.14. The wave enters with a peak frequency of 0.5 Hz and as it propagates over shallower waters, develops a secondary peak at 1 Hz. The results of Fluidity-SW are practically identical with SWAN-fine validating the implementation of the LTA approximation in the action balance equation.

4.7 Depth-induced wave breaking

To test depth-induced wave breaking the flume experiment by Battjes and Janssen [8] is reproduced. A long wave propagates from deep to shallow water across a bar-trough profile which causes it to break. The flume set-up is presented in figure 4.17.

This is simulated with a 18.72 m $\times$ 18.72 m domain with the wave entering at the eastern boundary. The wave has a height of 0.2 m and is represented by a JONSWAP spectrum ($\gamma = 3.3$) with peak frequency 0.53 Hz. The frequency domain is discretised with 32 elements logarithmically distributed from 0.125 Hz to 2.4 Hz, resulting in $\Delta\sigma/\sigma = 0.1$. The angular domain is discretised with 100 elements, resulting in $\Delta\theta = 3.6°$, to represent the $\cos^{500}(\theta)$ directional distribution of the incoming wave, which enters at an angle of 0°. The test case is run as a stationary simulation.

To isolate the impact of breaking, first the three-wave interactions are not activated and the only source term used is depth-induced breaking with a constant breaking index of $\gamma = 0.73$ (see section 2.4.5). A relatively coarse mesh is constructed with an edge-length of $\Delta x \approx 0.8$ m, resulting in 1,648 elements. The results plotted along the $y = 9$ m line (middle line of the domain) are presented in figure 4.18.

Looking at the measurements, as the wave faces shallower waters ($0 < x < 5$) it starts to shoal with the significant wave height slightly increasing. Beyond that point ($5 < x < 10$) the significant wave height drops as the wave breaks abruptly, followed by a region ($10 < x < 15$) where breaking halts and the wave height remains constant. Finally in the last region ($x > 15$) the wave starts to slowly shoal again.

Comparing the two codes, SWAN is over-predicting the significant wave height

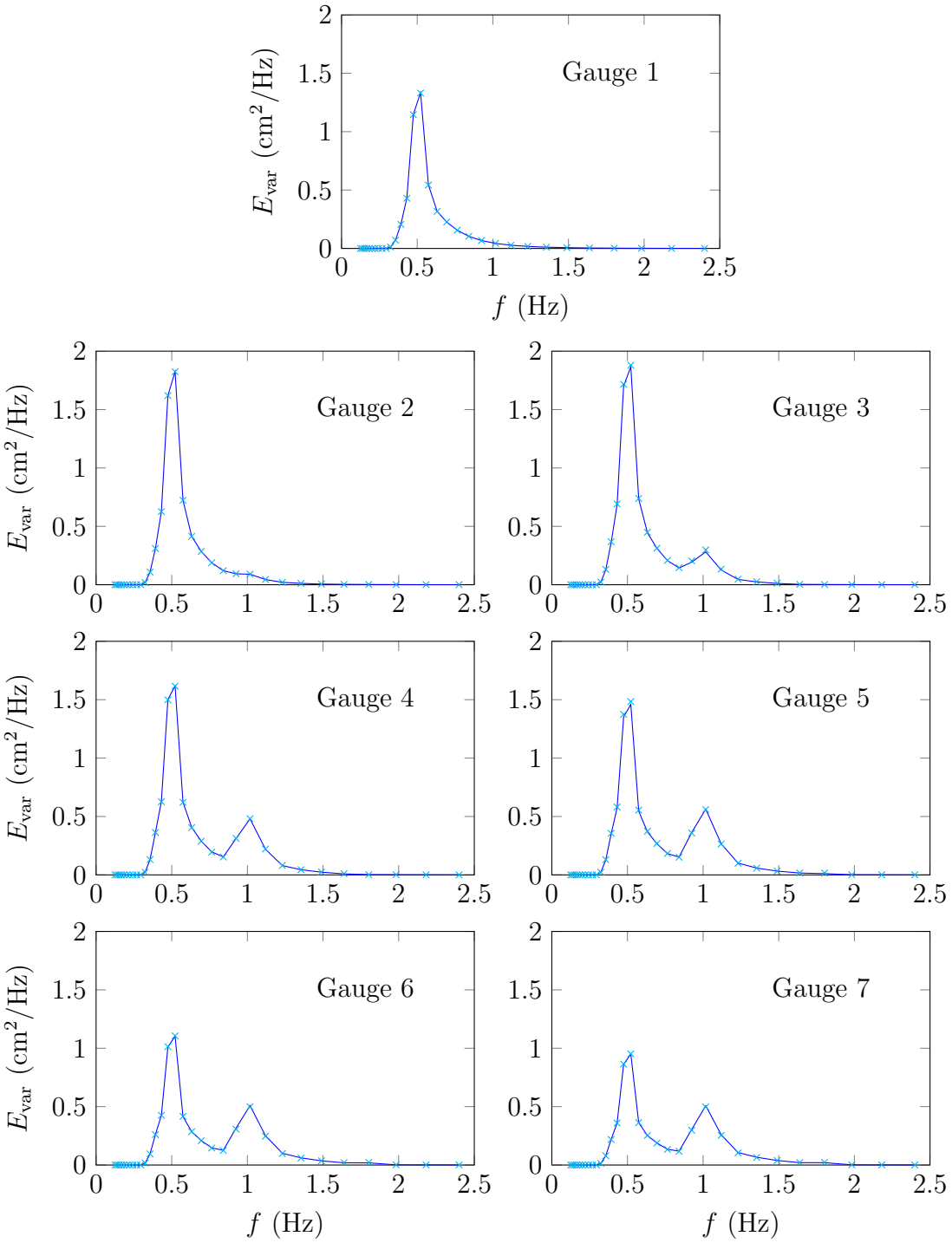


Figure 4.16: Validation for the three-wave interactions test case. Variance density plots for the gauge locations of figure 4.14.
Fluidity-SW: ——, SWAN-fine: ×.

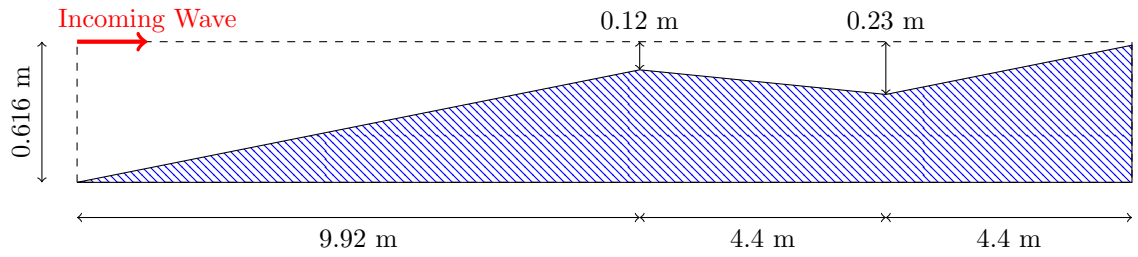


Figure 4.17: Set-up of the flume experiment by Battjes and Janssen [8] for depth-induced wave breaking.

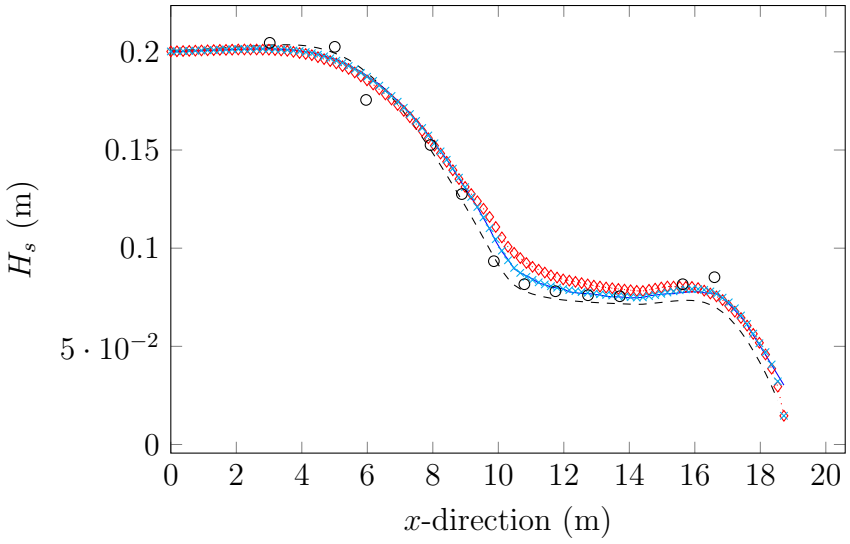


Figure 4.18: Validation for the depth induced breaking test case. The significant wave height is plotted along the $y = 9$ m line of the domain.
Battjes and Janssen [8]: ○, Fluidity-SW: ——, SWAN: ···◇···, SWAN-fine: ···×···, Fluidity-SW with triads: - - -.

in the region after the break. Increasing the spatial resolution to $\Delta x \approx 0.25\,\text{m}$ (14,412 elements) corrects this behaviour and brings the two results nearly to the same answer (SWAN-fine in figure 4.18).

Comparing the two codes against the measurements, the significant wave height is slightly under-predicted in the first region ($0 < x < 5$). In the rest of the domain the numerical results correctly represent the breaking of the wave, but do not allow the wave to shoal again in the last region ($x > 15$).

Activating triads with a low proportionality coefficient $\alpha_{\text{EB}} = 0.25$ leads to lower dissipation in the first region, giving a better match with measurements. However,

triads seem to increase the dissipation in the rest of the domain, leading to an under-estimation of the wave height. Increasing the proportionality coefficient (not included in the plot) enhances this behaviour.

4.8 Conclusions

Fluidity-SW has been tested against a wide range of different simulations which evaluate the ability to predict the linear approximation of waves (adiabatic part of equation) as well as the non-linear behaviour (source terms) in deep and shallow water. The code has been successfully validated against analytical solutions and experiments and is consistent with the results obtained with SWAN.

It has been demonstrated that the proposed scheme, with a $P1$ spatial approximation and $P0$ angular approximation exhibits little numerical diffusion which is advantageous when simulating large scale domains. At the same time when compared with the unstructured version of SWAN (which is first-order accurate in geographic space) it was shown that better results can be achieved with coarser meshes. For the three-wave interaction test case and the wave breaking test-case in particular, the same results can be achieved with up to four times bigger element-edge lengths in the spatial mesh.

Even though higher-order elements were not tested here, the scheme is formulated on arbitrary spatial and angular expansions, enabling it to be used with any type of elements to increase its accuracy and reduce the computational costs. The advantage of such flexibility is particularly demonstrated in the next chapter where a hierarchical angular expansion is proposed to formulate an efficient adaptive scheme in angle.

Chapter

FIVE

Angular adaptivity

A version of this chapter has been published under the tile: *Adaptive Haar wavelets for the angular discretisation of spectral wave models*, in the Journal of Computational Physics, doi:10.1016/j.jcp.2015.10.046 [2].

5.1 Introduction

In the ocean circulation modelling community, the wide range of spatial and temporal scales has motivated the development of spatially adaptive schemes, as a means of local and anisotropic dynamical mesh refinement. Various techniques have been developed, with examples including the structured tree-based hierarchical finite volume Gerris [68] model and the unstructured finite element Fluidity [67] model. The first effort to apply these techniques to the energy balance equation was made by Popinet et al. [69] who combined the adaptive solver of Gerris with WAVEWATCHIII to develop a spatially adaptive spectral wave model. In their work they showed a decrease of one to two orders of magnitude in run-times for practical spatial resolutions. More recently Meixner [58] was the first to apply adaptivity in spectral space. By developing a discontinuous finite element spectral wave model, p-adaptivity was applied both in geographic and spectral space. Adjusting the order of the finite element expansions gave significant speed-ups compared to using

uniform higher order expansions, in a deep water propagation test case.

This chapter focuses on applying adaptivity for the refinement of the angular resolution. It is not easy to quantify the directional distribution of ocean waves in a general framework. Observations, however, show that the directional distribution tends to be sharp around the peak frequency [31, 97]. As waves propagate outside of their generation area, direction-dispersion further enhances this. Thus, in many cases the energy spectrum only contains energy in a narrow band of directions. (This is even more obvious in coastal areas where waves appear to come from a single direction). Viewed in this perspective, uniform angular resolutions in spectral wave models are inefficient since for a specific point not all angles have non-zero energy. The adaptive approach proposed here attempts to deal with this problem though the use of compactly supported wavelet basis functions. These can locally resolve details in the angular dimension resulting in a different angular mesh for each computational point.

Wavelets, became an active field of research in the 1980's, with the works of researchers such as Morlet, Grossman and Daubechies [26] on signal processing. Starting as an alternative to Fourier analysis, their popularity soon expanded, owing mainly to the localised nature of wavelet basis in frequency and time, as well as their hierarchical structure. This meant that a localised wavelet transform could be performed with a variable-resolution reconstruction of a signal, which is ideal for applications such as data and image compression [54, 5, 21]. These advantages soon drew the attention of the numerical modelling community, as the aforementioned properties provided an efficient framework for adaptive algorithms. Since then, wavelets have been applied to various fields of numerical analysis, including turbulence modelling [32] and partial differential equations such as the Navier-Stokes [92, 98], hyperbolic [3, 71] and parabolic systems [40, 22]. A more comprehensive list of wavelets used in PDE's can be found in [24].

Of more relevance to this work, is the use of wavelets for the discretisation of the Boltzmann transport equation, which provides a natural framework for spectral wave modelling. Both the Boltzmann transport (in non-scattering media) and the energy balance equations are multi-dimensional hyperbolic systems, dealing with the propagation of an energy flux in geographic and spectral space [52]. Buchan et al. [17] first applied linear and quadratic wavelets for resolving the angular dependence of the Boltzmann transport equation, and then went on to show how they can be used for the application of angular adaptivity [18]. Goffin et al. [34] then extended

this to apply goal-based measures to the error metrics driving adaptivity.

In this work Haar wavelets (named after Alfred Haar) – piecewise constant, hierarchical, compactly supported basis functions – are used for the angular discretisation of the action balance equation and the application of anisotropic angular adaptivity. Haar wavelets are chosen for their simplicity, as well as the fact that they produce sparse system matrices compared to higher order wavelet expansions. For a historical background and an overview of wavelets in general and Haar wavelets in particular the reader can refer to [1], while a more rigorous mathematical background and review of their numerical applications can be found in [23].

The chapter is organised as follows. First in Section 5.2 a brief theoretical background of wavelets is given and the Haar wavelet functions are introduced. This is then followed by the development of the adaptive framework and the description of the adaptive algorithm in Section 5.3. Finally in Section 5.4 angular adaptivity is applied on both stationary and time-dependent test cases and the benefits of the scheme are quantified, in terms of the required degrees of freedom as well as computational run-times. This chapter is limited to the adiabatic part of the action balance equation and thus only tested on linear problems, i.e. propagation in geographic and spectral space without source terms. The application of adaptivity in realistic test cases with the source terms activated is treated in the next chapter.

5.2 Wavelets

In section 3.5 an arbitrary angular discretisation is defined in (3.14), with the use of a set of angular basis functions G_j and then in chapter 4 the scheme is validated for a $P0$ angular expansion. In this chapter the angular dimension of the action balance equation is discretised with the use of wavelets. The section below outlines the construction of these angular basis functions G_j, for Haar wavelets. This allows for the calculation of the angular matrices of (3.22) - (3.32) and the construction of the linear system of (3.45)-(3.46).

5.2.1 Multiresolution analysis

In general, wavelets are constructed with the use of multiresolution analysis (MRA) [56]. First a MRA is built and then the wavelet family can be constructed with the

desired criteria. Thus, a small introduction to MRA is necessary. A multiresolution analysis is a nested sequence V_j, $j \in \mathbb{Z}$, of subspaces of $L^2(\mathbb{R})$, the set of all Lebesgue integrable functions on the real line, i.e. the collection of functions $f : \mathbb{R} \to \mathbb{R}$ such that $\int_{\mathbb{R}} f^2 d\mathbb{R} < \infty$. The basic properties for a MRA are,

1. $V_j \subseteq V_{j+1}$, $j \in \mathbb{Z}$;
2. $\bigcup_{j\in\mathbb{Z}} V_j$ is dense in $L^2(\mathbb{R})$;
3. At each level j, there exists a set of scaling functions $\phi_{j,k}$, $k \in K^{'}(j)$ for some index set $K^{'}$, for which the set $\{\phi_{j,k} \mid k \in K^{'}(j)\}$ forms a Riesz basis of V_j.

For numerical applications, these nested spaces can be used to approximate any function $f \in L^2(\mathbb{R})$, by projecting f onto $f_j \in V_j$. In particular, using the scaling functions which span V_j the approximation becomes,

$$f \approx f_j = \sum_k \alpha_k \phi_{j,k}, \tag{5.1}$$

where j is the level of the space, k is the index number of the scaling functions for each level and α_k are the expansion coefficients which need to be determined. The accuracy of the expansion is then governed by the choice of j, as property 2 from above states that f can be fully recovered in the limit $j \to \infty$.

5.2.2 Wavelet construction

Using the MRA, wavelets can be generated as a basis for the spaces W_j that complement V_j in V_{j+1}, i.e. $V_{j+1} = V_j \oplus W_j$. These are denoted as $\{ \psi_{j,m} \mid m \in M(j) \}$, for some index set $M(j)$. Given that W_j is contained in V_{j+1}, so are the wavelet functions, i.e. $\psi_{j,m} \in W_j \subset V_{j+1}$. This means that the wavelet functions can be constructed as a combination of the scaling functions spanning V_{j+1},

$$\psi_{j,m} = \sum_{k\in K(j+1)} v_{j,m,k} \phi_{j+1,k}. \tag{5.2}$$

Recursively applying the relationship $V_j = V_{j-1} \oplus W_{j-1}$ gives,

$$V_j = V_{j-1} \oplus W_{j-1} = V_{j-2} \oplus W_{j-2} \oplus W_{j-1} = ... = V_l \oplus_{n=l}^{j-1} W_n. \tag{5.3}$$

Finally combining this with property 2 above yields,

$$L^2(\mathbb{R}) = V_l \oplus_{n=l}^{\infty} W_n. \tag{5.4}$$

Equation (5.4) defines a basis for $L^2(\mathbb{R})$ using the scaling functions in V_l, where l is the starting level for the scaling functions, and the wavelet functions spanning W_n, $n \in \{l, l+1, ..., \infty\}$. Thus any function $f \in L^2(\mathbb{R})$ can be also expressed as combination of scaling functions and wavelets as

$$f = \sum_{k \in K(l)} \alpha_k \phi_{l,k} + \sum_{n=l}^{\infty} \sum_{k \in M(n)} \beta_{n,k} \psi_{n,k}. \tag{5.5}$$

Finally, projecting f onto $f_j \in V_j \subset L^2(\mathbb{R})$ yields

$$f \approx f_j = \sum_{k \in K(l)} \alpha_k \phi_{l,k} + \sum_{n=l}^{j-1} \sum_{k \in M(n)} \beta_{n,k} \psi_{n,k}. \tag{5.6}$$

5.2.3 Haar wavelets

Before moving on to the presentation of Haar wavelets, the space V_j must be defined in terms of the governing equation. Wavelets are used for the angular discretisation of the action balance equation and thus, V_j represents the angular domain $\theta \in \{0, 2\pi\}$. In particular given a specific level l of the MRA, V_l is split into 2^l subdivisions (figure 5.1).

The Haar scaling functions, are piecewise constant functions within those intervals:

$$\phi_{l,k}(x) = \begin{cases} 1 & \text{if } x \in i_k, \\ 0 & \text{otherwise.} \end{cases} \tag{5.7}$$

The Haar wavelets are defined as

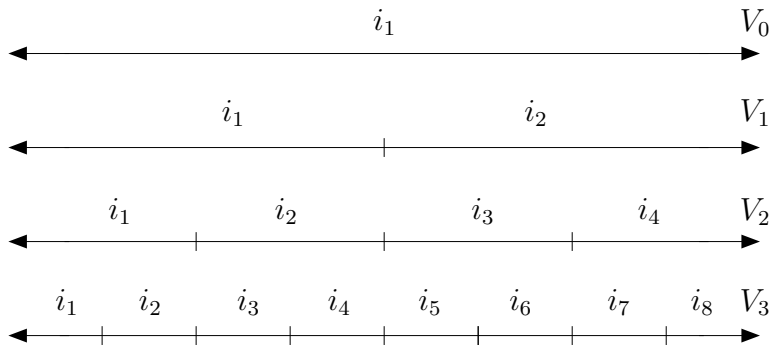


Figure 5.1: Haar wavelet MRA of the 2π angular domain. Each space V_l has 2^l subdivisions.

$$\psi_{n,k}(x) = \begin{cases} 1 & \text{if } x \in i_{2k-1}, \\ -1 & \text{if } x \in i_{2k}, \\ 0 & \text{otherwise,} \end{cases} \tag{5.8}$$

where $n \in \{l, l+1, ..., j-1\}$ for V_j. The hierarchy of scaling functions and wavelets is presented in figure 5.2. First, the scaling functions are expanded on V_l. On the first wavelet level, W_l, wavelets span the same space as the scaling functions in V_l. For every new level the number of wavelets doubles and thus each new wavelet supports half the space.

If (5.7) and (5.8) are substituted into (5.6), the Haar wavelets' approximation for any function in $L^2(\mathbb{R})$ becomes,

$$f(x) \approx \sum_{k=1}^{2^l} \alpha_k \phi_{l,k}(x) + \sum_{n=l}^{j-1} \sum_{k=1}^{2^n} \beta_{n,k} \psi_{n,k}(x). \tag{5.9}$$

Equation (5.9) shows that any function in $L^2(\mathbb{R})$ can be approximated, with a linear combination of the scaling functions on level l and the wavelets on levels $n \in \{l, l+1, ..., j-1\}$. Henceforth, the Haar wavelet discretisation is referred to as $HW_{l,j}$. Following (5.3),

$$HW_{l,j} = V_l \oplus W_l \oplus W_{l+1} \oplus .... \oplus W_{j-1} = V_j. \tag{5.10}$$

$HW_{2,5}$ for instance has 2^2 scaling functions in V_2, 2^2 wavelets in W_2, 2^3 wavelets in

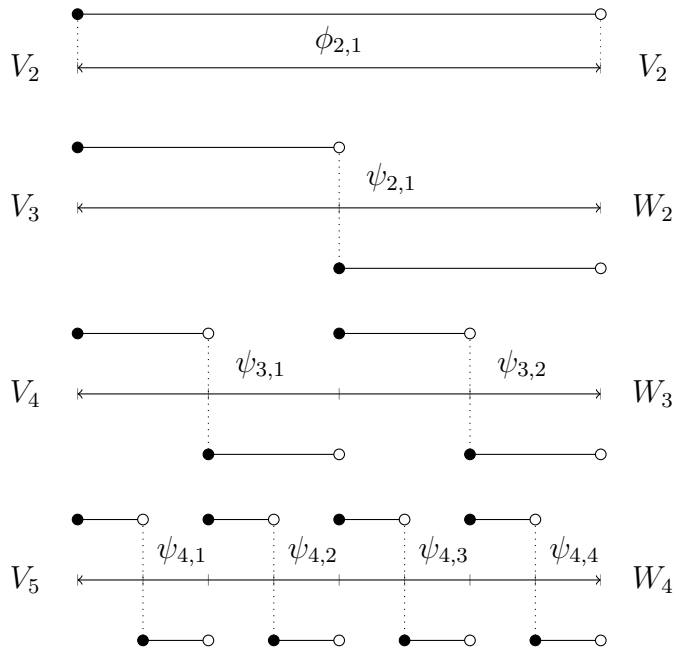


Figure 5.2: Example of Haar wavelets on a quadrant of the 2π angular domain. Each V_j space (denoted on the left) is reproduced by $V_j = V_l \oplus_{n=2}^{j-1} W_n$ (denoted on the right). Space V_5 can be thus reproduced by $V_5 = V_2 \oplus W_2 \oplus W_3 \oplus W_4$.

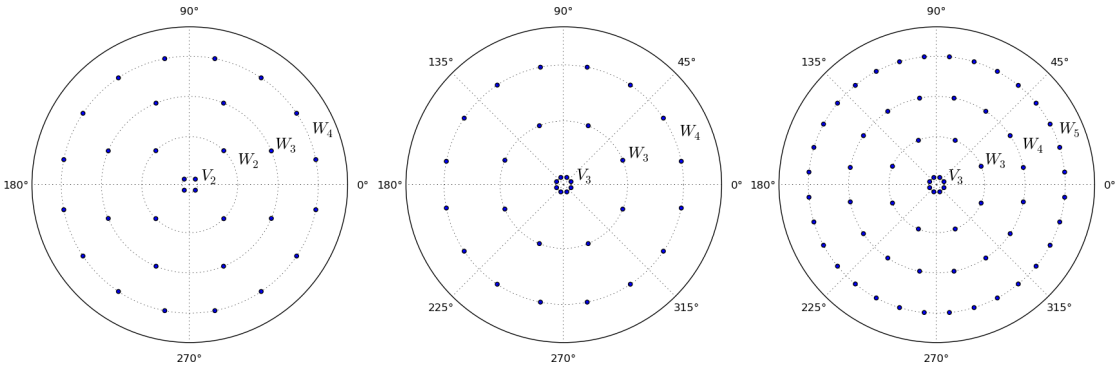
W_3 and 2^4 wavelets in W_4. The resulting space is V_5 with a cumulative number of functions equal to $2^5 = 32$ (figure 5.2). To visualise the angular mesh, polar plots are used that show the position of the functions (middle point) for all the levels (figure 5.3).

5.2.4 Calculating the angular matrices

Equation (5.9) provides an expression for representing a function with Haar wavelets. Assuming the levels of the scaling functions and wavelets are known, the number of functions used for the projection is also known. Then (5.9) can be condensed to the single summation given in (3.14):

$$N(\mathbf{r}, t, \sigma, \theta) \approx \sum_{j=1}^{K} N_j(\mathbf{r}, t, \sigma) G_j(\theta),$$

where N_j corresponds to the coefficients α, β and G_j to the functions ϕ and ψ of (5.9). Thus, scaling functions and Haar wavelets are now simply referred to as



(a) $HW_{2,5} \rightarrow 32$ functions **(b)** $HW_{3,5} \rightarrow 32$ functions **(c)** $HW_{3,6} \rightarrow 64$ functions

Figure 5.3: Polar plots for various Haar wavelet expansions. Each concentric circle represents the spaces: $\{V_l, W_l, W_{l+1}, ..., W_{j-1}\}$, for a $HW_{l,j}$ discretisation.

angular basis functions. Having the approximation for the angular dependence of the action density, all that is needed for the implementation of Haar wavelets is to calculate the angular matrices $\mathbf{A}_{\mathrm{s},\mathbf{x}}$, $\mathbf{A}_{\mathrm{s},\mathbf{y}}$, $\mathbf{M}$, $\mathbf{H}_\theta$, $\mathbf{H}_\sigma$, $\mathbf{H}_\sigma^{\mathrm{U}}$, $\mathbf{H}_\sigma^{\mathrm{D}}$, $\mathbf{H}_{\mathrm{S}}^{\mathrm{lhs}}$ and $\mathbf{H}_{\mathrm{S}}^{\mathrm{rhs}}$ of (3.22) - (3.32), presented in section 3.5.

The vast majority of the available spectral wave models, use a finite difference approximation for the angular dimension. This is the equivalent of a cell centred finite element $P0$ discretisation (which is the angular expansion used to validate the model in chapter 4). In the Boltzmann transport community this is known as discrete ordinates or SN [52]. If the angular matrices are calculated for this expansion then there exists a mapping operator $\mathcal{W}$, which maps the $P0$ space to the Haar space (both are piecewise constant, so the mapping is exact). The relationship is

$$\mathcal{W}N_W = N_{P0}, \tag{5.11}$$

where N_W and N_{P0} correspond to the action density approximated in the wavelet space and the $P0$ finite element space respectively. This mapping is applied to the angular matrices by pre-multiplying and post-multiplying by $\mathcal{W}^\mathcal{T}$ and $\mathcal{W}$ respectively as,

$$\mathbf{A}_{\mathbf{x}}^{\mathbf{W}} = \mathcal{W}^\mathcal{T}\mathbf{A}_{\mathrm{s},\mathbf{x}}^{\mathbf{P0}}\mathcal{W}. \tag{5.12}$$

The use of the mapping operator simplifies the implementation of Haar wavelets,

allowing them to be built on the existing framework, i.e. there is no need to recalculate the angular matrices in Haar space. The mapping matrix $\mathcal{W}$ is a sparse square matrix of 1's and -1's, which gets sparser as the number of angles grows. Thus, the mapping can be significantly optimised by exploiting the sparsity of the operator. At the same time all the angular matrices are diagonal in $P0$ space, except for the refraction matrix $\mathbf{H}_\theta$. Additionally $\mathbf{A}_{\mathrm{s},\mathbf{x}}$ and $\mathbf{A}_{\mathrm{s},\mathbf{y}}$ do not have a spatial dependence and need only be calculated once to be used for all the elements of the spatial domain. The most expensive operation is then the mapping of $\mathbf{H}_\theta$. The real utility of the mapping operator, however, is in the calculation of the source terms and in particular the DIA (see section 2.4.3) which assumes that the angular domain is composed of discrete angles. The source terms with Haar wavelets are treated in the chapter 6.

5.3 Angular adaptivity

The application of anisotropic angular adaptivity, i.e. allowing the model to use a different angular discretisation for each spatial node, would normally require the reconstruction of the angular matrices (3.22) - (3.32) for each spatial node at each adaptive time-step. This can be a cumbersome task with a significant computational cost. Fortunately, the whole process can be easily simplified with the use of hierarchical expansions, such as the Haar wavelets used here. To make this clear, assume that a uniform expansion is applied globally. The coefficients of this expansion will be high at spatial nodes where the action density is high, and low in areas of low action density. As these coefficients get smaller a filter can be applied to zero them out and eventually remove them from the expansion. This is known as thresholding and used for data compression [1].

Applying this on an adaptive framework, the angular matrices are calculated for a uniform expansion, and for each spatial node only the coefficients that are above the threshold are added to the final system. This is where the real benefits from the use of Haar wavelets can be seen, due to their compact support; every time a new level gets added the support of the wavelets becomes smaller, focusing on more detail in the angular domain. Thus, an adaptive scheme with wavelets, allows for the concentration of angles on specific patches of the angular domain for each spatial node. This can significantly reduce the total number of basis functions. An added benefit of their hierarchical nature is that there is no need to interpolate between

consecutive angular meshes. Projecting one adapted angular mesh onto the next simply consists of copying the existing angular coefficients over to the new angular mesh.

Thus, adapting in this framework simply consists of thresholding the angular coefficients every time the system gets assembled; the cost of adaptivity is negligible. The added cost comes from the use of wavelets. Firstly the angular matrices need to be mapped and secondly compared to a $P0$ angular expansion, wavelets lead to denser angular matrices which means that for a uniform (non-adapted) expansion wavelets will be slower. However, Haar wavelets are still sparse, i.e. the extra cost is small, and the ability to have a variable angular mesh compensates for the added computational effort.

5.3.1 Error measure

Haar wavelets provide a natural framework for identifying the regions where the action density is under- or over- resolved and hence the computational resolution should be altered. Each wavelet coefficient gets smaller as its importance becomes smaller. Thus, a magnitude-based error metric can be defined to indicate whether a wavelet coefficient is sufficiently small to be removed, or sufficiently large for its higher level hierarchical wavelets to be added. A simplified example is presented in figure 5.4.

Buchan et al. in [18] suggest that an appropriate error metric to be used is $N_j G_j A_j$ where N_j is the angular coefficient, G_j the basis function and A_j the support area of the basis function. However, for the Haar wavelets the basis functions switch between 1 and -1 and, after some initial results, the introduction of the area did not appear to have a significant impact. Thus, the error metric is implemented as

$$N_i > \tau. \tag{5.13}$$

If the angular coefficient is greater than a user-defined tolerance value τ then the error is considered significant, suggesting that more resolution should be added to this region, i.e. wavelets from the next level should be included. This could be repeated until enough levels have been added, such that none of the values for N_i are bigger than τ. However, in practice it is better to restrict the maximum number of levels. This means that both a $HW_{l,j_{\text{init}}}$ and a $HW_{l,j_{\max}}$ are defined, for the initial

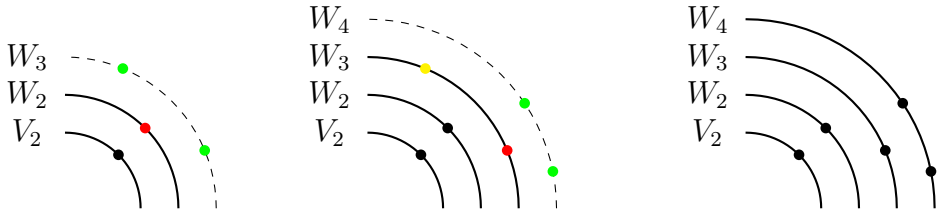


Figure 5.4: Simplified example of the angular adaptive scheme. Starting from the left sketch the red basis function suggests that the respective next level (dashed line) basis functions(green) should be added, i.e. the wavelet coefficient is bigger than the tolerance $N_i > \tau$. The central sketch shows that one of the two newly added basis functions can be removed (yellow), while the other requires yet another level. The sketch on the right shows the final adapted system.

and finest possible discretisation respectively.

Finally a way to remove basis functions is also needed to ensure that there are no over-resolved regions. This threshold is set to $N_j < 0.01\tau$; every time an angular coefficient is smaller than 0.01τ it is removed. This does not apply to scaling functions.

5.3.2 Adaptive procedure

The overall adaptive procedure can be described as,

1. Start with a $HW_{l,j_{\text{init}}}$ discretisation, choose the maximum value $j_{\max}$ and a tolerance value for the error metric τ (5.13).
2. Run the non-adapted $HW_{l,j_{\text{init}}}$ system.
3. Loop every angular coefficient N_i for every spatial node and evaluate if they are within the error bounds,

   if $N_i/\tau > 1$ $\rightarrow$ If not at max level, add the next level functions for N_i,
   if $N_i/\tau < 0.01$ $\rightarrow$ If not a scaling function, remove N_i,
   if $0.01 \leq N_i/\tau \leq 1$ $\rightarrow$ Keep N_i.

4. Reassemble the system matrices (see appendix A), but only add the components of the angular matrices, corresponding to the adapted angular coefficients.

5. For stationary simulations, repeat the above process until convergence (i.e. the algorithm has stopped changing the angular mesh), or a maximum number of adapts has been reached.

6. For non-stationary applications, choose an adapt period to specify at which time-steps the adaptivity algorithm will be evoked.

Owing to the SGS method (section 3.6), the action density is discontinuous. The system that gets assembled, however, is continuous. A continuous error metric is, thus, necessary to apply to the adaptive algorithm. One way to derive this is by looping over the elements containing the same nodes and keeping the maximum values, while a similar approach can be used to get a single error value for all frequencies. The frequency groups are looped over and the maximum value for the action density is kept for the error metric.

Finally a note on the use of the scaling functions. Given that $HW_{2,5}$ and $HW_{3,5}$ both result in the same number of basis functions (see figure 5.3), one could enforce the scaling functions to always start from the same level, i.e. level $l = 0$, and simplify the representation of wavelets to HW_j. However, the scaling functions are the only angular basis functions that the adaptive algorithm cannot remove; thus by changing l, the minimum number of basis functions can be easily controlled giving an extra degree of freedom in the adaptive procedure. This could prove important in transient simulations when the wave field changes abruptly. The adaptive algorithm might not have enough time to resolve these areas and a minimum number of functions could be necessary to provide an accurate representation.

5.4 Numerical results

To present the adaptive framework and attempt to quantify its benefits two test cases are selected. The first one is the stationary depth-induced shoaling and refraction test case (section 4.3). This is a highly directional problem, where the angular resolution dominates the errors. The second is an idealised deep water propagation scenario which is a standard test case for studying the "Garden Sprinkler Effect" (GSE). The GSE is a direct result of the angular discretisation and thus highly sensitive to the angular resolution. Since no effort has been spent to optimise the code, the results are not compared against other spectral wave models. Instead

Haar adaptivity is compared against a $P0$ angular expansion within the same code to demonstrate the advantages of the proposed numerical framework.

5.4.1 Depth-induced shoaling-refraction

Here the same test case presented in section 4.3 is used. A long wave propagates from deep to shallow water in a 4 km $\times$ 4 km domain (figure 4.3a). The wave enters from the deep eastern boundary with $d = 20$ m, at an angle of 210°, propagating towards the shallow western boundary with $d = 0.05$ m (figure 4.3c). A monochromatic wave is set-up with a significant wave height of 1 m, a frequency of 0.1 Hz and a $\cos^{500}(\theta)$ directional distribution. The mean angle of direction can then be compared to equation (4.2).

First an angular convergence test for the uniform P0 angular mesh is set-up, presented in figure 5.5. For each simulation the number of angles is doubled and the discrete root-mean-square (RMS) error plotted, compared to (4.2), along the $y =$ 1,000 m line (dashed line of figure 4.3b). This is presented by the blue line in figure 5.5, where first order convergence $(p + 1)$ is achieved. In these simulations, the angles are uniformly applied to all the spatial nodes of the domain. However the directional width is narrow which means that as the angular mesh is refined, a very small number of the angles have a non-zero action density.

Adaptive Haar wavelets are now used and compared to the uniform $P0$ results. For the application of angular adaptivity in stationary simulations it is advised to start with a coarse angular mesh, i.e. at the scaling function level. Each adaptive iteration then gradually introduces new angular basis functions, until the system converges, i.e. the algorithm stops changing the angular mesh and there is no change in the action density. This way the computational costs are small and only grow according to the errors of the simulation. In practice the convergence criteria should be relaxed to a percentage of the change of the action density (or the significant wave height), as after a point the change in the action density will be too small to justify the extra cost of re-running the system.

For each $HW_{l,j}$ simulation the scaling function and initial levels are $j_{\text{init}} = l = 3$. The maximum level $j_{\max}$ is increased and the RMS error is plotted, compared to (4.2), along the along the $y = 1{,}000$ m line (dashed line of figure 4.3b). The results for a $HW_{3,j}$, $j_{\max} \in \{4, 5, 6, 7, 8, 9, 10\}$, discretisation with tolerances $\tau \in \{1, 10^{-1}, 10^{-2}\}$

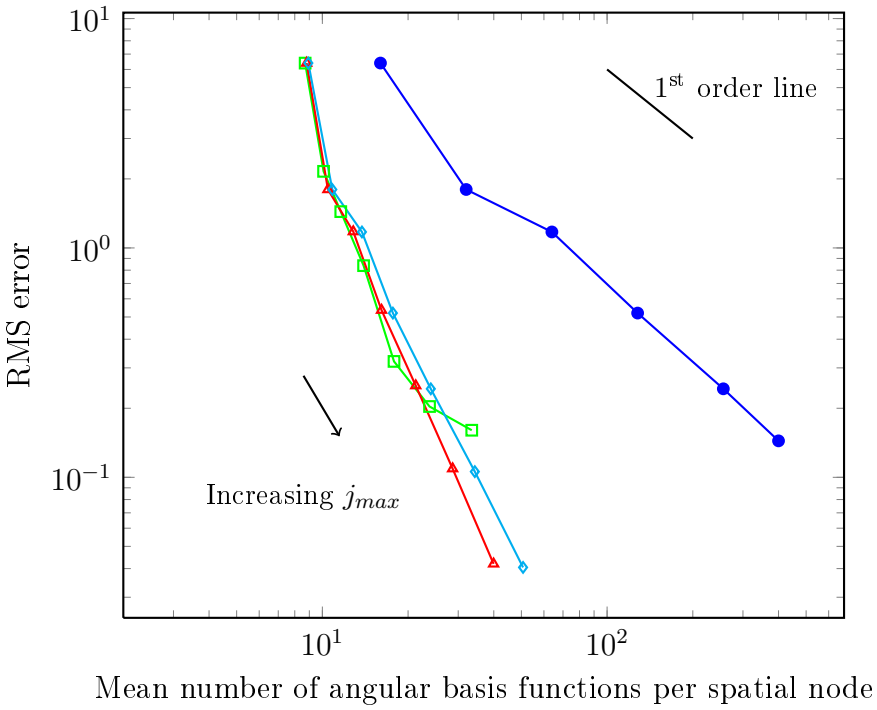


Figure 5.5: Depth induced refraction. Convergence tests for uniform $P0$ and $HW_{3,j}$, $j_{\max} \in \{4, 5, 6, 7, 8, 9, 10\}$, adaptive discretisations for various tolerances: $\tau = 1$ $\tau = 10^{-1}$, $\tau = 10^{-2}$. The $HW_{3,j}$ points correspond to the results after the adaptive algorithm converges.

are presented in figure 5.5.

For a tolerance $\tau = 1$, as $j_{\max}$ increases the errors appear to level out. As new levels are introduced, the values of the action density coefficients N_i become smaller, until they are ignored by the adaptive algorithm. Thus, even though $j_{\max}$ increases there is not enough resolution to represent the directional distribution of the action density and the errors stop decreasing. This is a clear indication that the selected tolerance value is too large. Decreasing the tolerance to $\tau = 10^{-1}$ amends this and produces errors comparable to the uniform resolution discretisation. A further reduction of the tolerance to $\tau = 10^{-2}$ produces similar errors to $\tau = 10^{-1}$, with a higher number of angular basis functions. This means that as the tolerance is further decreased, new basis functions are introduced that do not have a significant impact on the errors of the simulation. Indeed, for an infinitesimal value of τ adaptivity should uniformly add all the angular basis functions producing the same results as the uniform $P0$ discretisation. It is the balance between accuracy and computational costs that ultimately defines the tolerance value.

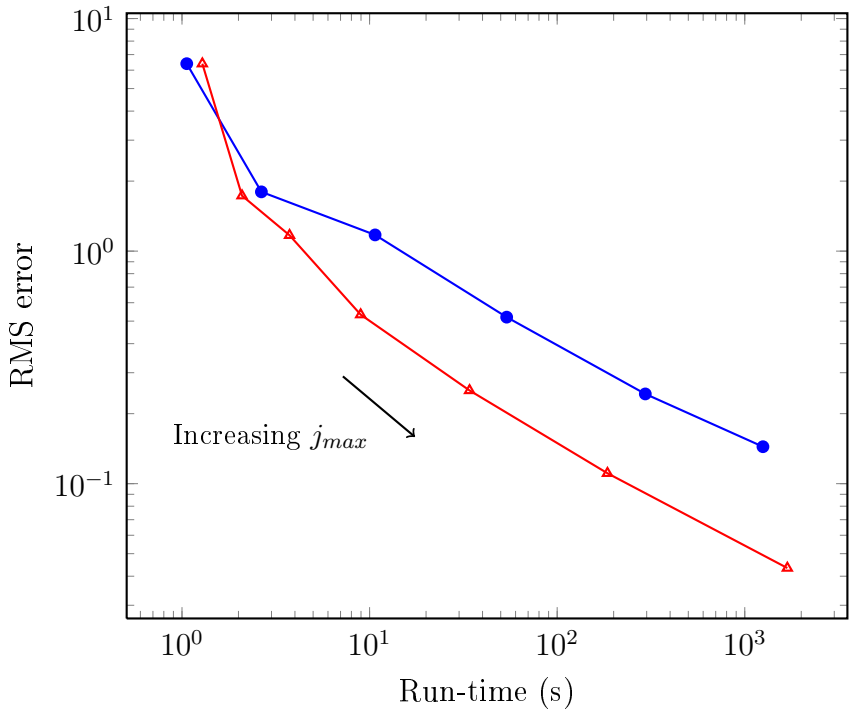
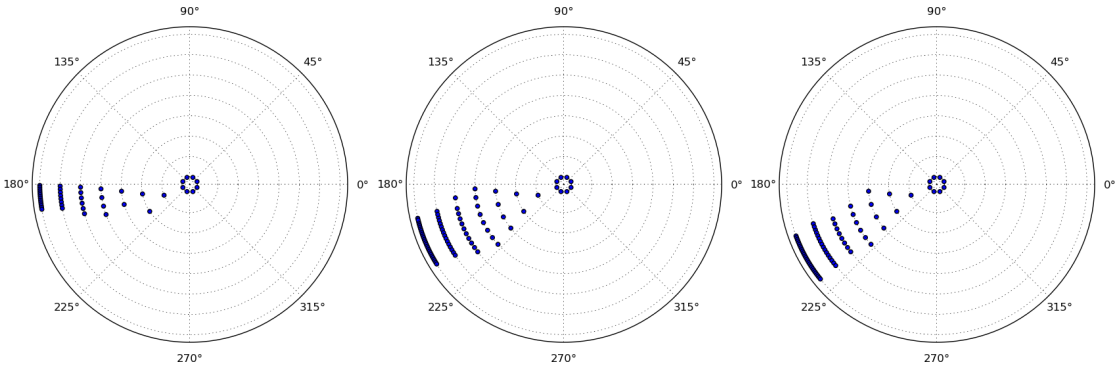


Figure 5.6: Depth induced refraction. Convergence tests for uniform $P0$ with $\{16, 32, 64, 128, 256, 400\}$ angles and $HW_{3,j}$, $j_{\max} \in \{4, 5, 6, 7, 8, 9, 10\}$, adaptive discretisations for a tolerance $\tau = 10^{-1}$. The $HW_{3,j}$ points correspond to the results after the adaptive algorithm converges.

In terms of the computational degrees of freedom, the adaptive $HW_{3,j}$ discretisations consistently use fewer degrees of freedom compared to the uniform $P0$ discretisations. The error level for a $P0$ angular discretisation with 128 angles is achieved with almost an order of magnitude less degrees of freedom by the adaptive $HW_{3,7}$ discretisation. Moving towards finer angular meshes, this difference becomes even bigger, showing the advantages of angular adaptivity for high fidelity results.

To see how this translates in computational times, the results with a tolerance $\tau = 10^{-1}$ are isolated and the errors against the run-times are plotted in figure 5.6. These are the results after each simulation has converged. For the same error levels adaptive $HW_{3,j}$ discretisations run consistently faster, with differences approaching an order of magnitude for fine resolutions. For the uniform $P0$ angular discretisation with 128 angles, the same error is achieved by the $HW_{3,7}$, six times faster. It is worth noting that the $HW_{3,j}$ converges after ten adaptive steps, i.e. solving ten times the adapted system is six times faster than solving the uniform system once.



(a) Point a **(b)** Point b **(c)** Point c

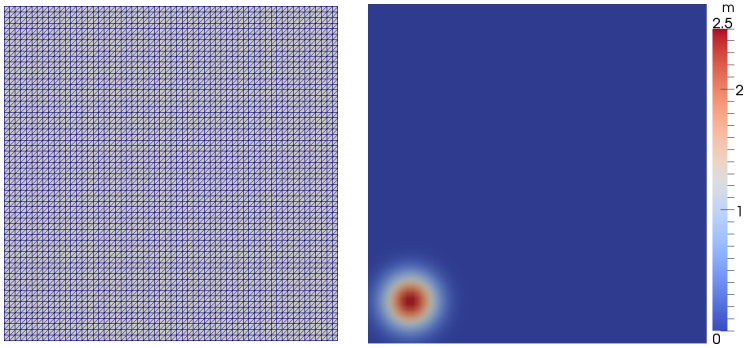
Figure 5.7: Polar plots for a $HW_{3,10}$ discretisation for points: $a = (0\text{ m}, 1000\text{ m})$, $b = (2000\text{ m}, 1000\text{ m})$, $c = (4000\text{ m}, 1000\text{ m})$.

Finally in figure 5.7 the polar wavelet plots for a $HW_{3,10}$ discretisation with a tolerance of $\tau = 10^{-1}$ are presented for three different locations with coordinates: $a = (0\text{ m}, 1000\text{ m})$, $b = (2000\text{ m}, 1000\text{ m})$, $c = (4000\text{ m}, 1000\text{ m})$. As the wave propagates from point c to point a, its mean direction shifts from 210° to 180°. The angular basis functions follow the change of the mean direction refining only the patches of the angular domain that are active for each spatial node.

5.4.2 Deep water propagation

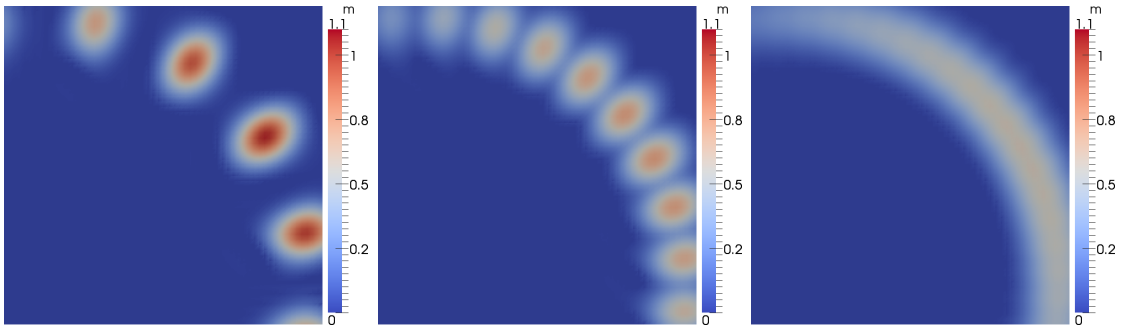
An inherent problem of the spectral space discretisation is the spurious separation of energy into the discretised bins. This is called the "Garden Sprinkler Effect" and has has been extensively studied in [12, 86, 69]. (In the Boltzmann transport community this is known as the ray effect). To showcase this effect in the angular dimension, a large spatial domain (4,000 km × 4,000 km) is simulated, with a monochromatic wave propagating over a long distance in deep water ($d = 10{,}000\,\text{m}$). For the spatial discretisation a structured triangle mesh is used, with an element edge length of 67 km (figure 5.8a). The initial wave field, located 500 km from the lower and left side has a Gaussian distribution in space, with a significant wave height of $H_s = 2.5$ m and a standard deviation of 150 km (figure 5.8b). Its mean direction is 30° with an angular distribution of $\cos^2(\theta)$ and a frequency of 0.1 Hz. The simulation is time-dependent without any source terms activated and runs for 5 days with a time-step of 600 s.

In figure 5.9, the results at the final timestep for a $P0$ angular discretisation with



(a) Spatial mesh **(b)** Initial field

Figure 5.8: Spatial mesh and initial conditions for the deep water propagation test case.

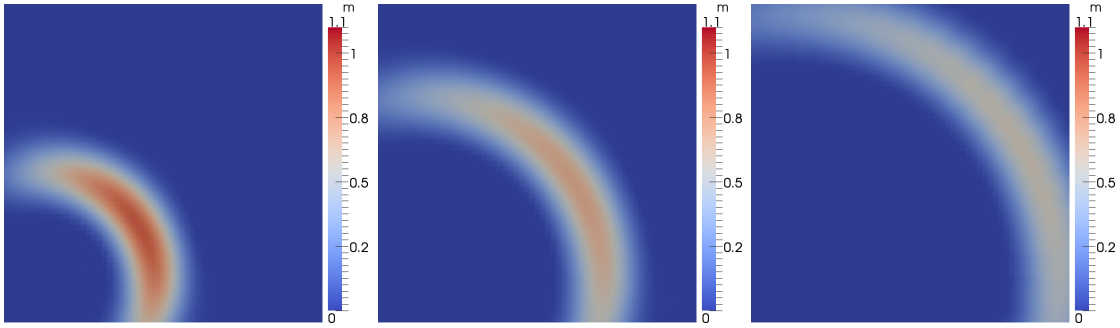


(a) $P0$ - 16 angles **(b)** $P0$ - 32 angles **(c)** $P0$ - 64 angles

Figure 5.9: Significant wave height after 5 days of deep water propagation, for a $P0$ angular discretisation with various angular resolutions.

16, 32 and 64 basis functions are presented. As the wave propagates, it breaks up into the paths of the prescribed directions; the coarser the angular discretisation, the more intense the GSE will be. This is also connected to the numerical diffusion of the spatial discretisation. Higher order schemes have a lower numerical diffusion, which intensifies the GSE. This essentially means that increasing the resolution in geographic space makes the GSE worse.

The obvious solution is to increase the number of angles. However, in the multidimensional framework of the action balance equation increasing the number of angles globally significantly affects the computational costs. With a finite element expansion, as the one presented here, doubling the angular basis functions quadruples the size of the angular matrices. This increased computational cost for finer angular resolutions, led to the use of a diffusion correction term by [12], which smears out



(a) $t = 2$ days. **(b)** $t = 3.5$ days. **(c)** $t = 5$ days.

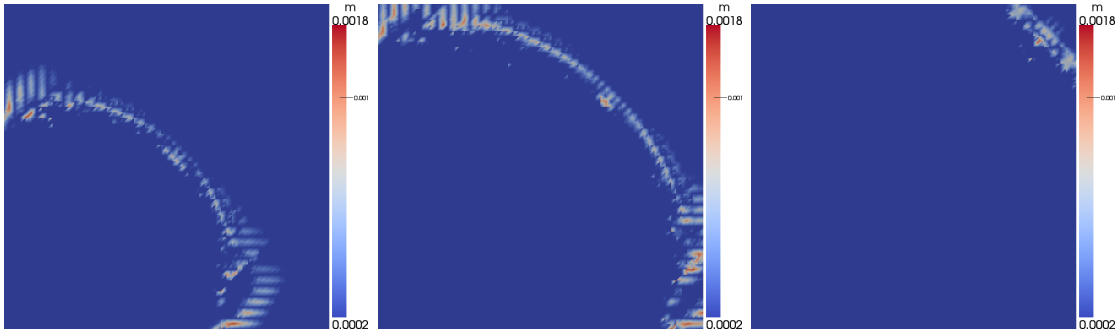
Figure 5.10: Significant wave height for an adaptive $HW_{2,6}$ discretisation with tolerance $\tau = 10^{-6}$ at several time levels.

the action density depending on the wave age. By knowing how much the wave field has propagated, it can be spread accordingly to alleviate the GSE. Calculating the wave age, however, is costly, leaving the age as a tunable coefficient, which introduces inaccuracies.

Here, as an alternative, angular adaptivity is used, to increase the accuracy of the solution while keeping the computational cost at a minimum. A $HW_{2,6}$ discretisation is applied, with a tolerance value of $\tau = 10^{-6}$. This introduces a maximum of $2^6 = 64$ basis functions, making the results comparable to the uniform $P0$ with 64 angles. By starting the simulations at the scaling function level, as in the stationary example, the initial $\cos^2(\theta)$ distribution is only represented by 4 angles. This, of course, introduces errors which then propagate throughout the simulation. Thus, the simulation starts at the maximum angular discretisation $j_{\text{init}} = j_{\max}$. (An alternative would have been to be able to adapt a few times at the first timestep before propagating in time). Given that the cost of adapting is negligible, adaptivity is activated at each time-step.

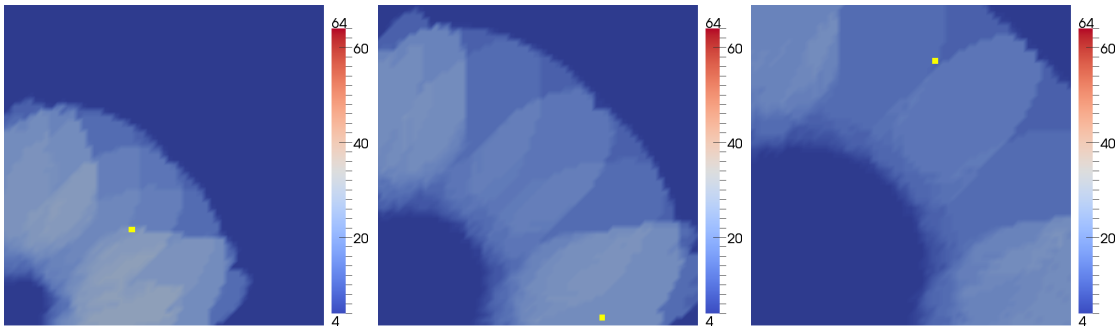
In figure 5.10 the adaptive run is presented at various time levels, while figure 5.11 shows the difference between the significant wave height for the $HW_{2,6}$ and $P0-64$ angles runs. The results are readily comparable, with differences in the order of mm.

However, capturing the solution is only part of the goal, as the objective is the reduction of the computational cost. To showcase this, the angular mesh, or the distribution of the number of angular basis functions in space, is presented in figure 5.12. The angular mesh can be seen following the propagation of the wave field,



(a) $t = 2$ days. **(b)** $t = 3.5$ days. **(c)** $t = 5$ days.

Figure 5.11: Absolute difference in significant wave height between a $P0-64$ angle and an adaptive $HW_{2,6}$ discretisation with tolerance $\tau = 10^{-6}$ for various time levels. Colorbar in logarithmic scale.



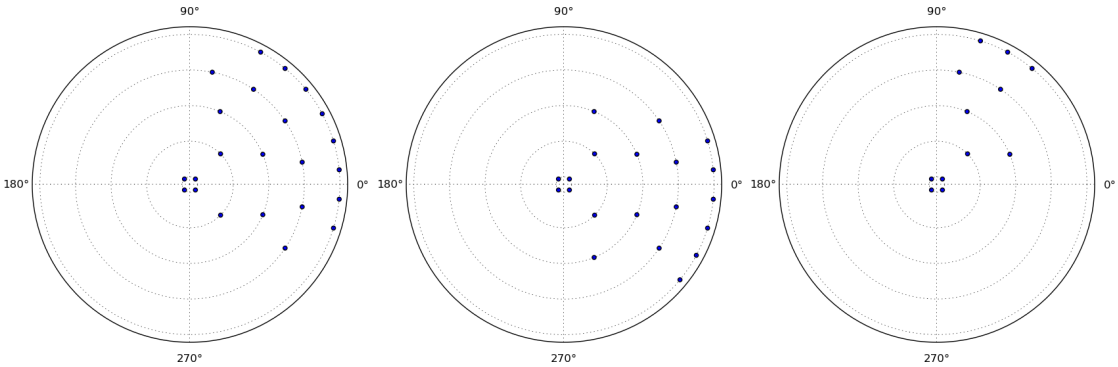
(a) $t = 2$ days. **(b)** $t = 3.5$ days. **(c)** $t = 5$ days.

Figure 5.12: Angular mesh, i.e. number of angular basis functions, for a $HW_{2,6}$ discretisation with tolerance $\tau = 10^{-6}$ at various time levels. The polar plots for the points denoted by the yellow dots are presented in figure 5.13.

surrounding the area around it. It is worth observing that the maximum errors in figure 5.11 occur at the edges of this area. The smaller the prescribed tolerance, the bigger the region of increased adapted angles will be and thus the smaller the error.

Finally in figure 5.13 the polar plots for the three geographical points denoted by the yellow dots in figures 5.12a–5.12c, are presented at their respective time levels. For each point, the wave field has a different mean direction and directional distribution. Adaptivity adjusts the number and position of angular basis functions accordingly.

To better quantify the savings in the computational costs from using angular adaptivity a convergence test is now presented. First the $P0$ angular discretisation is tested. With 300 angles used to construct the reference solution, the number of



(a) $t = 2$ days. **(b)** $t = 3.5$ days. **(c)** $t = 5$ days.

Figure 5.13: Polar plots of a $HW_{2,6}$ discretisation for the points in figure 5.12, at their respective time levels.

angles is gradually increased and the $l2$ norm of the significant wave height for the final timestep is plotted against the run-time. This is presented in the blue line of figure 5.14.

For the adapted runs, a $HW_{2,j}$, $j_{\max} \in \{3, 4, 5, 6, 7, 8\}$, discretisation is used with tolerances $\tau \in \{10^{-6}, 10^{-7}, 10^{-8}\}$. The results are presented in figure 5.14. As $j_{\max}$ is increased the maximum number of basis functions is doubled and the $HW_{2,j}$ lines move towards higher run-times and smaller errors. Using a smaller tolerance value, adaptivity inserts more angles and thus the run-times are higher. However, up to $j_{\max} = 7$ the errors are the same for all tolerances, i.e. the extra angular basis functions that are inserted do not significantly impact the error. A significant difference can only be seen for the last value of $j_{\max} = 8$. This is the point where the accuracy of the solution is comparable to the tolerance limit and thus decreasing the tolerance produces better results. For the case of $\tau = 10^{-8}$ the highest value of $j_{\max} = 8$ gives the same error values as the respective uniform $P0$ runs. This is a useful guide to how the tolerance should be tuned depending on the desired accuracy.

The adaptive simulations are consistently faster compared to the uniform resolution ones. The same error produced by a uniform $P0$ angular discretisation with 128 angles is achieved almost an order of magnitude faster by the $HW_{2,7}$ adaptive discretisation. As the angular resolutions increase this difference becomes bigger. This is due to the reduced number of degrees of freedom, as is evident in figure 5.15, where the mean number of angular basis functions for a tolerance of $\tau = 10^{-6}$ is plotted at each time level. At the first time level, the simulation starts with the

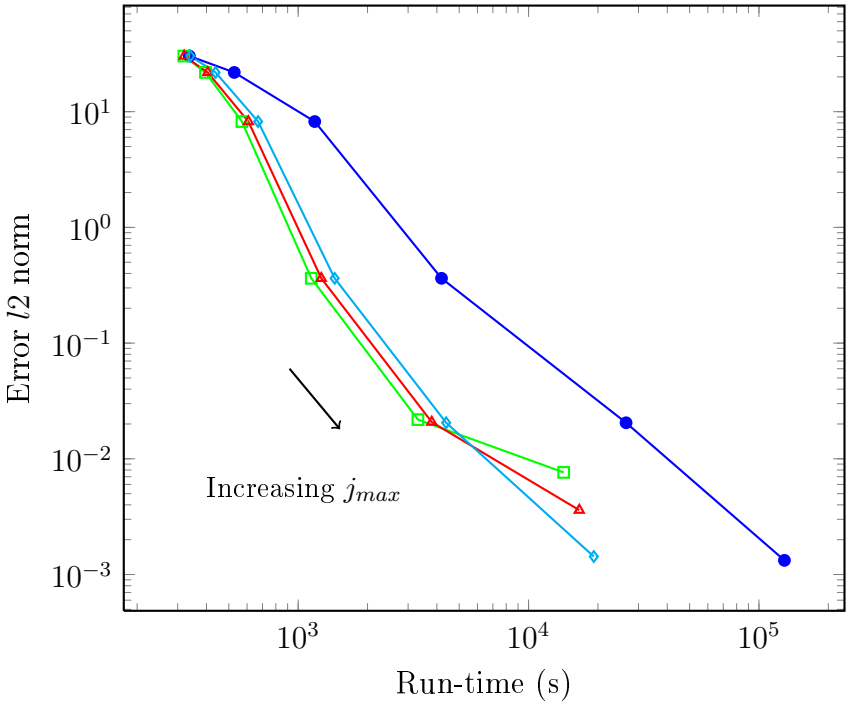


Figure 5.14: Error against run-time for the deep water propagation test case. Results for $P0$ with $\{8, 16, 32, 64, 128, 256\}$ angles and $HW_{2,j}$, $j_{max} \in \{3, 4, 5, 6, 7, 8\}$, for tolerances: $\tau = 10^{-6}$, $\tau = 10^{-7}$, $\tau = 10^{-8}$. Each point corresponds to the error compared to a uniform $P0$ discretisation with 300 angles, at the final time level.

maximum number of angles so as to accurately represent the initial angular distribution. After the first adapt, the mean number of basis functions immediately drops and the simulations run consistently with up to an order of magnitude fewer degrees of freedom. As the wave field propagates it spreads covering a larger computational area. Thus, the degrees of freedom increase towards higher time levels, only to decrease again when parts of the wave field exit the domain. This constant adjustment of the degrees of freedom ensures that the computational costs are always optimised depending on the desired accuracy.

5.5 Conclusions

Due to the multidimensional nature of the action balance equation, the computational costs associated with its solution renders the use of high fidelity discretisations expensive and inefficient. This means that in realistic domains, the number of angles

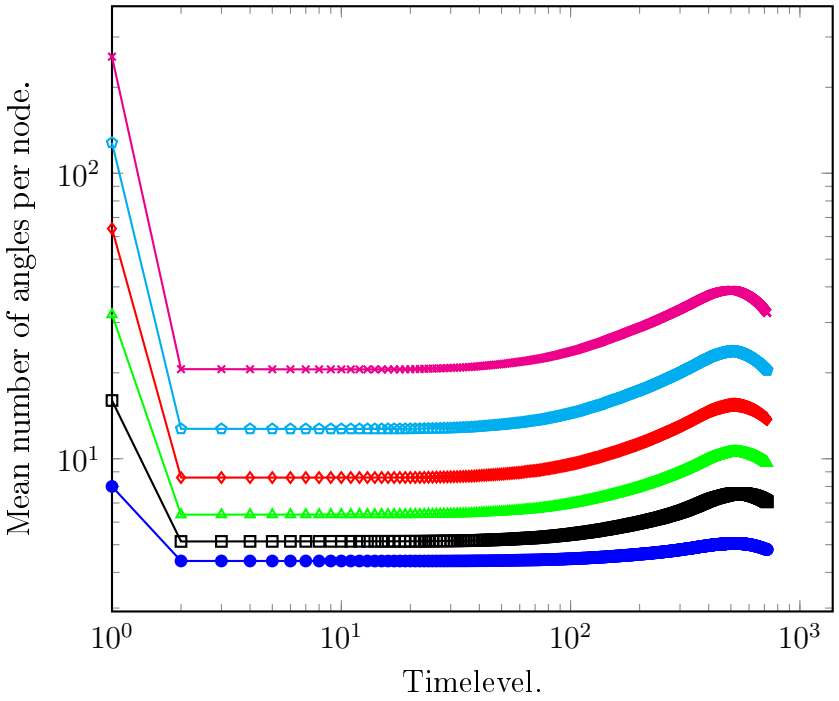


Figure 5.15: Mean number of angular basis functions against timelevel for the deep water propagation test case. $HW_{2,3}$ —●—, $HW_{2,4}$ —□—, $HW_{2,5}$ —△—, $HW_{2,6}$ —◇—, $HW_{2,7}$ —⬠—, $HW_{2,8}$ —×—, for a tolerance of $\tau = 10^{-6}$.

used needs to be kept small. In general, however, sea surface wind-wave fields are directional and thus in most cases the majority of angular degrees of freedom do not significantly impact on the accuracy of the solution. What is more, the mean direction of the wave field is constantly changing and the rate of this change is subject to external forces, such as the wind, currents and the bathymetric slope. Hence, a-priori estimation of the required angular mesh resolution is challenging.

To resolve this problem, this chapter introduced a new framework for applying angular adaptivity in spectral wave models. The method employs hierarchical angular expansions, using Haar wavelets to represent the angular dependence of the action density. The adaptive procedure uses the hierarchy and compact support of wavelets to locate the areas on the angular mesh that are under-resolved and increase the number of angular functions to locally refine the resolution. At the same time, areas that are over-resolved are identified and functions removed to decrease the global degrees of freedom without negatively impacting on the accuracy. By controlling the minimum and maximum number of basis functions, as well as the tolerance for the error metric the balance between errors and computational costs is easily managed.

The method was applied to a steady state depth induced shoaling-refraction test case, as well as a transient large scale propagation test case. The adaptive results were verified against a uniform resolution discretisation and the gains in terms of computational degrees of freedom and run-times were quantified.

Wavelets were constantly rearranged for each geographic point following the mean direction and capturing the directional distribution of the wave field. Thus, the same error levels, compared to a uniform expansion, were achieved in both cases with lower computational costs and faster run times. In particular, for an angular resolution of 128 angles, adaptivity used an order of magnitude less degrees of freedom compared to the uniform resolution. This translated in six times faster run-times for the shoaling-refraction test case and almost an order of magnitude faster run times for the large scale propagation test case. This refers to the total run-times including both the linear solves and the adapt process. The difference widened as the angular mesh was further refined, showing the advantage of adaptivity for high fidelity results.

In all the results presented the objective was to show that adaptive wavelets can reproduce the same errors as the equivalent uniform resolution angular meshes. Thus, the convergence criteria were strict and the tolerance limits low. In practical simu-

lations the convergence criteria and tolerance limits need to be linked to the change of the significant wave height, which will result in fewer angular basis functions and, thus, faster run-times. Speed-ups can also be achieved by optimising the scheme, such as exploiting the sparsity of the angular matrices for the mapping from $P0$ to Haar space.

Haar wavelets provide an effective framework for applying anisotropic angular adaptivity, refining the angular resolution according to the desired accuracy while at the same time reducing the computational costs. This can push spectral wave models towards higher resolutions and help bridge the gap between coarse large scale and fine coastal zone simulations.

Chapter

SIX

Verification

6.1 Introduction

In chapter 4 the proposed scheme was validated against a wide range of simulations that tested both the adiabatic part (linear) and the source terms. However, none of these cases had all the source terms activated at the same time, since the main objective was to isolate and validate the individual physical processes. Then in chapter 5 a new adaptive scheme in angle was formulated and compared against uniform angular resolutions. The validity and efficiency of the scheme was investigated by applying it to two highly directional, linear problems, but it was not tested with the source terms activated.

To conclude this work, this chapter tries to fill these two gaps, as well as introduce dynamic spatial mesh refinement. The code (with a fixed spatial and angular mesh) is applied to a realistic scenario that requires the use of all the source terms. Then angular adaptivity (with a fixed spatial mesh) is activated to showcase its validity, even in cases where the source terms dominate the system. Finally, preliminary results from the application of spatial adaptivity (with a fixed angular mesh) on the same case are presented, to showcase the ability to dynamically adapt the spatial mesh and improve the accuracy of the solution, while keeping the computational cost low.

In the next sections the Haringvliet estuary is used for the verification of the code. The bathymetry and spatial mesh are taken from the Haringvliet case in the SWAN web-page [82]. First, in section 6.2, the results of Fluidity-SW with a uniform $P0$ angular discretisation are compared against wave measurements and results obtained with SWAN. Then, in section 6.3, angular adaptivity is activated with the use of Haar wavelets and the angularly adaptive results are compared to the uniform angle results of section 6.2. Finally, in section 6.4, the same test case is run with spatial adaptivity on a uniform $P0$ angular discretisation. The results are then compared to the fixed mesh results of section 6.2 and a high resolution benchmark obtained with SWAN. Thus, this chapter tests the overall ability of Fluidity-SW to be applied on realistic scenarios, with uniform as well as adaptive spatial and angular meshes.

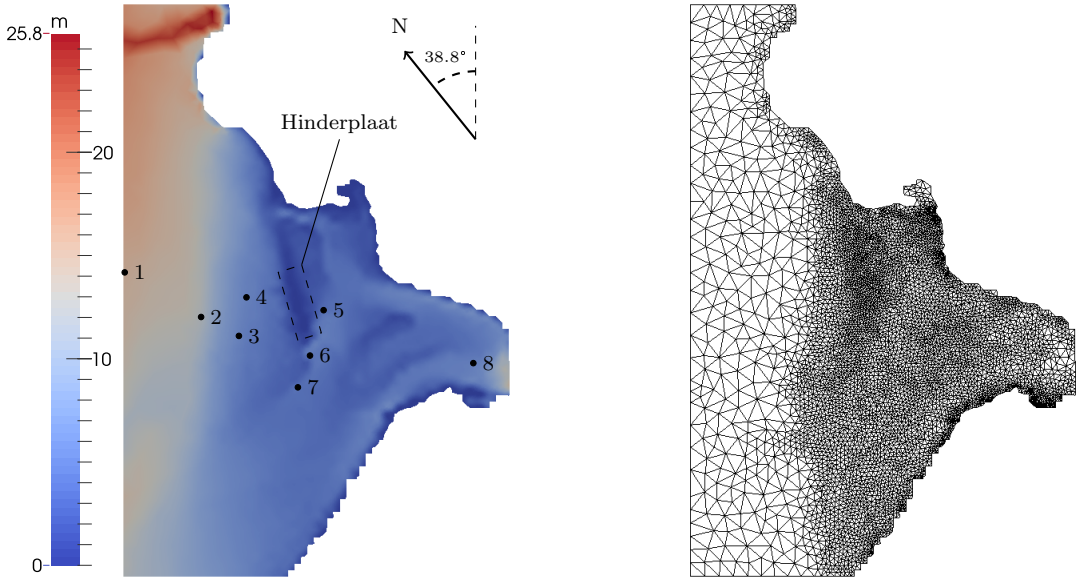
6.2 Haringvliet estuary

6.2.1 Model set-up

The Haringvliet estuary is part of the Rhine estuary in the southwest of the Netherlands. During a period of three months in 1982 the Ministry of Transport, Public Works and Water Management in the Netherlands conducted a wave measurement campaign for the validation of numerical wave models. From this extensive data set a local storm, which took place between October 14 and October 15, has been isolated [4] and is often used for the verification of spectral wave models in shallow water [72, 99, 73, 77].

The bathymetry for the Haringlviet test case, taken from the files for the Haringvliet case in the SWAN web-page [82], is presented in figure 6.1a. The surface area is approximately 15 km by 20 km in the $x-$ and $y-$ direction respectively, with the axis of the problem rotated by 38.8° relative to the North (see figure 6.1a). The area is characterised by relatively shallow waters, with a shoal (Hinderplaat) which encompasses almost half of the entrance to the estuary.

During the measurement campaign wave measurements were taken at eight locations (depicted in figure 6.1a), as well as measurements of wind directions, wind speeds and water levels. From the two days of the data set two test cases are considered here. These were on October 14 at 21:00 and 23:00 UTC respectively. These events are characterised by fairly constant wind speed and direction, relatively big waves



(a) Depth **(b)** Spatial mesh

Figure 6.1: Bathymetry and spatial mesh for the Haringvliet estuary, along with the locations of the eight observation stations and the location of the Hinderplaat shoal (taken from the SWAN website [82]). The positive $y-$ axis is rotated by 38.8° relative to the North.

Case	Time (UTC)	Water level (m)	Wind velocity ($\mathrm{m\,s^{-1}}$)	Wind direction (°)
I	21:00	0.3	12	300
II	23:00	1.7	14	300

Table 6.1: Description of the conditions for the two test cases considered for the Haringvliet estuary. The wind direction assumes a nautical convention, i.e. the direction from which the wind is blowing is measured clock-wise from North.

and low enough water levels to cause the creation of secondary peaks in the wave spectra [72].

The main conditions for two test cases are presented in table 6.1. The basic difference between the two events is in the water level which is equal to 0.3 m for test case I and 1.7 m for test case II (the change in the water level is implemented by increasing the value of the bathymetry throughout the domain). This allows for the investigation of the code in a range of shallow water depths. The wind speeds are $12\,\mathrm{m\,s^{-1}}$ and $14\,\mathrm{m\,s^{-1}}$ respectively and the wind direction is 300° for both cases. This direction assumes a nautical convention, i.e. the direction from which the wind is blowing is measured clock-wise from North. Given that the axis of the simulation is tilted by 38.8° the wind direction in Cartesian coordinates for the simulation, i.e. the direction in which the wind is blowing measured counter-clock wise from the positive $x-$axis, is 8.8°.

The one-dimensional measured spectra for location 1 (taken from [4]) are used as a boundary condition for the left boundary of figure 6.1a. The spectrum is distributed in angle with a $\cos^2(\theta)$ distribution and a mean direction of 10°. The wind speed is considered constant throughout the domain and currents are not taken into account. The simulations are run as stationary problems, starting from a zero initial guess, with all the source terms activated, i.e wind input, white-capping, four-wave interactions, three-wave interactions and depth-induced wave breaking. All the source terms are used with the default parameters (see section 2.4) and for the three-wave interactions a proportionality coefficient of $\alpha_{\mathrm{EB}} = 0.25$ is used.

The angular domain is discretised with a $P0$ angular discretisation and 32 angular elements (resulting in $\Delta\theta = 11.25°$). The frequency mesh has 32 elements logarithmically distributed from 0.0521 Hz to 1 Hz (resulting in $\Delta\sigma/\sigma = 0.1$). Finally the spatial mesh, taken from the files for the Haringvliet case in the SWAN web-page [82], has 11,489 elements (figure 6.1b) with a variable element edge length of $\Delta x \approx$ 25 m to 700 m.

In both test cases the results of Fluidity-SW are compared to the results obtained with SWAN on the same spatial mesh and the buoy measurements. With the default break-off criteria, SWAN converges the non-linear problem in 30 iterations. Here, however, a fixed number of 60 iterations is used for both codes, after which there is no visible change to the output spectra.

6.2.2 Results

The variance density spectra for the eight locations of figure 6.1a, are presented in figure 6.2 for test case I. In the locations where the wave measurements are not available at 21:00 UTC, the two closest observations around 21:00 UTC are presented.

First it is worth noting the scale of the transformation of the measured spectra (observations) from deep water to the entrance of the estuary. The variance density starts in location 1 at approximately $16\,m^2\,Hz^{-1}$ at the peak frequency and drops to about $0.1 - 0.15\,m^2\,Hz^{-1}$ just after the shoal (location 5). Then, far behind the shoal (location 8) the waves are regenerated by the local wind and increase to approximately $0.3\,m^2\,Hz^{-1}$ at the peak frequency. Location 7 is below the shoal and, thus, higher waves are registered with a variance density of approximately $1 - 1.5\,m^2\,Hz^{-1}$. This transformation is also observable in the value of the peak frequencies. In the shallow water region behind the shoal, local wind and three-wave interactions feed energy into the high frequency part of the spectrum, causing the peak frequency to increase. The waves enter at a peak frequency of approximately 0.15 Hz at location 1, shift to a peak frequency of 0.5 Hz at location 5, whereas location 8 has two peaks with the peak frequency shifted at approximately 0.3 Hz.

Comparing the two codes, the two results are consistent. The most noticeable difference between them is at location 5 where SWAN predicts higher energy levels. Noting that location 5 has the lowest wave heights, SWAN at that location predicts a significant wave height of 0.56 m and the difference between the codes in the prediction of the significant wave height is approximately 0.12 m.

Finally, comparing the results with the measurements for test case I the codes are reasonably good at predicting the transformation of the shape of the spectrum from a single-peaked spectrum at location 1 to a two-peaked spectrum with a shifted peak frequency at location 8. Taking into account the scale of the transformation (the variance density drops by two orders of magnitude from location 1 to location 5) the trends of the measured spectra are predicted in the simulated results, with the variance dropping from locations 1 to location 5 and then regenerating in location 8. However, examining the individual spectra, the energy level is over-predicted in location 2 and under-predicted in location 3. This probably means that the dissipation mechanisms are not well represented in that region. Similar conclusions can be drawn for locations 5 and 6 with an under and over estimation of the energy level,

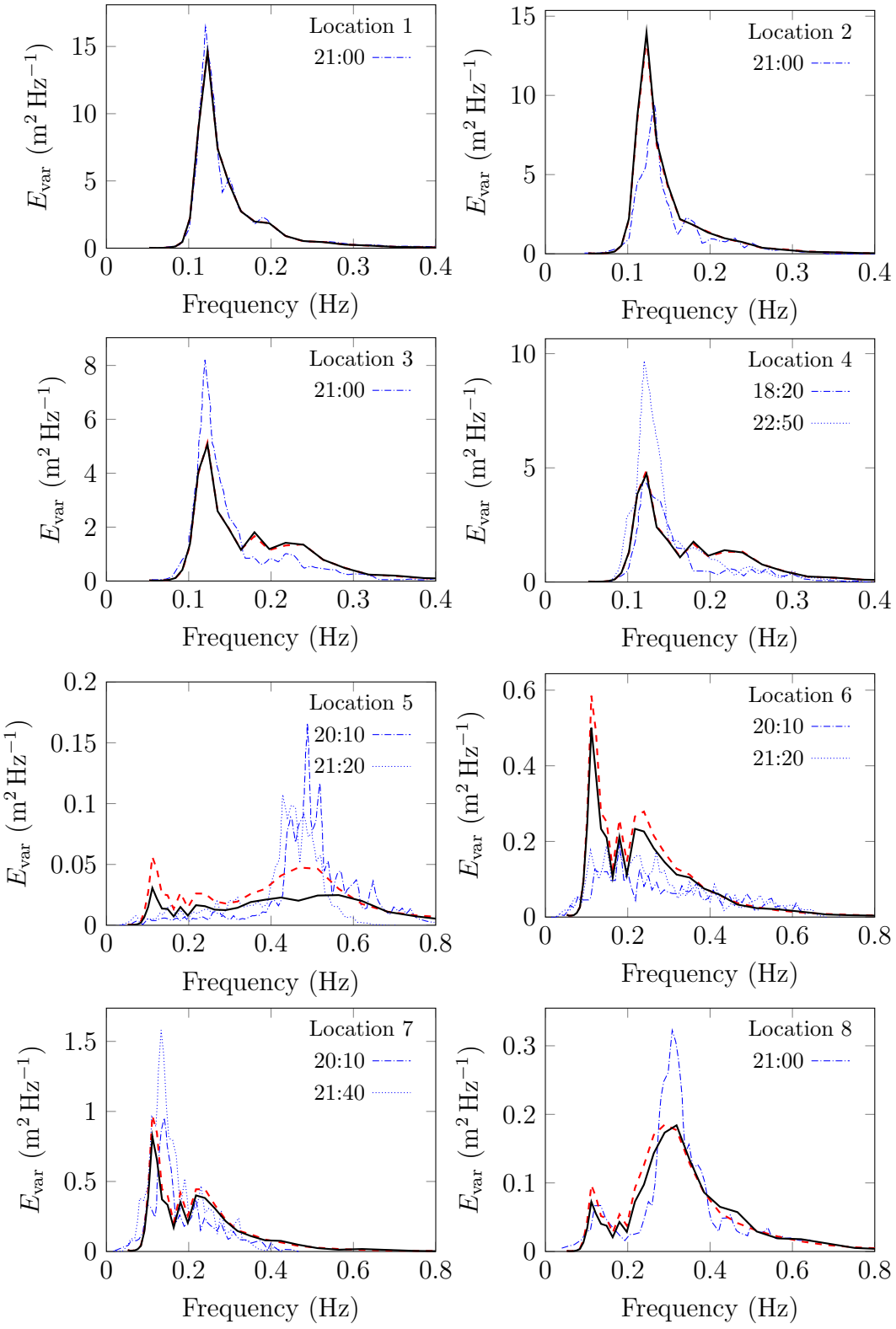


Figure 6.2: Variance density plots at the locations of figure 6.1a for the Haringvliet estuary at 14 October 1982, 21:00 UTC (test case I).
Fluidity-SW: ——, SWAN: - - -, observations: -·-· & ·····.

respectively. Finally, in location 8 the low-frequency peak is accurately predicted, but the high-frequency peak is under-estimated.

The ability of the codes to predict the sea state at the Haringvliet estuary is improved in test case II, where the water level is higher. The results for the eight locations are presented in figure 6.3. Location 2 is still over-predicted and location 3 under-predicted but the results are closer to the measurements. In location 8 there now seems to be too much energy at the high-frequency peak, compared to the measurements which show the primary peak at the low-frequency part of the spectrum. In general, however, considering the scale of the transformation the prediction of the sea state is reasonable, with the exception of location 2 where the over-estimation of the significant wave height is approximately 1 m.

Finally, comparing the two codes, the results are again consistent. The most noticeable difference occurs again in location 5 where SWAN predicts a significant wave height of approximately 1 m and the difference between the two codes is approximately 0.1 m.

It is beyond the scope of this work to further explore the discrepancies between the measurements and the numerical results. It is worth drawing a few conclusions however. As a first note, in the simulations above bottom friction is not included. To explore the impact of bottom friction, SWAN was run with the source term activated (with the default parameters, see [83]), resulting in higher dissipation at most of the locations. However, the impact was not very large and did not alter the main observations of the previous paragraphs. In location 2 for instance, where there is a clear overestimation of the significant wave height, activating bottom friction for test case II resulted in a reduction of the significant wave height by approximately 0.08 m, when the difference with the measurements is close to 1 m.

Secondly, comparing the two test cases the models produced results with a better match to the measurements when the water level was higher. This is an indication that in very shallow water the highly non-linear sea state is not adequately represented by the implemented source terms.

Finally, even though the results of the two codes were consistent there were small differences, most visible at location 5. The models have identical formulations for the source terms and these differences originate from the different spatial discretisations of the two codes. They are most visible in location 5 which is in the area of the highest gradients in the bathymetry and, thus, the solution fields. This is further

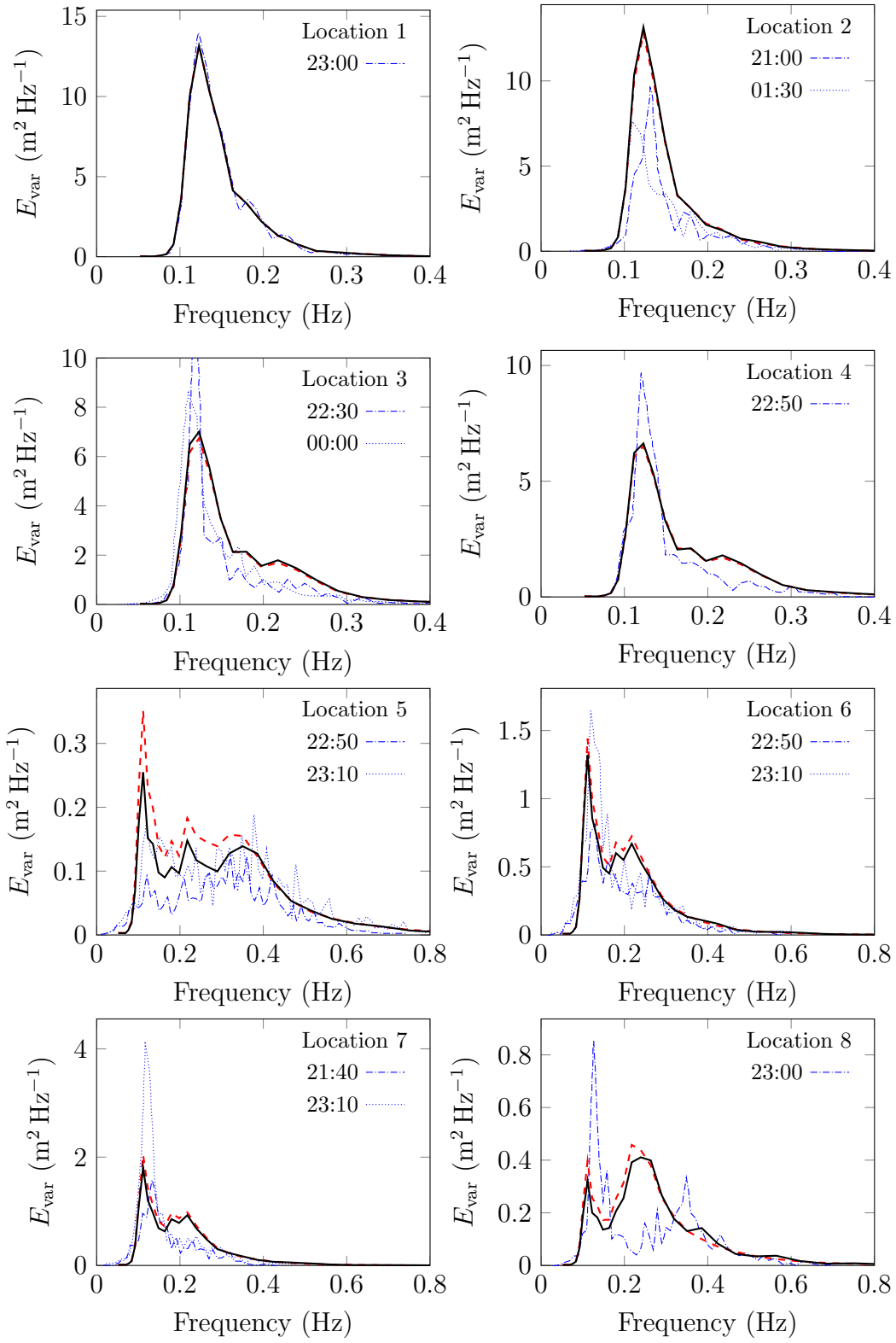


Figure 6.3: Variance density plots at the locations of figure 6.1a for the Haringvliet estuary at 14 October 1982, 23:00 UTC (test case II).
Fluidity-SW: ——, SWAN: - - -, observations: -·-· & ·····.

explored in section 6.4.

6.3 Haringvliet estuary – Angular adaptivity

6.3.1 Motivation and model set-up

In chapter 3 the proposed system was discretised with an arbitrary angular expansion. Then in chapter 5, this was used as the basis for expanding the angular dimension with Haar wavelets, which allowed for the developement of a simple angularly adaptive scheme based on thresholding the angular coefficients of the wavelet expansion. To formulate the system with Haar wavelets a mapping operator was used to map from a $P0$ space to Haar space. This was justified by the fact that using the mapping on each of the angular matrices (3.22) – (3.32) allowed the existing framework to be used with little modification to the code.

When implementing Haar wavelets with the source terms, however, the utility of the mapping becomes even more evident. The DIA is by far the most successful approximation of non-linear wave-wave interactions (see section 2.4.3), mostly due to to the lack of success in finding efficient more accurate replacements for operational wave models [88]. The DIA, however, assumes discrete angles interacting with each other at predetermined intervals. By being able to map from $P0$ space to Haar space the implementation of the DIA in Haar space becomes trivial.

In this section the Haringvliet test case is used again, but now the simulation is run with angular adaptivity activated. Given that refraction is not very important here (as is typical of short crested waves in small coastal regions [72]), increasing the number of angles, compared to the simulations in the previous section, does not have a major impact on the results. The maximum number of angles is therefore set equal to 32, the same number of angles used for the uniform angle results of the previous section. Thus, adaptivity is tested for its ability to reproduce the same results with fewer degrees of freedom.

Considering the main findings of chapter 5, it should be noted that the Haringvliet estuary is not the ideal test case for angular adaptivity. The domain is small and the simulation stationary, which means that there won't be a big enough variation in the angular distribution of action density, in space or time, to showcase the advantages of anisotropic angular expansions. Also, the simulation mainly involves short crested

waves which are adequately modelled with a small number of angles. However, the relative reduction of degrees of freedom with adaptivity increases with the maximum number of angles.

Thus, angular adaptivity would be better suited for larger scale time-dependent simulations, where spatial advection and angular advection (refraction) are important. However, the main objective here is to verify that angular adaptivity can be successfully used in scenarios were the source terms dominate the system. Angular adaptivity on advection dominated problems has already been verified in chapter 5. Thus, verifying that source terms can be properly accounted for, allows for the application of angular adaptivity in random sea-states where short and long crested waves, as well as advection and source dominated regions are part of the same simulation.

For the verification of adaptivity, an adaptive $HW_{l,j_{\max}}$ discretisation is used on the Haringvliet estuary, where the scaling functions and initial levels are $j_{\text{init}} = l = 2$ and the maximum level is $j_{\max} = 5$. This means that the simulation starts with $2^2 = 4$ angular basis functions and is allowed to reach a maximum of $2^5 = 32$. Again 60 iterations are used to converge the non-linear problem and adaptivity is activated after each iteration step. Finally two different tolerance levels are tested, $\tau = 10^{-2}$ and $\tau = 10^{-3}$. Given that test case II had a better agreement with the measurements, only this scenario is considered here.

6.3.2 Results

The mean number of angular basis functions at each iteration step for an adaptive $HW_{2,5}$ discretisation with a tolerance of $\tau = 10^{-2}$ is presented in figure 6.4, while figure 6.5 presents the angular mesh at various iteration steps.

The simulation starts with four angular basis functions on each node. For the first few iterations adaptivity rapidly increases the number of basis functions throughout the domain, bringing the mean number of angles to approximately 16 after the 15th iteration (figure 6.4). Then the mean number of angles slightly drops to approximately 15 by the 25th iteration and stays constant for the remaining iterations.

It is interesting to note that adaptivity starts by introducing most of the angles in the area before the shoal and as the iterations progress, gradually increases the number of angles after the shoal (figure 6.5). In the first few iterations the negative source

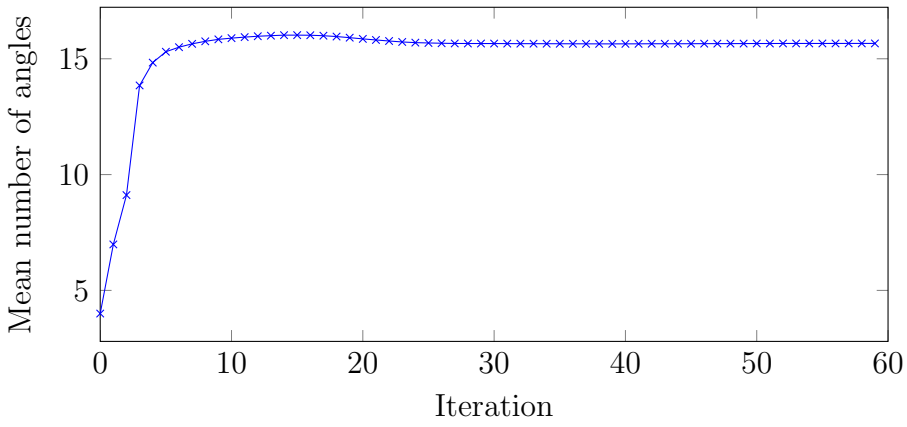
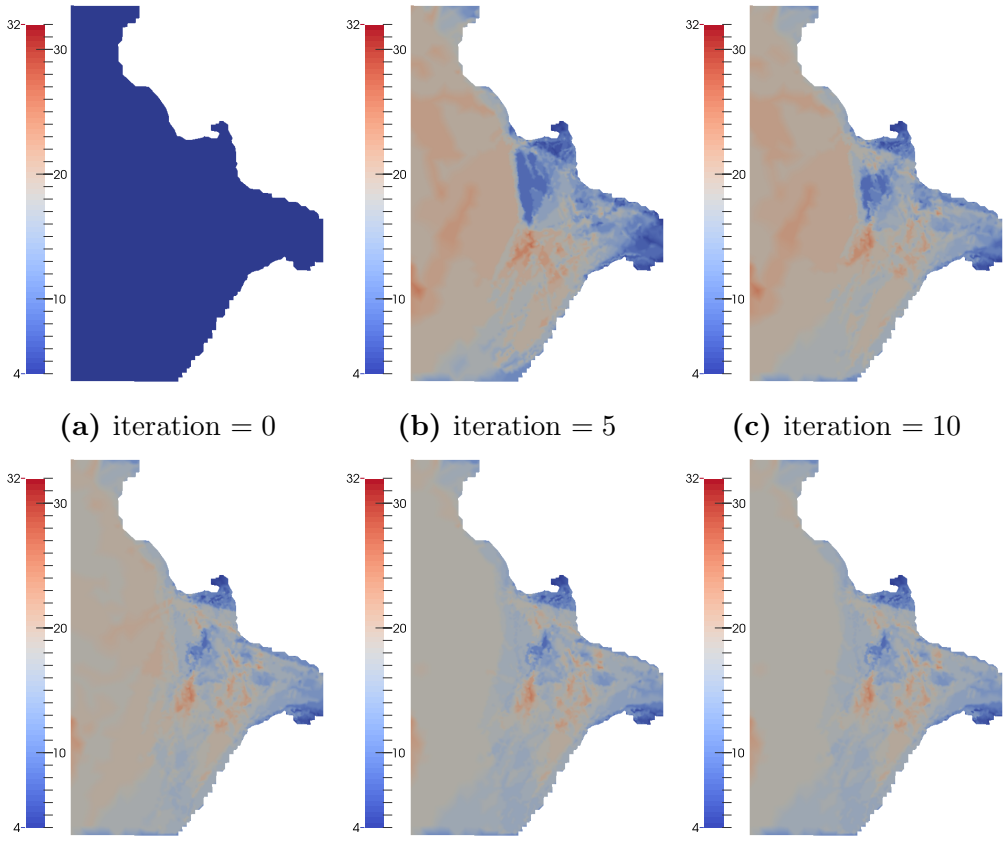


Figure 6.4: Mean number of angular basis functions, for an adaptive $HW_{2,5}$ discretisation with tolerance $\tau = 10^{-2}$ at each iteration step, for the Haringvliet test case.



(a) iteration = 0 **(b)** iteration = 5 **(c)** iteration = 10

(d) iteration = 20 **(e)** iteration = 40 **(f)** iteration = 60

Figure 6.5: Angular mesh, i.e. number of angular basis functions, for an adaptive $HW_{2,5}$ discretisation with tolerance $\tau = 10^{-2}$ at various iteration steps, for the Haringvliet test case.

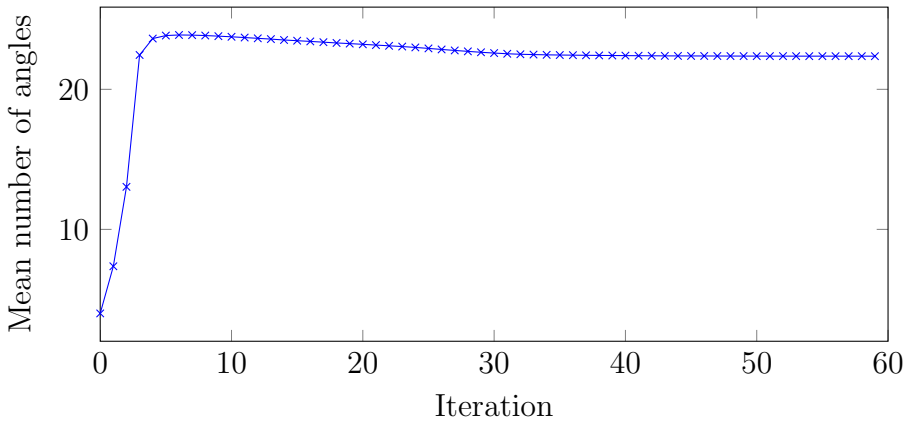


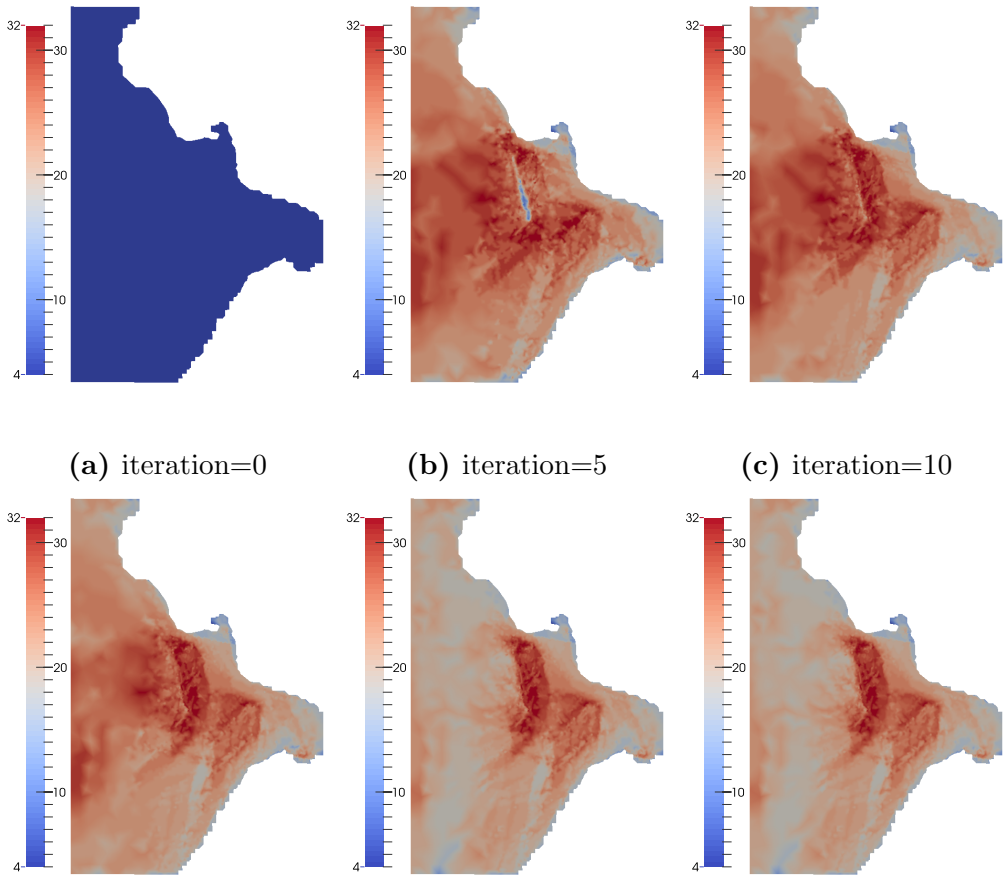
Figure 6.6: Mean number of angular basis functions, for an adaptive $HW_{2,5}$ discretisation with tolerance $\tau = 10^{-3}$ at each iteration step, for the Haringvliet test case.

terms start dissipating the wave energy in the shallow water areas, i.e. around the shoal. As the non-linear problem evolves, however, the positive source terms start regenerating the waves in that area, gradually increasing the energy content behind the shoal (mostly feeding energy to the high frequency part of the spectrum). Given that some of the nodes in that area have more than half of the maximum number of angles (see figure 6.5), this also means that the directional distribution in that area gets wider, probably due to refraction and four-wave interactions shifting energy in the angular dimension.

As the angular coefficients get bigger, adaptivity increases the number of angular basis functions. After the non-linear problem has converged (as mentioned in section 6.2, SWAN with the default break-off criteria converged with approximately 30 iterations) and only small variations to the action density occur, adaptivity stops changing the angular mesh.

The same results for a tolerance of $\tau = 10^{-3}$ are presented in figures 6.6 and 6.7. By using a smaller tolerance adaptivity introduces more angles throughout the domain and, thus, the mean number of angles increases compared to $\tau = 10^{-2}$. In particular, in the first few iterations the mean number of angles jumps to approximately 24 from the initial value of 4 (figure 6.6). Then until the 30th iteration that number drops to approximately 22 and stays constant for the last 30 iterations.

Once more, in the first few iterations most of the angles are concentrated in the area before the shoal, but as the non-linear problem evolves the majority of the angles



(a) iteration=0 **(b)** iteration=5 **(c)** iteration=10

(d) iteration=20 **(e)** iteration=40 **(f)** iteration=60

Figure 6.7: Angular mesh, i.e. number of angular basis functions, for an adaptive $HW_{2,5}$ discretisation with tolerance $\tau = 10^{-3}$ at various iteration steps, for the Haringvliet test case.

is placed in the area after the shoal (figure 6.7). The main difference now is in the amount of angles inserted, with the majority of the nodes in the area behind the shoal having the maximum number of angles activated.

It should be noted that the area behind the shoal has the lowest values of action density and, thus, significant wave heights. However, it has the widest angular distributions. This is why decreasing the tolerance has such a big impact on the angular mesh. As the tolerance level is decreased from $\tau = 10^{-2}$ to $\tau = 10^{-3}$, more resolution is inserted to represent the wide distribution of small angular coefficients.

To quantify the ability of angular adaptivity to reproduce the uniform resolution results, figure 6.8 presents the variance density spectra for the eight measurement locations, for both tolerances. For locations $1-4$ and $6-7$ both adaptive simulations reproduce essentially the same results predicted by a uniform angular resolution. For location 5, on the other hand, using a tolerance of $\tau = 10^{-2}$ underestimates the variance density, whereas it overestimates it for location 8. Decreasing the value of the tolerance, however, pushes the results very close to the ones predicted by a uniform resolution, for both locations.

To interpret these results the scale of the variance density plots should be considered. The two locations where adaptivity under-performed, compared to a uniform angular resolution, have the smallest energy content. The calculated significant wave height for location 5 with a uniform resolution is 0.907 m, whereas adaptivity with $\tau = 10^{-2}$ and $\tau = 10^{-3}$ calculated 0.798 m and 0.872 m, respectively. The equivalent values at location 8 are 1.15 m for the uniform mesh and 1.22 m and 1.19 m for the two adaptive runs, respectively. Thus, running the Haringvliet problem with $\tau = 10^{-2}$ underestimates the significant wave height for location 5 by 12% and overestimates it for location 8 by 6 %. However, it only uses half of the angular degrees of freedom. Equivalently decreasing the tolerance reduces these values to about 3% for both locations, but now approximately 70% of the angles are used. Further decreasing the tolerance introduces more angles, resolving better the areas with small angular coefficients and pushing the results closer to the uniform resolution. A balance between accuracy and resolution is what defines the desired tolerance level.

For each node of the domain a different angular discretisation is created to represent the angular distribution of the action density. This is further illustrated in figure 6.9, which presents the polar plots for the eight locations, for a tolerance of $\tau = 10^{-3}$. Locations $1-4$ are before the shoal and mainly need angular coefficients in half of

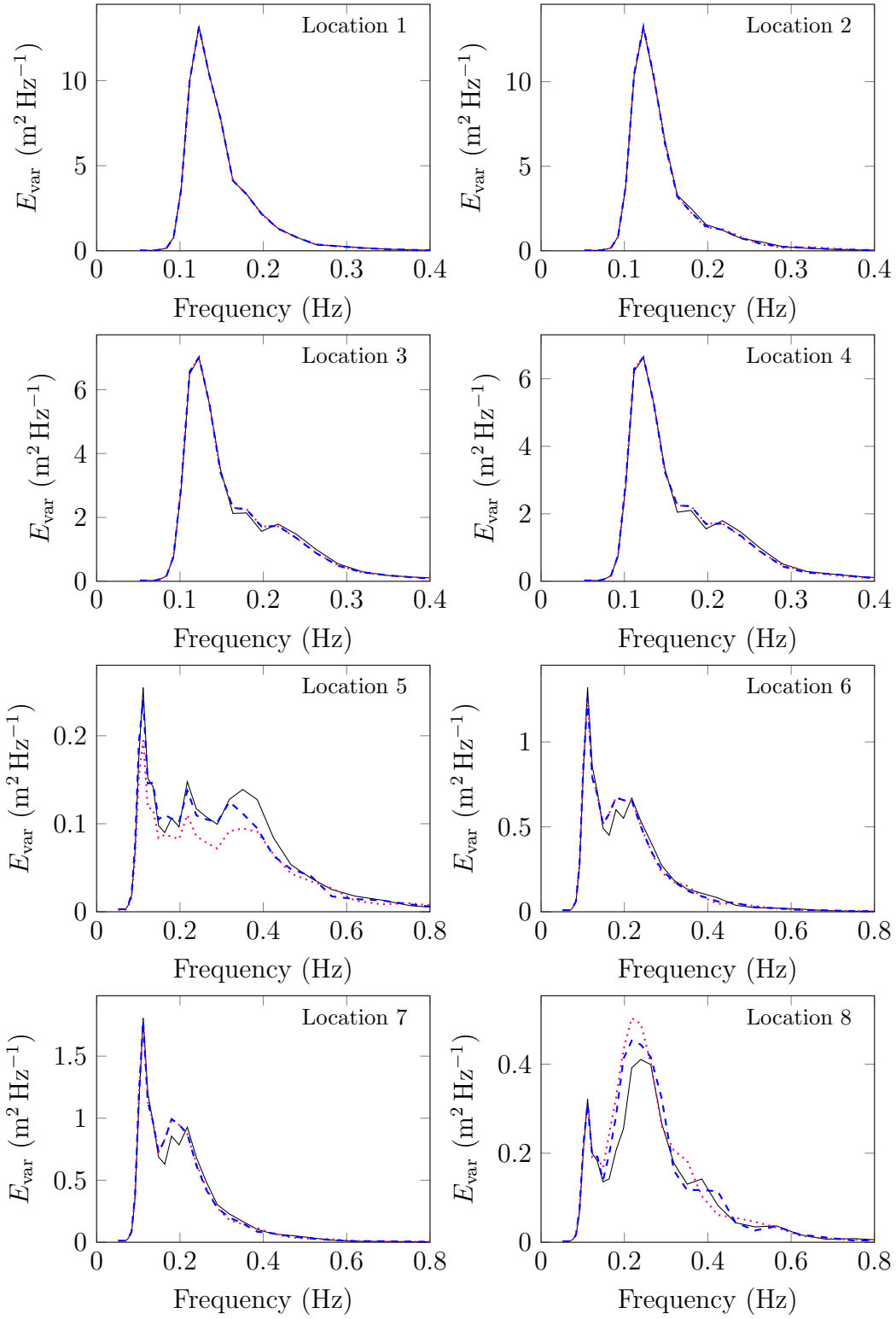
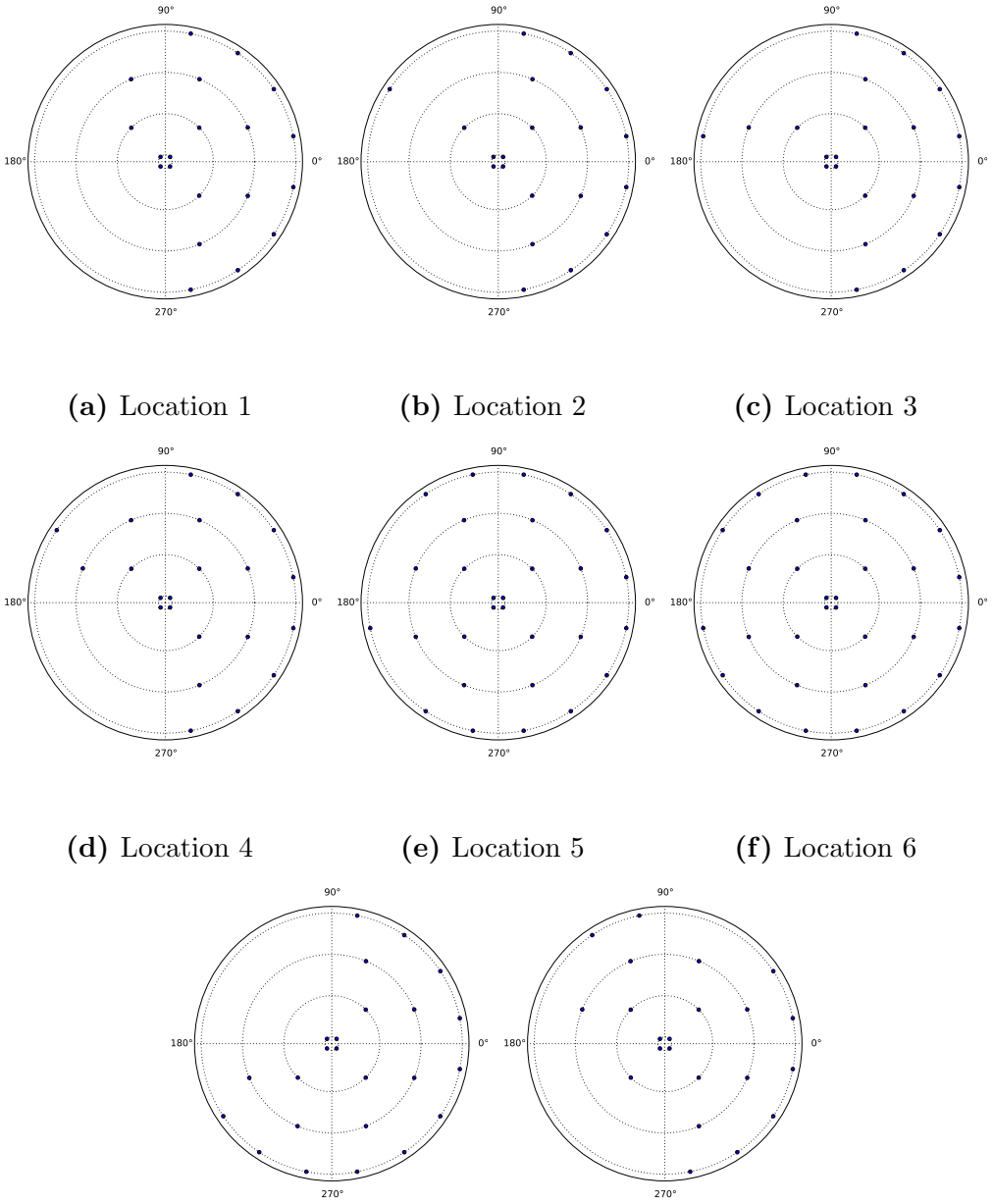


Figure 6.8: Variance density plots at the locations of figure 6.1a for the Haringvliet estuary (test case II). An adaptive $HW_{2,5}$ discretisation with tolerances $\tau = 10^{-2}$ and 10^{-3} compared against the uniform $P0$ results with 32 angles. $P0 - 32$: ——, $HW_{2,5}$ with $\tau = 10^{-2}$: ·····, $HW_{2,5}$ with $\tau = 10^{-3}$: - - -.



(a) Location 1 **(b)** Location 2 **(c)** Location 3

(d) Location 4 **(e)** Location 5 **(f)** Location 6

(g) Location 7 **(h)** Location 8

Figure 6.9: Polar plots for an adaptive $HW_{2,5}$ discretisation with tolerance $\tau = 10^{-2}$, for the Haringvliet test case. The locations are depicted in figure 6.1a.

the angular domain to advect the solution in geographic space. At the rest of the locations however, refraction, four-wave interactions and the local wind widen the angular distribution and adaptivity increases the number of angular coefficients.

Thus, the proposed scheme successfully reproduces the results of the equivalent uniform resolution and does so at a reduced cost. The source terms are accurately represented with the adapted angular mesh and the non-linear problem converges to the solution of the uniform angular mesh with decreasing thresholding tolerances.

6.4 Haringvliet estuary – Spatial adaptivity

6.4.1 Motivation and model set-up

The focus in this section is on the application of dynamic spatial mesh optimisation with the proposed scheme. Spatial mesh optimisation is used to accurately represent multi-scale, evolving physical processes by dynamically identifying and resolving the anisotropy in the solution fields.

To implement spatial mesh optimisation, the infrastructure of the Fluidity framework is utilised. Mesh optimisation in Fluidity is driven by interpolation error-based measures. The main process is based on the construction of a metric tensor field, calculated from the Hessian of the solution fields, user-defined error bounds, and maximum and minimum allowed edge lengths. A functional describing the mesh quality is then formed, whose minimisation ensures the creation of a mesh with elements that have the appropriate shape and size. This is achieved through an optimisation algorithm with heuristic topological operations that change the local connectivity of the nodes (a type of so-called h-adaptivity). This results in a mesh that is refined in regions where high curvature of the solution field exists, but also coarsened in areas where resolution is not required. Thus, it provides an effective framework for refining the areas of interest while keeping the computational cost low. For a more detailed description of the adaptive algorithm and the general framework the reader can refer to [61] and [67] respectively, while an in-depth description of the various options in Fluidity can be found in [44].

Here, the Haringvliet test case is used again and only test case II is considered. First the simulation is run with SWAN on a very fine mesh to provide a benchmark for the spatially converged solution. A grid is constructed with a constant element-edge

length of $\Delta x \approx 5\,\text{m}$ (for comparison the mesh used for the simulations in sections 6.2 and 6.3 had a minimum edge-length of 25 m and a maximum of 700 m). This results in a mesh with $\approx$ 24,000,000 elements.

Then Fluidity-SW is set up with spatial adaptivity (on a fixed angular mesh), using the significant wave height for the calculation of the error metric. An absolute measure is chosen for the optimisation, based on the infinity norm of the interpolation error. A constant error bound is chosen, equal to 0.035, which is approximately 1% of the maximum value of the significant wave height in the test case. The minimum edge length is set equal to 0.1 m and the maximum 5,000 m, while the maximum number of nodes equal to 100,000. Once more, a fixed number of 60 non-linear iterations are used to converge the stationary problem and spatial adaptivity is activated every 5 iterations.

6.4.2 Results

The results of the SWAN simulation on the fine grid (SWAN-fine) along with the results for SWAN and Fluidity-SW on the fixed coarse mesh of section 6.2 (repeated from section 6.2 as SWAN-coarse and Fluidity-SW-coarse), are presented in figure 6.10. Here only location 5 is presented, as this was the location with the biggest differences between the two codes.

Comparing the SWAN-fine results with the coarse mesh results of section 6.2, it seems that both SWAN-coarse and Fluidity-SW-coarse were not converged. However, SWAN-coarse appears to be marginally closer to the fine benchmark. The significant wave height predicted for location 5 by SWAN-coarse was 1.007 m and by Fluidity-SW-coarse 0.907 m. The equivalent value for SWAN-fine is 0.969 m.

This seems counter-intuitive, given that SWAN has first-order accuracy compared to the second order of the $P1$ sub-grid scale method and in chapter 4 the proposed scheme outperformed SWAN on most of the problems. A possible explanation however, is that SWAN on unstructured grids is monotone [99] (i.e. the value of the action density is guaranteed to be positive), whereas the proposed numerical scheme is not. Thus, in smooth problems, such as the ones presented in chapter 4, the proposed scheme converges faster, however, in the presence of strong gradients the results can oscillate, affecting the accuracy of the solution. This then gets augmented by the removal of the negative values and the rescaling of the spectrum (see section

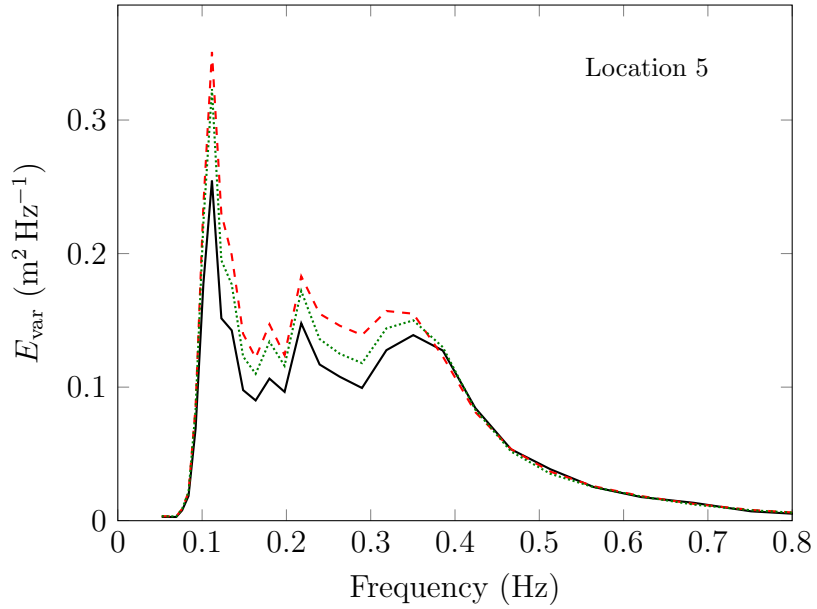


Figure 6.10: Variance density plots at location 5 of figure 6.1a, for the Haringvliet estuary (test case II). The results from a finely resolved grid with SWAN, compared to the coarse results of section 6.2.
Fluidity-SW-coarse: ——, SWAN-coarse: - - -, SWAN-fine: ·····.

3.6). The differences between the two codes are, thus, more apparent in location 5, which is in the area with the highest gradients of the solution fields. It is worth noting that similar observations were made by Zanke et al. [89] when comparing a non-monotone Crank-Nicolson Taylor Galerkin scheme with a monotone Residual Distribution scheme.

Spatial adaptivity is now activated in an effort to construct a mesh which better represents the gradients in the solution fields without increasing the computational cost, compared to the fixed coarse mesh of section 6.2 which had 11,489 elements. Here, for the adaptive run, the simulation starts with a very coarse geometry-conforming mesh, allowing adaptivity to gradually refine it as the non-linear problem evolves. Figure 6.11 presents the number of spatial elements after each non-linear iteration and figure 6.12 presents the spatial mesh at various iteration steps.

The adaptive simulation starts with 1,094 elements. Each time adaptivity is evoked (every 5 iterations) the number of elements increases, with resolution focusing on the areas that have a big curvature in the significant wave height. The result is a high number of elements for the Hinderplaat shoal as well as a few areas close to the edges of the domain, while the rest of the domain remains relativity coarse.

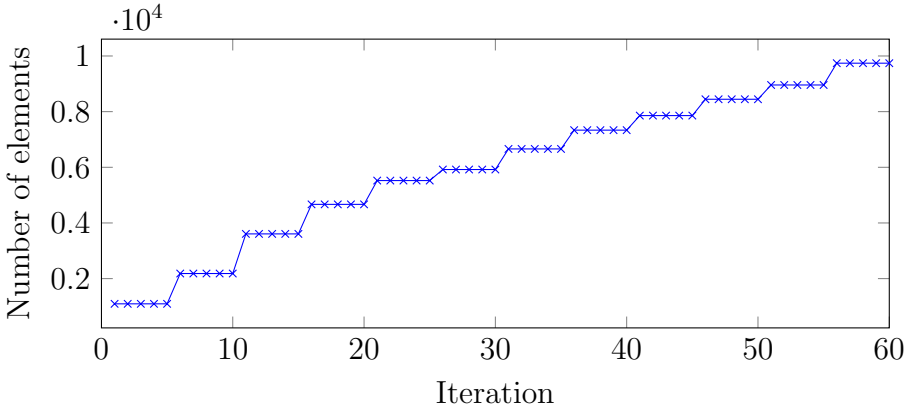
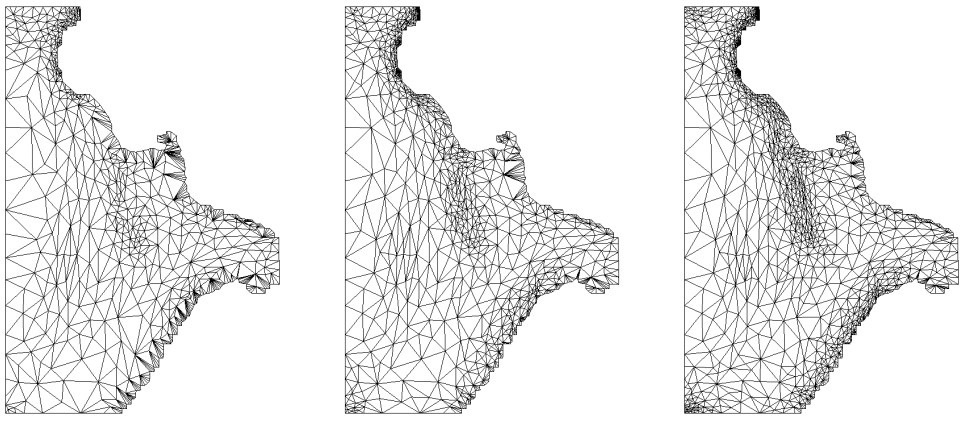
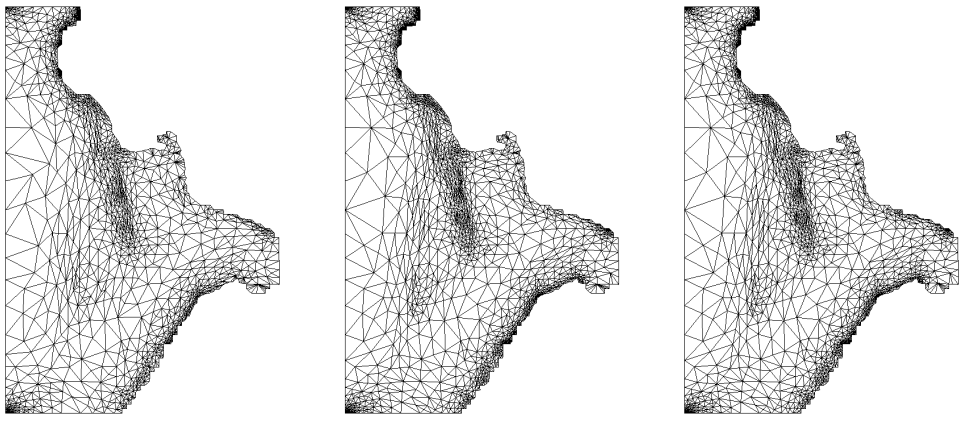


Figure 6.11: Spatial adaptivity for the Haringvliet test case with Fluidity-SW. Number of spatial elements at each non-linear iteration.



(a) iteration=0 **(b)** iteration=5 **(c)** iteration=10



(d) iteration=20 **(e)** iteration=40 **(f)** iteration=60

Figure 6.12: Spatial adaptivity for the Haringvliet test case with Fluidity-SW. Spatial mesh at various iteration steps.

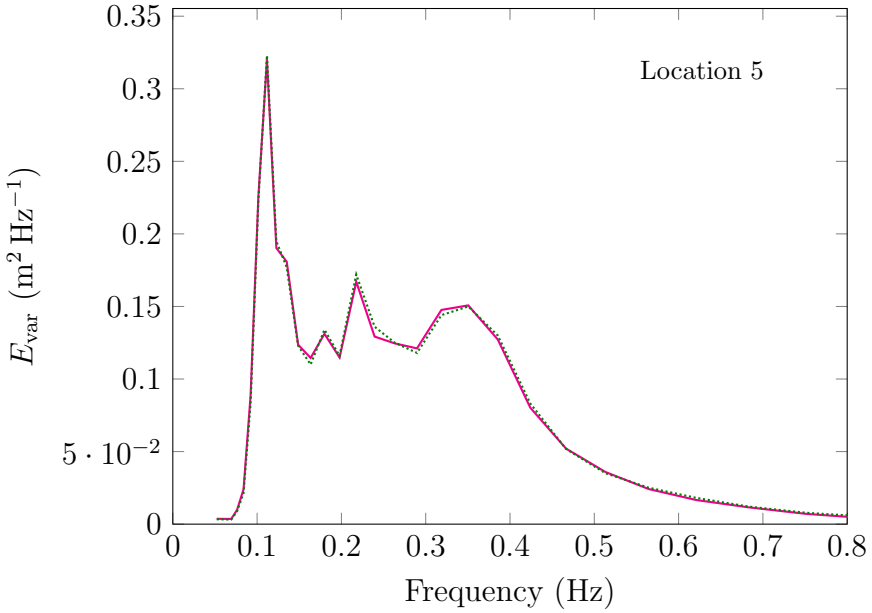


Figure 6.13: Variance density plots at location 5 of figure 6.1a, for the Haringvliet estuary (test case II). The results from a finely resolved grid with SWAN, compared to the results from spatial adaptivity with Fluidity-SW.
Fluidity-SW with spatial adaptivity: ——, SWAN-fine: ·····.

After 60 iterations the mesh has 9,741 elements, which is almost 2,000 elements less, compared to the coarse mesh of section 6.2.

To quantify the quality of the adapted mesh, figure 6.13 now shows the comparison of the SWAN-fine results against the spatially adaptive results with Fluidity-SW, for location 5. The adaptive results are now predicting a spectrum very close to the fine benchmark, with a difference in the significant wave height of less than 1% (for comparison, with the coarse fixed mesh the respective difference was 4% for SWAN-coarse and 6% for Fluidity-SW-coarse).

Thus, the spatially adaptive results more accurately predict the transformation of the spectrum in the Haringvliet test-case, with a lower cost compared to the results obtained with the fixed coarse mesh. The final adapted mesh has a small number of elements optimally placed to represent the gradients in the solution fields. At the same time however, the simulation starts with a very coarse geometry-conforming mesh which is gradually refined as the non-linear problem evolves and the adaptive algorithm is evoked. This means, that the cumulative degrees of freedom and, thus, the computational cost throughout the 60 iterations is significantly smaller.

6.5 Conclusions

In this chapter the overall ability of Fluidity-SW to be used in realistic simulations was successfully verified, on fixed and adaptive spatial and angular meshes.

First, the code (with a fixed spatial and angular mesh) was tested on the Haringvliet estuary, a realistic shallow water test case, with all the source terms activated. Comparing with the results obtained with SWAN, on the same mesh and with the same set-up, the two codes were consistent in the prediction of the variance density spectrum, with only small differences attributed to the different spatial discretisations.

Compared to the observations, both codes did a good job at predicting the trends, as well as the scale of the transformation of the measured spectra, as the waves propagated from deep to shallow water. However, when examining the individual spectra at various locations, there were noticeable differences between the observations and the predictions. In general, the results were a better match to the observations in the scenario with higher water levels. This suggests that in very shallow water the implemented source terms are not adequately representing the highly non-linear physical processes of the waves.

It was then shown that angular adaptivity (with a fixed spatial mesh) can successfully reproduce the results derived from a uniform angular resolution, by using fewer degrees of freedom. In particular, the biggest difference between adaptive and uniform simulations was at the location with the lowest energy level (behind the shoal). For a tolerance of $\tau = 10^{-2}$, adaptivity overestimated the significant wave height by 12% at that location, but used approximately half of the degrees of freedom compared to the uniform simulation. Decreasing the tolerance to $\tau = 10^{-3}$ reduced this difference to 3%, but increased the required mean number of angles to approximately 70%. Thus, it was again shown that a balance between accuracy and computational cost can be achieved by calibrating the thresholding tolerance.

It is worth noting that the Haringvliet test case is not an ideal framework for applying angular adaptivity. It is a small stationary simulation with short-crested waves which are adequately resolved with a small number of angles. A big part of the domain has a wide angular distribution and there is no substantial variability in the angular distribution of the action density throughout the domain. However, having already shown in chapter 5 that adaptivity is very well suited for advection

dominated problems, the main objective here was to show that the source terms can be successfully represented. This then allows for the use of adaptivity in random sea-states. In large-scale, transient simulations where spatial and angular advection are important the relative reduction in the degrees of freedom will be significantly bigger.

Finally, preliminary results from the application of spatial adaptivity (with a fixed angular mesh) were presented. The simulations started with a very coarse geometry-conforming mesh, which was gradually refined, using the significant wave height for the calculation of the error metric. This resulted in a mesh with a small number of elements, appropriately placed to account for the gradients in the solution field. The results from the adaptive mesh and the fixed mesh (used to initially verify the code) were then compared to a high resolution benchmark. It was shown that adaptivity can produce a better match to the benchmark, by creating a mesh with fewer elements. In fact, given that the simulations started with a very coarse mesh and the number of elements was gradually increased, the cumulative computational cost of the simulation was significantly smaller, compared to using a fixed mesh.

Similar to angular adaptivity, the advantages of spatial adaptivity would be considerably bigger in large-scale transient problems, with high variability in the temporal and spatial distribution of the solution fields. Further extending the framework of Fluidity-SW to allow for a combined space-angle adaptive mesh could then significantly reduce the computational costs associated with high-fidelity, multi-scale simulations.

Chapter

SEVEN

Conclusions and future work

With this work a new spectral wave model was developed, Fluidity-SW, presenting a new approach for the discretisation of the action balance equation, with a focus on the treatment of the angular and spatial dimensions. The resulting framework was extended with a new method for the application of dynamic anisotropic angular adaptivity, which can more efficiently resolve the angular variability of the solution fields. Finally, the code was further extended with the implementation of dynamic anisotropic spatial h-adaptivity, in an effort to more accurately deal with the spatial variability of the solution fields. Throughout this work, the proposed numerical scheme was thoroughly tested in a wide range of simulations, and its results were compared against analytical solutions, wave measurements and the results obtained with the unstructured mesh version of the widely used SWAN code.

For the angular discretisation a discontinuous finite element expansion was used. The spatial discretisation, on the other hand, was implemented with a sub-grid scale method, which attempts to combine the benefits of discontinuous Galerkin formulations, i.e. accuracy and stability, with continuous Galerkin formulations, i.e. low computational cost. The resulting framework, with a $P1$ spatial expansion (linear) and $P0$ angular expansion (piecewise constant), was validated against a set of standardised benchmarks, designed to test each of the terms of the equation by isolating the various physical processes. Then the code was verified on a realistic

simulation with all the source terms activated.

It was shown that the numerical scheme exhibits little numerical diffusion (in geographic space) and that the linear approximation in geographic space results in higher accuracy compared to the first-order unstructured mesh version of SWAN. However, contrary to SWAN on unstructured grids, the proposed numerical scheme leads to non-monotonic behaviour. This means that in the presence of unresolved strong gradients, oscillations can reduce the quality of the solution. This, of course, has to be weighted against the higher numerical diffusion of monotone first-order schemes, which becomes a significant disadvantage in larger-scale simulations. As an alternative high-order schemes can be used combined with non-linear flux limiters. These should be further explored in the future.

The angular dimension was then discretised with the use of Haar wavelets, which are hierarchical, compactly supported basis functions. This allowed for the development of a simple and efficient adaptive algorithm, based on thresholding the values of the angular coefficients of the wavelet expansion. The resulting adaptive framework introduced dynamic spatial and angular anisotropy in the angular mesh. Angular adaptivity was successfully verified on both advection-dominated (space and angle) problems and source-term-dominated problems. It was shown to be very effective in cases where the temporal and/or spatial and/or angular anisotropy of the solution fields are high. Realistic examples for such conditions are large-scale, transient, advection-dominated problems, such as swell propagation over long distances.

In general, random sea-states are characterised by both swell conditions and wind seas (short-crested waves), with swell propagation typically requiring finer angular resolutions compared to short-crested wind seas. At the same time waves are directional, with a mean direction that is subject to variable external forces. This means that in many cases a large number of angular degrees of freedom are not contributing to the solution, but at the same time an a-priori estimation of the ideal angular mesh would be challenging. Thus, the dynamic adjustment of the angular mesh provides a natural framework for the modelling of multi-scale, random sea-states. In fact it was shown that adaptivity can also be useful in the mitigation of the Garden Sprinkler Effect, by only locally increasing the angular degrees of freedom.

Finally, preliminary results from the application of spatial adaptivity were presented on a realistic scenario. Using the significant wave height as a basis for the construction of an error metric, a very coarse geometry-conforming mesh was gradually

refined by increasing the resolution in the areas of interest. This resulted in a mesh with a small number of elements, optimally placed to account for the anisotropy of the solution field. By comparing the adapted results and the results from a fixed mesh, against a high resolution benchmark it was shown that spatial adaptivity can provide a better match to the benchmark with a smaller number of elements, compared to the fixed mesh.

Thus, the overall ability of Fluidity-SW to simulate surface gravity wind-waves was successfully verified, on fixed spatial and angular meshes, as well as with spatial and angular adaptivity.

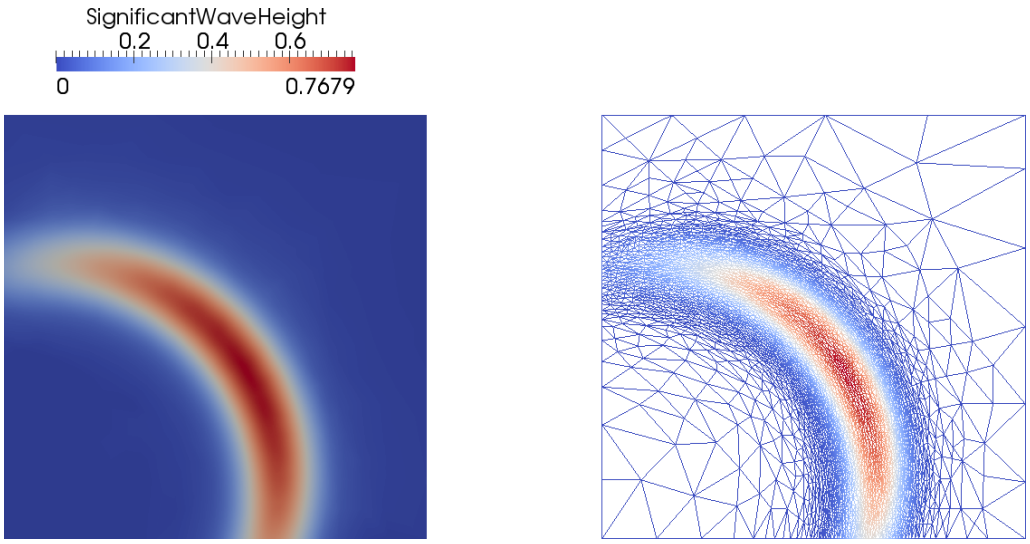
For future work, in the short-term effort should be concentrated in optimising the code. Besides the basic improvements aimed at speeding up its current implementation, this should also involve changes in the underlying framework.

Firstly, the sub-grid scale model needs to be further improved in order to be competitive against a purely discontinuous formulation. The first step towards this is the approximation of D (see section 3.6). Reducing the cost of its inversion, while maintaining a stable spatial discretisation is of the utmost importance, in order for the sub-grid scale method to prove efficient.

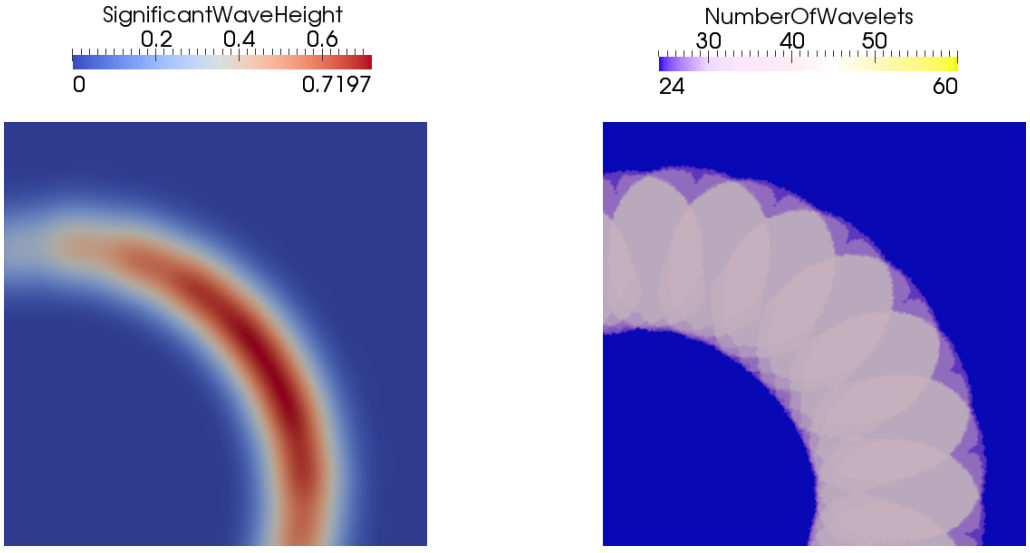
Furthermore, higher-order finite element spaces, in geographic and angle space, should be investigated for their potential benefits. Higher-order schemes should also be implemented for the up-winding in angle and frequency, while better alternatives should be investigated for the time propagation. Finally, the application of matrix-free solvers should be explored, as a means to remove the hindrance of calculating and storing large matrices, and improve the parallel capability of Fluidity-SW.

In all the adaptive results presented, the focus was on either spatial or angular adaptivity. In practice, however, an even more efficient framework would be a combined space-angle adaptive scheme. Figure 7.1 shows two simulations for an idealised example of wave energy propagating over a long distance. In the first simulation spatial adaptivity is used (figure 7.1a), while in the second angular adaptivity (figure 7.1b).

As the wave energy propagates, spatial and angular adaptivity are following the solution field, locally refining the spatial and angular mesh respectively. Thus, for each simulation an optimal mesh is constructed to represent the solution. Combining the two algorithms would then produce an optimal space-angle mesh, which would account for the errors in both spaces and help to further reduce the computational cost of the simulation. Thus, combined space-angle error metrics should be explored



(a) Significant wave height and spatial mesh.



(b) Significant wave height and angular mesh.

Figure 7.1: Example of an idealised test case, where a monochromatic wave propagates over a long distance. Two different simulations are presented, with the application of spatial and angular adaptivity respectively.

in the future.

A similar approach should also be considered for the frequency space. In this work the focus was on space and angle, however, it would be equally useful to apply frequency adaptivity or combined space-angle-frequency adaptivity. The main problem with this approach, is that the proposed implicit scheme solves the whole system at once. With the current implementation, a finite volume scheme in frequency allows each frequency group to be solved separately. Thus, the assembled system is of size (angular degrees of freedom)^2 $\times$ (spatial degrees of freedom)^2, for each frequency. Incorporating the frequencies into the finite element framework, developed for the angular dimension, would allow for frequency-adaptivity. However, the assembled system would now be (angular degrees of freedom)^2 $\times$ (spatial degrees of freedom)^2 $\times$ (frequency degrees of freedom)^2. This would significantly increase the memory and computation demands. However, utilising a matrix-free approach could alleviate this problem and allow for the incorporation of the frequency in the same scheme.

In the longer term, work should focus on extending the framework to further expand its capabilities. First, the code should be coupled to a circulation model for combined wave-current simulations. Then the source terms should be augmented, to account for recent improvements in their formulations, various processes that have not been already included (such as bottom friction and diffraction), as well as the ability to represent wave energy converters for applications in the design of wave energy arrays.

As a final general point, due to the multidimensional nature of the action balance equation the computational costs associated with its solution render the use of high fidelity discretisations expensive and inefficient. The use of unstructured adaptive techniques, such as the ones proposed and implemented here, could provide an effective means of increasing the feasible resolutions. This could help bridge the gap between global and coastal scale models and become an efficient framework for the multi-scale nature of spectral wave modelling. This should be further explored by applying the code on more realistic simulations and comparing it in terms of accuracy and computational cost, against other available frameworks.

Bibliography

[1] E. Aboufadel. *Discovering wavelets*. Wiley, New York, 1999.

[2] A. Adam, A. G. Buchan, M. D. Piggott, C. C. Pain, J. Hill, and M. A. Goffin. Adaptive haar wavelets for the angular discretisation of spectral wave models. *Journal of Computational Physics*, 305:521 – 538, 2016.

[3] M. A. Alves, P. Cruz, A. Mendes, F. D. Magalhes, F. T. Pinho, and P. J. Oliveira. Adaptive multiresolution approach for solution of hyperbolic PDEs. *Computer Methods in Applied Mechanics and Engineering*, 191:3909–3928, 2002.

[4] Andorka Gal, J.H. Verification set Haringvliet, October 14, 1982 - October 15, 1982. Report: RIKZ - 95. 112x, Ministry ot Transport, Public Works and Water Management, Netherlands, 1995.

[5] A. Averbuch and V. A. Zheludev. A new family of spline-based biorthogonal wavelet transforms and their application to image compression. *IEEE Transactions on Image Processing*, 13(7):993–1007, 2004.

[6] S. Balay, S. Abhyankar, M. F. Adams, J. Brown, P. Brune, K. Buschelman, L. Dalcin, V. Eijkhout, W. D. Gropp, D. Kaushik, M. G. Knepley, L. C. McInnes, K. Rupp, B. F. Smith, S. Zampini, H. Zhang, and H. Zhang. PETSc Web page. `http://www.mcs.anl.gov/petsc`, 2016.

[7] J. A. Battjes. Shallow Water Wave Modeling. *in: M.Isaacson, M. Quick, (Eds.), Proceeding of International Symposium Waves - Physical and Numerical Modeling, University of British Columbia, Vancouver, ASCE*, pages 1–23, 1994.

[8] J. A. Battjes and J. P. F. M. Janssen. Energy loss and set-up due to breaking of random waves. In *Proceedings of the 16th international conference on coastal engineering*, pages 569–587. ASCE, 1978.

[9] J. A. Battjes and M. J. F. Stive. *Calibration and Verification of a Dissipation Model for Random Breaking Waves*, pages 649–660.

[10] S. Beji and J. A. Battjes. Experimental investigation of wave propagation over a bar. *Coastal Engineering*, 19(1):151 – 162, 1993.

[11] M. Benoit, F. Marcos, and F. Becq. Development of a third generation shallow-water wave model with unstructured spatial meshing. *Coastal Engineering Proceedings*, 1(25), 2001.

[12] N. Booij and L. H. Holthuijsen. Propagation of ocean waves in discrete spectral wave models. *Journal of Computational Physics*, 68(2):307 – 326, 1987.

[13] N. Booij, R. C. Ris, and L. H. Holthuijsen. A third-generation wave model for coastal regions: 1. Model description and validation. *J. Geophys. Res.*, 104(C4):7649–7666, 1999.

[14] F. P. Bretherton and C. J. R. Garrett. Wavetrains in inhomogeneous moving media. *Proceedings of the Royal Society of London A: Mathematical, Physical and Engineering Sciences*, 302(1471):529–554, 1968.

[15] A. G. Buchan, A. S. Candy, S. R. Merton, C. C. Pain, J. I. Hadi, M. D. Eaton, A. J. H. Goddard, R. P. Smedley-Stevenson, and G. J. Pearce. The inner element sub-grid scale finite element method for the Boltzmann transport equation. *Nucl. Sci. Eng.*, 164(2):105–121, 2010.

[16] A. G. Buchan and C. C. Pain. An efficient space-angle subgrid scale discretisation of the neutron transport equation. *Annals of Nuclear Energy*, 94:440 – 450, 2016.

[17] A. G. Buchan, C. C. Pain, M. D. Eaton, R. P. Smedley-Stevenson, and A. J. H. Goddard. Linear and quadratic octahedral wavelets on the sphere for angular discretisations of the Boltzmann transport equation. *Annals of Nuclear Energy*, 32(11):1224–1273, 2005.

[18] A. G. Buchan, C. C. Pain, M. D. Eaton, R. P. Smedley-Stevenson, and A. J. H. Goddard. Self-adaptive spherical wavelets for angular discretisations of the Boltzmann transport equation. *Nucl.Sci.Eng.*, 158:244–263, 2008.

[19] L. Cavaleri, J. Alves, F. Ardhuin, A. Babanin, M. Banner, K. Belibassakis, M. Benoit, M. Donelan, J. Groeneweg, T. Herbers, P. Hwang, P. A. E. M. Janssen, T. Janssen, I. Lavrenov, R. Magne, J. Monbaliu, M. Onorato, V. Polnikov, D. Resio, W. E. Rogers, A. Sheremet, J. McKee Smith, H. L. Tolman, G. van Vledder, J. Wolf, and I. Young. Wave modelling - The state of the art. *Progress in Oceanography*, 75:603–674, 2007.

[20] L. Cavaleri and P. M. Rizzoli. Wind wave prediction in shallow water: Theory and applications. *Journal of Geophysical Research: Oceans*, 86(C11):10961–10973, 1981.

[21] S. G. Chang, B. Yu, and M. Vetterli. Adaptive wavelet thresholding for image denoising and compression. *IEEE Transactions on Image Processing*, 9(9):1532–1546, 2000.

[22] G. Chiavassa, M. Guichaoua, and J. Liandrat. Two adaptive wavelet algorithms for non-linear parabolic partial differential equations. *Computers and Fluids*, 31(47):467 – 480, 2002.

[23] C. K. Chui. *An Introduction to Wavelets*. Wavelet analysis and its applications. Academic Press, 1992.

[24] W. Dahmen. Wavelet methods for PDEs some recent developments. *Journal of Computational and Applied Mathematics*, 128(12):133 – 185, 2001. Numerical Analysis 2000. Vol. VII: Partial Differential Equations.

[25] S. Dargaville, M. A. Goffin, A. G. Buchan, C. C. Pain, R. P. Smedley-Stevenson, P. N. Smith, and G. Gorman. Solving the boltzmann transport equation with multigrid and adaptive space/angle discretisations. *Annals of Nuclear Energy*, 86:99 – 107, 2015. Tribute to a {GIANT}.

[26] I. Daubechies. *Ten Lectures on Wavelets*. Society for Industrial and Applied Mathematics, Philadelphia, PA, USA, 1992.

[27] J. Donea and A. Huerta. *Finite Element Methods for Flow Problems*. John Wiley & Sons, 2003.

[28] Y. Eldeberky. *Nonlinear transformation of wave spectra in the nearshore zone*. PhD thesis, Delft University of Technology, Department of Civil Engineering, The Netherlands, 1996.

[29] Y. Eldeberky and J. A. Battjes. Spectral modeling of wave breaking: Application to Boussinesq equations. *Journal of Geophysical Research: Oceans*, 101(C1):1253–1264, 1996.

[30] H. Elman, D. Silvester, and A. Wathen. *Finite Elements and Fast Iterative Solvers with Applications in Incompressible Fluid Dynamics*. Oxford University Press, first edition, 2005.

[31] K. C. Ewans. Observations of the Directional Spectrum of Fetch-Limited Waves. *J. Phys. Oceanogr.*, 28:495–512, 1998.

[32] M. Farge. Wavelet transforms and their applications to turbulence. *Annual Review of Fluid Mechanics*, 24(1):395–458, 1992.

[33] R. Gelci, H. Cazalé, and J. Vassal. Prévision de la houle. La méthod des densités spectroangulaires. *Bulletin d'information du Comité d'Océanographie et d'Etude des Côtes*, 9:416–435, 1957.

[34] M. A. Goffin, A. G. Buchan, S. Dargaville, C. C. Pain, P. N. Smith, and R. P. Smedley-Stevenson. Goal-based angular adaptivity applied to a wavelet-based discretisation of the neutral particle transport equation. *Journal of Computational Physics*, 281(0):1032 – 1062, 2015.

[35] K. Hasselmann. Weak-interaction theory of ocean waves. In M. HOLT, editor, *Basic Developments in Fluid Dynamics*, pages 117 – 182. Academic Press, 1968.

[36] K. Hasselmann. On the spectral dissipation of ocean waves due to white capping. *Boundary-Layer Meteorology*, 6(1):107–127, 1974.

[37] K. Hasselmann. On the non-linear energy transfer in a gravity-wave spectrum part 1. general theory. 12(4):481–500, 03 2006.

[38] S. Hasselmann, K. Hasselmann, J. H. Allender, and T. P. Barnett. Computations and parameterizations of the nonlinear energy transfer in a gravity-wave specturm. part II: Parameterizations of the nonlinear energy transfer for application in wave models. *Journal of Physical Oceanography*, 15(11):1378–1391, 1985.

[39] H. Hersbach and P. A. E. M. Janssen. Improvement of the short-fetch behavior in the wave ocean model (wam). *Journal of Atmospheric and Oceanic Technology*, 16(7):884–892, 1999.

[40] S. L. Ho and S. Y. Yang. Wavelet-Galerkin method for solving parabolic equations in finite domains. *Finite Elements in Analysis and Design*, 37(12):1023 – 1037, 2001.

[41] L. H. Holthuijsen. *Waves in Oceanic and Coastal Waters*. Cambridge University Press, 2007.

[42] L. H. Holthuijsen, A. Herman, and N. Booij. Phase-decoupled refraction-diffraction for spectral wave models. *Coastal Engineering*, 49(4):291 – 305, 2003.

[43] T. W. Hsu, S. H. Ou, and J. M. Liau. Hindcasting nearshore wind waves using a FEM code for SWAN. *Coastal Engineering*, 52(2):177 – 195, 2005.

[44] Imperial College London AMCG. Fluidity manual v4.1.12. 4 2015.

[45] P. A. E. M. Janssen. Quasi-linear theory of wind-wave generation applied to wave forecasting. *Journal of Physical Oceanography*, 21(11):1631–1642, 1991.

[46] P. A. E. M. Janssen. Progress in ocean wave forecasting. *Journal of Computational Physics*, 227(7):3572 – 3594, 2008. Predicting weather, climate and extreme events.

[47] K. K. Kahma and C. J. Calkoen. Reconciling discrepancies in the observed growth of wind-generated waves. *Journal of Physical Oceanography*, 22(12):1389–1405, 1992.

[48] G. J. Komen, L. Cavaleri, M. Donelan, K. Hasselmann, S. Hasselmann, and P. A. E. M. Janssen. *Dynamics and Modelling of Ocean Waves*. Cambridge University Press, 1994. Cambridge Books Online.

[49] G. J. Komen, K. Hasselmann, and K. Hasselmann. On the existence of a fully developed wind-sea spectrum. *Journal of Physical Oceanography*, 14(8):1271–1285, 1984.

[50] A. J. Kuik, G. P. van Vledder, and L. H. Holthuijsen. A method for the routine analysis of pitch-and-roll buoy wave data. *J. Phys. Oceanogr.*, 18:1020–1034, 1988.

[51] B. P. Leonard. A stable and accurate convective modelling procedure based on quadratic upstream interpolation. *Computer Methods in Applied Mechanics and Engineering*, 19(1):59 – 98, 1979.

[52] E. E. Lewis and W. F. Miller. *Computational methods of neutron transport*. 1984.

[53] M. S. Longuet-Higgins and R. W. Stewart. The changes in amplitude of short gravity waves on steady non-uniform currents. *Journal of Fluid Mechanics*, 10:529–549, 6 1961.

[54] B. J. Lucier, R. A. DeVore, and B. Jawerth. Image Compression Through Wavelet Transform Coding. *IEEE Trans. Inf. The.*, 38:719–746, 1992.

[55] P. A. Madsen and O. R. Sørensen. Bound waves and triad interactions in shallow water. *Ocean Engineering*, 20(4):359 – 388, 1993.

[56] S. G. Mallat. Multiresolution approximations and wavelet orthonormal bases of l2(r). *Transactions of the American Mathematical Society*, 315(1):pp. 69–87, 1989.

[57] C. C. Mei, M. Stiassnie, and D. K. P. Yue. *Theory and Applications of Ocean Surface Waves: Nonlinear aspects*. Advanced series on ocean engineering. World Scientific, 2005.

[58] J. D. Meixner. *Discontinuous Galerkin Methods for Spectral Wave / Circulation Modeling*. PhD thesis, The University of Texas at Austin, August 2013.

[59] J. D. Meixner, J. C. Dietrich, C. Dawson, M. Zijlema, and L. H. Holthuijsen. A discontinuous galerkin coupled wave propagation/circulation model. *Journal of Scientific Computing*, 59(2):334–370, 2014.

[60] J. W. Miles. On the generation of surface waves by shear flows. 3(2):185–204, 03 2006.

[61] C. C. Pain, A. P. Umpleby, C. R. E. de Oliveira, and A. J. H. Goddard. Tetrahedral mesh optimisation and adaptivity for steady-state and transient finite element calculations. *Computer Methods in Applied Mechanics and Engineering*, 190:3771–3796, 2001.

[62] S. Patankar. *Numerical Heat Transfer and Fluid Flow*. Electro Skills Series. Hemisphere Publishing Corporation, 1980.

[63] O. M. Phillips. *The Dynamics of the Upper Ocean*. Cambridge Monographs on Mechanics. Cambridge University Press, 1977.

[64] O. M. Phillips. On the generation of waves by turbulent wind. 2(5):417–445, 03 2006.

[65] W. J. Pierson and L. Moskowitz. A proposed spectral form for fully developed wind seas based on the similarity theory of s. a. kitaigorodskii. *Journal of Geophysical Research*, 69(24):5181–5190, 1964.

[66] W. J. Pierson, G. Neumann, and R. W. James. *Practical methods for observing and forecasting ocean waves by means of wave spectra and statistics*. H.O. Pub 603, US Navy Hydrographic Office, 1955.

[67] M. D. Piggott, G. J. Gorman, C. C. Pain, P. A. Allison, A. S. Candy, B. T. Martin, and M. R. Wells. A new computational framework for multi-scale ocean modelling based on adapting unstructured meshes. *International Journal for Numerical Methods in Fluids*, 56(8):1003–1015, 2008.

[68] S. Popinet. Gerris: a tree-based adaptive solver for the incompressible euler equations in complex geometries. *Journal of Computational Physics*, 190(2):572 – 600, 2003.

[69] S. Popinet, R. M. Gorman, G. J. Rickard, and T. H. L. A quadtree-adaptive spectral wave model. *Ocean Modelling*, 34(12):36 – 49, 2010.

[70] J. Qi, C. Chen, R. C. Beardsley, W. Perrie, G. W. Cowles, and Z. Lai. An unstructured-grid finite-volume surface wave model (fvcom-swave): Implementation, validations and applications. *Ocean Modelling*, 28(13):153 – 166, 2009. The Sixth International Workshop on Unstructured Mesh Numerical Modelling of Coastal, Shelf and Ocean Flows.

[71] S. M. Reckinger, O. V. Vasilyev, and B. Fox-Kemper. Adaptive wavelet collocation method on the shallow water model. *Journal of Computational Physics*, 271(0):342 – 359, 2014. Frontiers in Computational Physics Modeling the Earth System.

[72] R. C. Ris, L. H. Holthuijsen, and N. Booij. A third-generation wave model for coastal regions: 2. verification. *Journal of Geophysical Research: Oceans*, 104(C4):7667–7681, 1999.

[73] R. C. Ris, L. H. Holthuijsen, J. M. Smith, N. Booij, and A. van Dongeren. The ONR test bed for coastal and oceanic wave models. In *Proceedings of*

28th International Conference of Coastal Engineering, pages 380–392. World Scientific Publishing, 2003.

[74] W. E. Rogers, P. A. Hwang, and D. W. Wang. Investigation of wave growth and decay in the swan model: Three regional-scale applications. *Journal of Physical Oceanography*, 33(2):366–389, 2003.

[75] W. E. Rogers, J. M. Kaihatu, H. A. H. Petit, N. Booij, and L. H. Holthuijsen. Diffusion reduction in an arbitrary scale third generation wind wave model. *Ocean Engineering*, 29(11):1357 – 1390, 2002.

[76] A. Roland. *Development of WWM II: spectral wave modelling on unstructured meshes*. PhD thesis, Technische Universit Darmstadt, Institute of Hydraulics and Water Resources Engineering, 2008.

[77] A. Roland, U. Zanke, T.-W. Hsu, S.-H. Ou, J.-M. Liau, and S.-K. Wang. Verification of a 3rd generation FEM spectral wave model for shallow and deep water applications. In *Proceedings of OMAE2006*, pages 487–499. ASME, 2006.

[78] R. L. Snyder, F. W. Dobson, J. A. Elliott, and R. B. Long. Array measurements of atmospheric pressure fluctuations above surface gravity waves. *Journal of Fluid Mechanics*, 102:159, Apr 2006.

[79] O. R. Sørensen, H. Kofoed-Hansen, M. Rugbjerg, and L. S. Sørensen. A third-generation spectral wave model using an unstructured finite volume technique. In *Proceedings of the 29th international conference on coastal engineering*, pages 894–906. ASCE, 2004.

[80] SWAMP Group. *Ocean Wave Modeling*. Plenum Press, 1985.

[81] The SWAN team. *Scientific and Technical Documentation*. Delft University of Technology, SWAN Cycle III version 41.10 2016.

[82] The SWAN team. SWAN Web page. `http://swanmodel.sourceforge.net/`, 2016.

[83] The SWAN team. *User Manual*. Delft University of Technology, SWAN Cycle III version 41.10 2016.

[84] H. L. Tolman. A Third-Generation Model for Wind Waves on Slowly Varying, Unsteady, and Inhomogeneous Depths and Currents. *Journal of Physical Oceanography*, 21(6):782–797, 1991.

[85] H. L. Tolman. Effects of numerics on the physics in a third-generation wind-wave model. *Journal of Physical Oceanography*, 22(10):1095–1111, 1992.

[86] H. L. Tolman. Alleviating the garden sprinkler effect in wind wave models. *Ocean Modelling*, 4(34):269 – 289, 2002.

[87] H. L. Tolman. Limiters in third-generation wind wave models. *Journal of Atmospheric & Ocean Science*, 8(1):67–83, 2002.

[88] H. L. Tolman, M. L. Banner, and J. M. Kaihatu. The NOPP operational wave model improvement project. *Ocean Modelling*, 70:2–10, Oct. 2013.

[89] Z. Ulrich, R. Aron, H. Tai-Wen, O. Shan-Hwei, and L. Jian-Ming. Spectral Wave Modelling on Unstructured Grids with the WWM (Wind Wave Model) II: The Shallow Water Case. In *Third Chinese-German Joint Symposium on Coastal and Ocean Engineering*, Tainan, Taiwan, 2006.

[90] G. P. van Vledder, T. H. C. Herbers, R. J. Jensen, D. T. Resio, and B. Tracy. Modelling of non-linear quadruplet wave-wave interactions in operational wave models. pages 797–811.

[91] WAMDI group. The WAM model - A third generation ocean wave prediction model. *Journal of Physical Oceanography*, 18:1775–1810, 1988.

[92] G. W. Wei, D. S. Zhang, S. C. Althorpe, D. J. Kouri, and D. K. Hoffman. Wavelet-distributed approximating functional method for solving the Navier-Stokes equation. *Computer Physics Communications*, 115(1):18 – 24, 1998.

[93] G. Whitham. *Linear and Nonlinear Waves*. A Wiley-Interscience publication. Wiley, 1974.

[94] B. W. Wilson. Numerical prediction of ocean waves in the North Atlantic for December, 1959. *Deutsche Hydrographische Zeitschrift*, 18:114–130, May 1965.

[95] J. Wu. Wind-stress coefficients over sea surface from breeze to hurricane. *Journal of Geophysical Research: Oceans*, 87(C12):9704–9706, 1982.

[96] B. Yildirim and G. Karniadakis. A hybrid spectral/dg method for solving the phase-averaged ocean wave equation: Algorithm and validation. *Journal of Computational Physics*, 231(14):4921 – 4953, 2012.

[97] I. Young, L. Verhagen, and B. M.L. A note on the bimodal directional spreading of fetch limited wind waves. *Journal of Geophysical Research*, 100:773–778, 1995.

[98] X. Zhou and Y. He. Using divergence free wavelets for the numerical solution of the 2-d stationary NavierStokes equations. *Applied Mathematics and Computation*, 163(2):593 – 607, 2005.

[99] M. Zijlema. Computation of wind-wave spectra in coastal waters with SWAN on unstructured grids. *Coastal Engineering*, 57(3):267 – 277, 2010.

[100] M. Zijlema and A. J. van der Westhuysen. On convergence behaviour and numerical accuracy in stationary SWAN simulations of nearshore wind wave spectra. *Coastal Engineering*, 52(3):237 – 256, 2005.

Appendix

A

Sub-grid scale matrices

The sub-grid scale matrices $\mathbf{A}, \mathbf{B}, \mathbf{C}, \mathbf{D}$, are,

$$\begin{aligned}\mathbf{A}_{i,j} = &\int_V \mathbf{P}_i \frac{1}{\Delta t}\mathbf{M}\mathbf{P}_j dV - \int_V \nabla \mathbf{P}_i \cdot \Big(\mathbf{A}_{\mathrm{s}} c_g(\mathbf{r})^{t,\sigma_q} + \mathbf{M}\mathbf{V}(\mathbf{r})^{t,\sigma_q}\Big)\mathbf{P}_j dV + \\ &\int_\Gamma \mathbf{P}_i \left[\Big(\mathbf{A}_{\mathrm{s}} c_g(\mathbf{r})^{t,\sigma_q} + \mathbf{M}\mathbf{V}(\mathbf{r})^{t}\Big)\cdot \mathbf{n}\right]\mathbf{P}_j d\Gamma + \int_V \mathbf{P}_i \frac{1}{\Delta\sigma}\mathbf{H}_\sigma(\mathbf{r})^{t,\sigma_q}\mathbf{P}_j dV + \\ &\int_V \mathbf{P}_i \mathbf{H}_\theta(\mathbf{r})^{t,\sigma_q}\mathbf{P}_j dV - \int_V \mathbf{P}_i \mathbf{H}_{\mathrm{S}}^{\mathrm{lhs}}(\mathbf{r})^{t,\sigma_q}\mathbf{P}_j dV, \end{aligned} \tag{A.1}$$

$$\begin{aligned}\mathbf{B}_{i,j} = &\int_V \mathbf{P}_i \frac{1}{\Delta t}\mathbf{M}\mathbf{Q}_j dV - \int_V \nabla \mathbf{P}_i \cdot \Big(\mathbf{A}_{\mathrm{s}} c_g(\mathbf{r})^{t,\sigma_q} + \mathbf{M}\mathbf{V}(\mathbf{r})^{t,\sigma_q}\Big)\mathbf{Q}_j dV + \\ &\int_V \mathbf{P}_i \frac{1}{\Delta\sigma}\mathbf{H}_\sigma(\mathbf{r})^{t,\sigma_q}\mathbf{Q}_j dV + \int_V \mathbf{P}_i \mathbf{H}_\theta(\mathbf{r})^{t,\sigma_q}\mathbf{Q}_j dV - \\ &\int_V \mathbf{P}_i \mathbf{H}_{\mathrm{S}}^{\mathrm{lhs}}(\mathbf{r})^{t,\sigma_q}\mathbf{Q}_j dV, \end{aligned} \tag{A.2}$$

$$\mathbf{C}_{i,j} = \int_{V_e} \mathbf{Q}_i \frac{1}{\Delta t}\mathbf{M}\mathbf{P}_j dV + \int_{V_e} \mathbf{Q}_i \nabla \cdot \Big(\mathbf{A}_{\mathrm{s}} c_g(\mathbf{r})^{t,\sigma_q} + \mathbf{M}\mathbf{V}(\mathbf{r})^{t,\sigma_q}\Big)\mathbf{P}_j dV +$$

$$\int_{V_e} \mathbf{Q}_i \Big(\mathbf{A}_{\mathrm{s}} c_g(\mathbf{r})^{t,\sigma_q} + \mathbf{MV}(\mathbf{r})^{t,\sigma_q} \Big) \cdot \nabla \mathbf{P}_j dV + \int_{V_e} \mathbf{Q}_i \frac{1}{\Delta\sigma} \mathbf{H}_\sigma(\mathbf{r})^{t,\sigma_q} \mathbf{P}_j dV + \int_{V_e} \mathbf{Q}_i \mathbf{H}_\theta(\mathbf{r})^{t,\sigma_q} \mathbf{P}_j dV - \int_{V_e} \mathbf{Q}_i \mathbf{H}_{\mathrm{S}}^{\mathrm{lhs}}(\mathbf{r})^{t,\sigma_q} \mathbf{P}_j dV, \tag{A.3}$$

$$\mathbf{D}_{i,j} = \int_{V_e} \mathbf{Q}_i \frac{1}{\Delta t} \mathbf{M} \mathbf{Q}_j dV - \int_{V_e} \nabla \mathbf{Q}_i \cdot \Big(\mathbf{A}_{\mathrm{s}} c_g(\mathbf{r})^{t,\sigma_q} + \mathbf{MV}(\mathbf{r})^{t,\sigma_q} \Big) \mathbf{Q}_j dV + \int_{\Gamma^e_{\mathrm{out}}} \mathbf{Q}_i \left[\Big(\mathbf{A}_{\mathrm{s}} c_g(\mathbf{r})^{t,\sigma_q} + \mathbf{MV}(\mathbf{r})^{t,\sigma_q} \Big) \cdot \mathbf{n} \right] \mathbf{Q}_j d\Gamma + \int_{V_e} \mathbf{Q}_i \frac{1}{\Delta\sigma} \mathbf{H}_\sigma(\mathbf{r})^{t,\sigma_q} \mathbf{Q}_j dV + \int_{V_e} \mathbf{Q}_i \mathbf{H}_\theta(\mathbf{r})^{t,\sigma_q} \mathbf{Q}_j dV - \int_{V_e} \mathbf{Q}_i \mathbf{H}_{\mathrm{S}}^{\mathrm{lhs}}(\mathbf{r})^{t,\sigma_q} \mathbf{Q}_j dV, \tag{A.4}$$

where i, j correspond to sub-matrices of size $K \times K$, with K being the number of angles. Each i, j sub-martix contains the spatial integrals of the angular matrices (presented in section 3.5) for each node combination (i, j) of a spatial element.

The numerical sources, i.e. the right hand side contributions to the system, $\mathbf{S}_\Phi$ and $\mathbf{S}_\Theta$ are

$$\mathbf{S}_{\Phi_i} = \int_{\mathbf{V}} \mathbf{N}_i \mathbf{S}, \tag{A.5}$$

$$\mathbf{S}_{\Theta_i} = \int_{\mathbf{V}} \mathbf{Q}_i \mathbf{S}, \tag{A.6}$$

where $\mathbf{S}_{\Phi_i}$ and $\mathbf{S}_{\Theta_i}$ are vector of size K, containing the spatial integrals of the numerical source $\mathbf{S}$ for each node i of a spatial element.